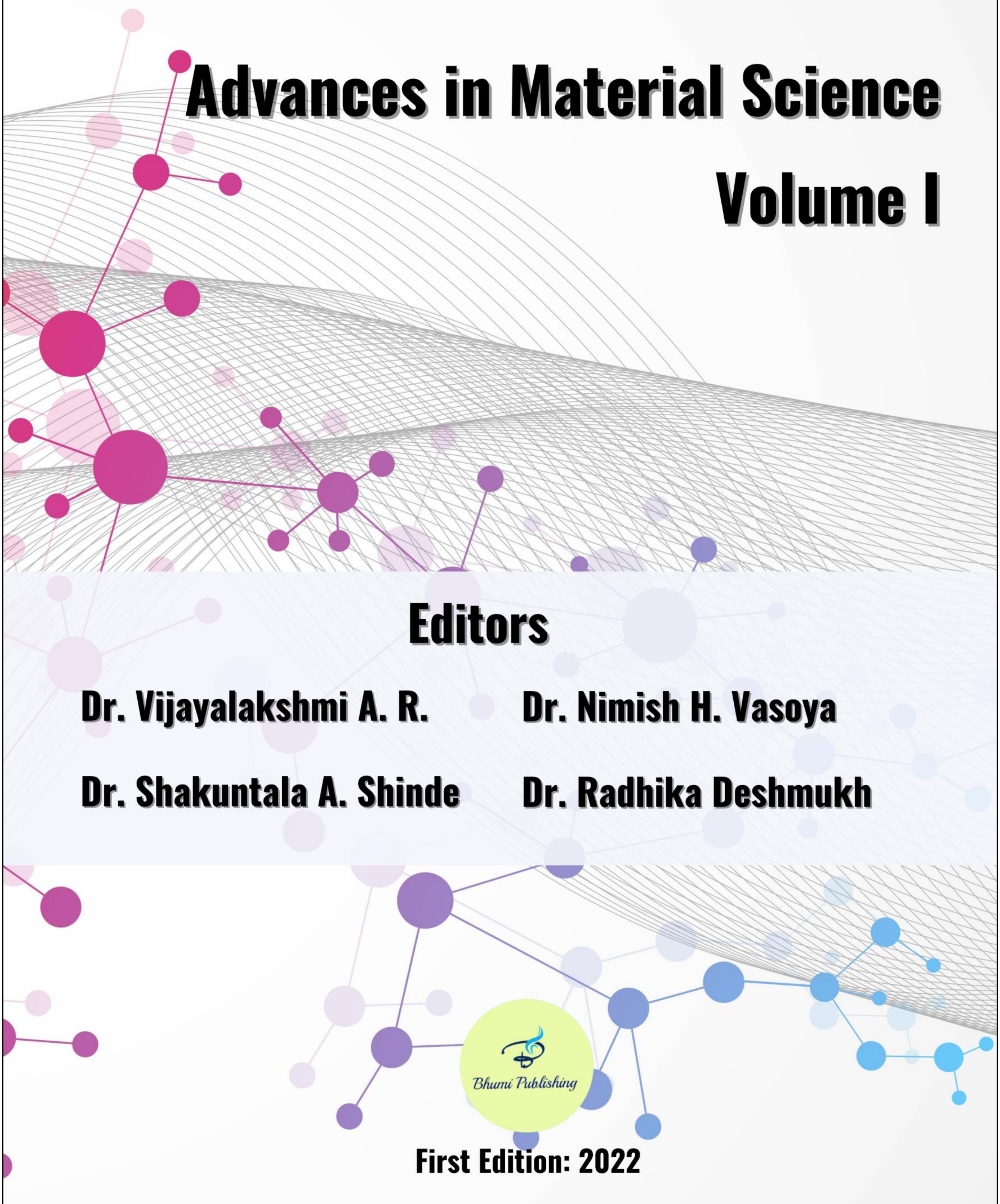

ISBN: 978-93-91768-58-4

Advances in Material Science

Volume I

Editors

Dr. Vijayalakshmi A. R. **Dr. Nimish H. Vasoya**

Dr. Shakuntala A. Shinde **Dr. Radhika Deshmukh**

Bhumi Publishing

First Edition: 2022

Advances in Material Science

Volume I

(ISBN: 978-93-91768-58-4)

Editors

Dr. Vijayalakshmi A. R.
Department of Mathematics,
Maharani's Science College for Women,
Palace Road,
Bangalore

Dr. Nimish Vasoya
Department of Balbhavan and
Toy Innovation,
Children's University,
Gandhinagar, Gujarat

Dr. Shakuntala A. Shinde
Department of Physics,
Sharadchandra Arts, Commerce and
Science College,
Naigaon, Dist- Nanded

Dr. Radhika G. Deshmukh
Department of Physics,
Shri Shivaji Science College,
Amravati,
Maharashtra

Bhumi Publishing

2022

First Edition: 2022

***ISBN:* 978-93-91768-58-4**

Published by:

Bhumi Publishing,
Nigave Khalasa, Kolhapur 416207, Maharashtra, India
Website: www.bhumipublishing.com
E-mail: bhumipublishing@gmail.com

Book Available online at:

https://www.bhumipublishing.com/books/

PREFACE

We are delighted to publish our book entitled ***"Advances in Material Science Volume I".*** *This book is the compilation of esteemed articles of acknowledged experts in the fields of material science providing a sufficient depth of the subject to satisfy the need of a level which will be comprehensive and interesting. It is an assemblage of variety of information about advances and developments in material science. With its application oriented and interdisciplinary approach, we hope that the students, teachers, researchers, scientists and policy makers will find this book much more useful.*

The articles in the book have been contributed by eminent scientists, academicians. Our special thanks and appreciation goes to experts and research workers whose contributions have enriched this book. We thank our publisher Bhumi Publishing, India for compilation of such nice data in the form of this book.

Finally, we will always remain a debtor to all our well-wishers for their blessings, without which this book would not have come into existence.

\- ***Editors***

\- ***Advances in Material Science Volume I***

CONTENTS

SPECTRAL ANALYSIS OF POLY (3-HEXYLTHIOPHENE) AND [6, 6]-PHENYL C_{61}-BUTYRIC ACID METHYL ESTER MATERIALS

Nikhil Rastogi
Department of Physics,
School of Basic Sciences and Technology,
IIMT University, Meerut., U.P., India
Corresponding author E-mail: drnikhilrastogi75@gmail.com

Abstract:

Bulk hetero-junction material is analyzed at various exceptional layer thickness and obvious opening versatility by General Photovoltaic Device Model. GPVDM programming was first made to imitate solar cells and OLEDs, yet later on it has been connected with copy different gadget, including silicon/CIGS-based gadgets. Normal mass hetero-intersection sun organized cell includes mix of P3HT and PCBM as strong material, Indium Tin oxide (ITO) is an unmistakable anode, Poly (3,4-ethylenedioxythiophene) polystyrene sulfonate is an electron stopping layer and Aluminum a cathode. The optical reenactment has performed at different strong layer thicknesses from 100 to 250nm, and electrical entertainment at different openings movability from 1×10^{-4}cm2/Vs to 1×10^{-7}cm2/Vs autonomously. The current-voltage (j-v) attributes are impacted by the underlying flexibility. The best current-voltage (j-v) attributes are found at 1×10^{-6}cm2/Vs adaptability and the best ingestion at 200 nm. It is expected that in the ordinary BHJ sun based cell the ampleness increments, when minimization diminishes, the convenience further rots. Assuming the flexibility is stretched out from 1×10^{-5}cm2/Vs the parcel likelihood is broadened and will be by and large preposterous.

Keywords: P3HT & PCBM Material, Indium Tin oxide, PEDOT: PSS Material

Introduction:

A Solar cell is the device that expected light radiation to work. The plant accomplishes a significant work to change over radiation energy into substance energy. The sun provides us with a nonstop and endless asset of energy and assists us with mitigating emergencies of energy and contamination. Customary sun powered cells dependent upon structure polymers are an extraordinary arrangement promising for an unpretentious and flexible decision instead of inorganic light based cells. Today two or three sun arranged cell headways exist in which standard sun based cells are significant for developments. Natural sun oriented cell s attracts progressively more interest in latest several years. These gives radiations change capability of around 6% to 7% for single convergence cell. It is fundamentally less contrasted and successfully recognized silicon photovoltaic gadget, which has viability above 20%. Regardless, regular photovoltaic (OPV) gadget partake in a couple of advantages like, versatile substrates, the opportunity of insignificant cost creation, room temperature taking care of and thin film structure. Normal sun controlled cells incorporate a blend of polymer advertiser (P3HT) and acceptor (PCBM). In mass hetero-intersection (BHJ) sun powered cells, the photons make emphatically bound electron-openings sets. The openings and electrons are then transported to their different anodes. Investigation attempts to some degree as of late have generally further developed regular sun based cell execution and power change efficiency (PCE) valves better than 10% have actually been achieved. All through the long haul, tremendous investigation tries assessed at developing low band openings polymers to extend maintenance and accumulates more daylight based energy for which the more low current can be conveyed. GPVDM is a free universally useful device for the 1D reenactment. It was created to mimic natural sunlight based cells; it has as of late been stretched out to mimic different gadgets, silicon/CIGS-based gadgets. Both position and energy space inside the gadget are disparaged with between 10-80 autonomous SRH catch/get away from rate conditions being settled at each cross section point.

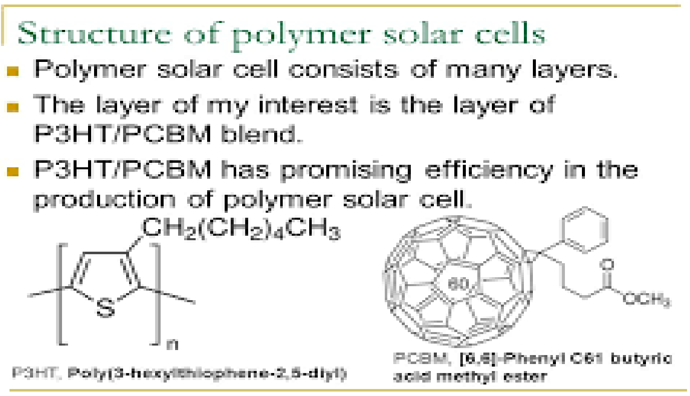

Structure of polymer solar cells

- Polymer solar cell consists of many layers.
- The layer of my interest is the layer of P3HT/PCBM blend.
- P3HT/PCBM has promising efficiency in the production of polymer solar cell.

P3HT, Poly(3-hexylthiophene-2,5-diyl)

PCBM, [6,6]-Phenyl C61 butyric acid methyl ester

Figure 1a: Structure of P3HT: PCBM Material

In ITO/PEDOT: PSS/P3HT: PCBM/Al normal mass hetero-intersection solar cells, P3HT is an electron supporter that effectively transports positive openings, PCBM ([6, 6]-phenyl C61-butyric destructive methyl ester) is an electron acceptor materials. It effectively moves electrons starting with one iota then onto the next. The film of ITO (Indium Tin Oxide) is used as a straight forward terminal. Since, it has high transport around there and cutoff of conduction. Poly (3, 4-ethylenedioxythiophene) poly (styrene-sulfonate) is an initial transportation layer. PEDOT: PSS may be used as layers between the straight forward cathodes and dynamic layer of materials to deter the electron and opening trade off base. In this examination we present ghostly induction of mass hetero-intersection (BHJ) sun fueled cell using GPVDM programming at different unique layer thicknesses. The essential advantage of the mass heterojunction sun arranged cell is that an enormous piece of made excitons show up at a nearby supporter acceptor interface, where they related into free charge carriers.

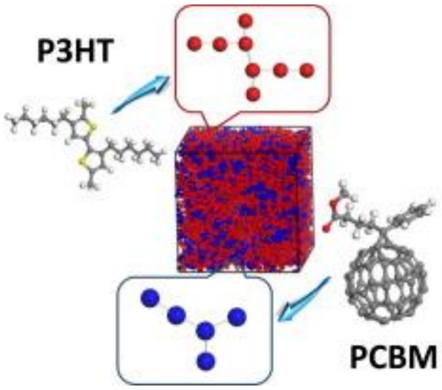

Figure 1b: Atomic Structure of P3HT: PCBM Material

Design and charge carriers:

Bulk hetero-junction, a mix of interpenetrating mix of electron patron and electron acceptor shaped normal materials, which grant maintenance of radiation, the time of charge carriers, splitting of excitons at sponsor acceptor association point, and transport of positive and negative charges to reverse terminals. (BHJ) are generally delivered by molding the two structure polymers, anticipating and a while later allowing secluding the two phases, when in doubt, with the help of hardening process. The two structure polymers will self gathered into an interpenetrating network communicating the two anodes. The construction is displayed in figure 2.

Later the catch of a photon, electron move to the acceptor spaces, then, are brought through the device and accumulated by the one cathode and openings moves reverse way and assembled at inverse side. Expecting the dissipating of the two materials is especially greater, it will achieve defenseless charge travel through the unique layer. In control move, the two providers and acceptor add to the time of charge carriers.

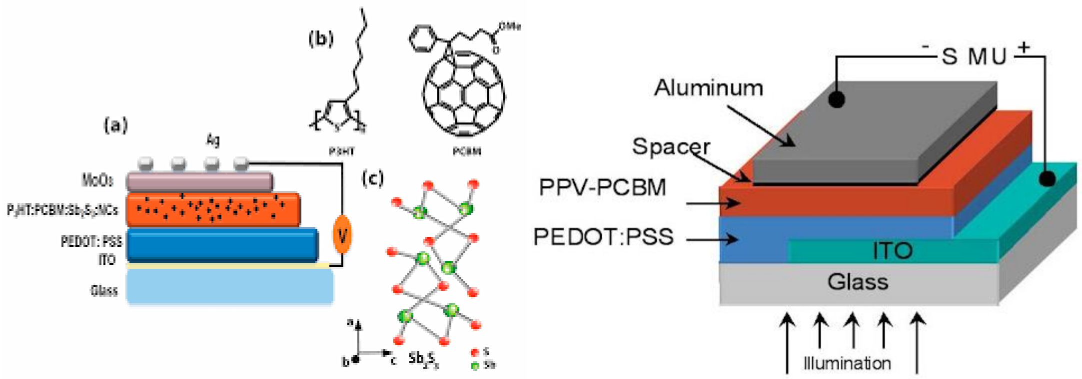

Figure 2: Bulk hetero-junction solar cell materials

The Solar cells produce normal adaptable excitons later osmosis of light. To disconnect the excitons into free charge carriers a supporter acceptor system ought to be used. On account of the lower excitons spread lengths to 1-10 nm in polymeric materials a direct bilayer configuration will achieve low efficiencies, since just photons ingested inside this detachment from D/A mark of communication will add to the device current. A development in the delivered photo current can be achieved by using an interpenetrating association of provider and acceptor materials. Ideally in mass hetero-intersection (BHJ), all consumed photons will be close by patron acceptor interface and these can be adding to the made photocurrent.

Analysis of the material:

Bulk hetero-junction solar cell reproduced by the product on different systems square. The product creating PC programs is unequivocally expected to imitate mass hetero-intersection standard sun based cells. The model contains ghastly properties, drawing in both stream voltages credit to be imitated in much the same way as optical properties. The electrical model basically covers the strong layer of the gadget. In this model, there are two sorts of charge transporter electrons, free electrons and got electrons. Free electrons have a restricted transportability of μ_{oe} (μ_{oh}) and got electrons can't move using any and all means and have an adaptability of nothing. To survey the typical conveniences we take the extent of free to got carriers and copy it by the free carrier flexibility.

$$\mu_e(n) = \frac{\mu_e^{\circ} n_{free}}{n_{free} + n_{trap}}$$

Thus if all carriers were free the average mobility would be $\boldsymbol{\mu^o_e}$ and if all carriers were trapped the average mobility would be zero. The Material simulation is shown in figure 3.

Spectral based analysis:

Bulk hetero-junction solar cell is simulated by the apparatus at different outstanding layer thicknesses. GPVDM making PC programs is unequivocally planned to copy mass hetero-intersection conventional sun coordinated cells, for instance, those wards on the P3HT: PCBM material. The model contains otherworldly person of the sun controlled cell; support both stream voltage ascribes to be reenacted similarly as optical properties. GPVDM contains both an electrical and optical model. The optical model expansion if all else fails wires the glass substrate, the contacts and layers like PEDOT: PSS. The electrical engendering normally cover, the interesting layer of the contraption, subsequently a regularly optical entertainment is fundamentally more conspicuous than electrical reenactment window. Subsequently, it depicted the phantom model which can deal with the optical reenactment and it moreover addresses the strong layer. This is conceivable by putting a 'yes in segment (dynamic layer) in the figure 4.

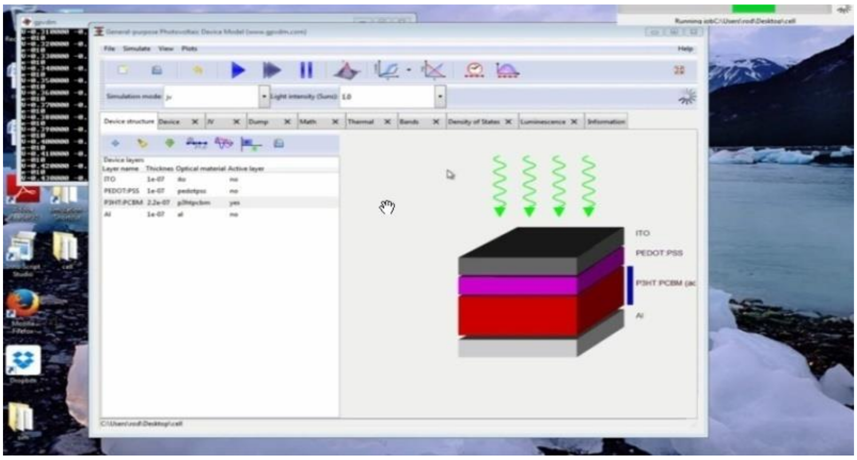

Simulation mode: jv
Light intensity (Suns): 1.0

Device layers

Layer name	Thicknes	Optical material	Active layer
ITO	1e-07	ito	no
PEDOT:PSS	1e-07	pedotpss	no
P3HT:PCBM	2.2e-07	p3htpcbm	yes
Al	1e-07	al	no

Figure 3: Material simulation

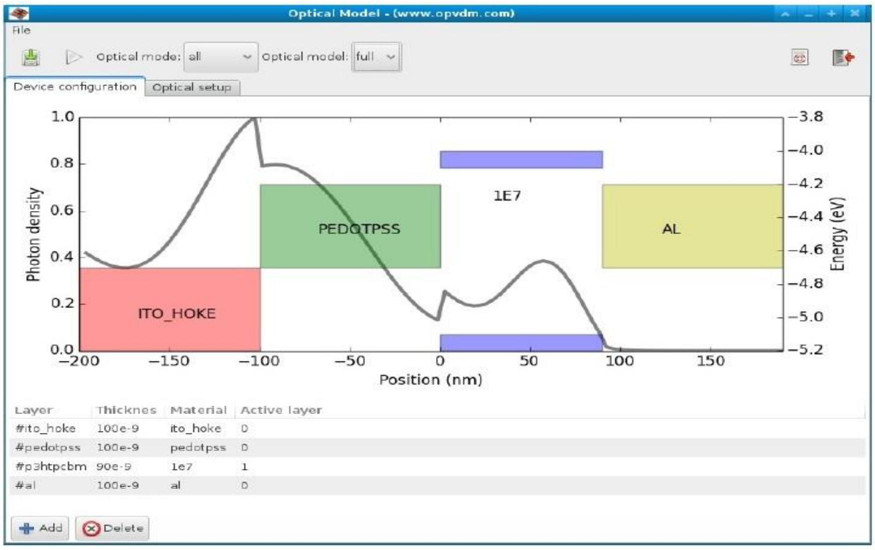

Optical mode: all
Optical model: full

Layer	Thicknes	Material	Active layer
#ito_hoke	100e-9	ito_hoke	0
#pedotpss	100e-9	pedotpss	0
#p3htpcbm	90e-9	1e7	1
#al	100e-9	al	0

Figure- 4: Spectral based analysis

Result and Discussion:

In the present work bulk hetero-junction sunlight based cells are simulated by the tool to analyse the spectral characteristics. The retention of P3HT: PCBM dynamic layer are extra feasible for the rehash from 350-750nm. The optical reenactment (repeat 150-750 nm) is made at various interesting layer thickness, PEDOT: PSS thickness 20 nm, the thickness of ITO 20nm, Al thickness 20nm and the layer thickness are 180nm, 200nm, 220nm, and the systems of support at different strong layer thicknesses are displayed in the figure 5a, 5b and 5c. The j-v qualities are reproduced at different openings adaptability, 1×10^{-4}cm2/Vs to 1×10^{-7}cm2/Vs, which is showed up in figure 6. It is clear from the I-v twists that the short current thickness is high at 1×10^{-6}cm2/Vs and least at 1×10^{-4}cm2/Vs.

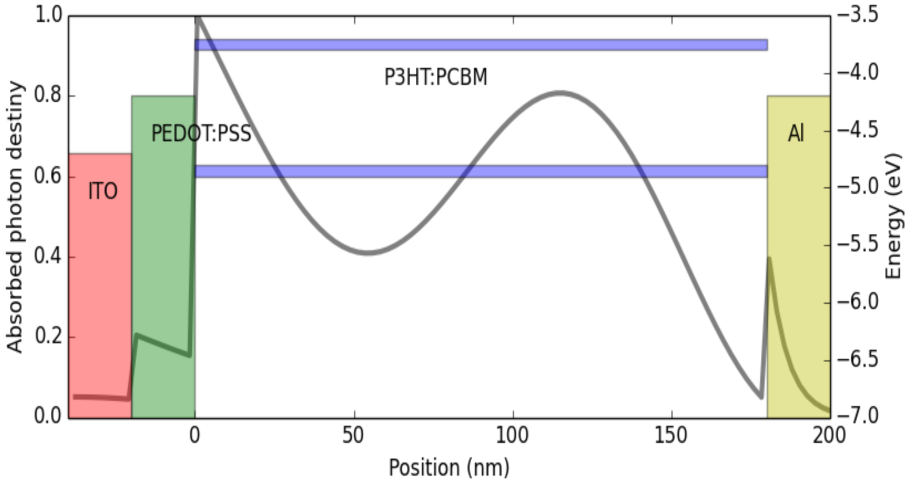

Figure 5a: Analysis on 180 NM

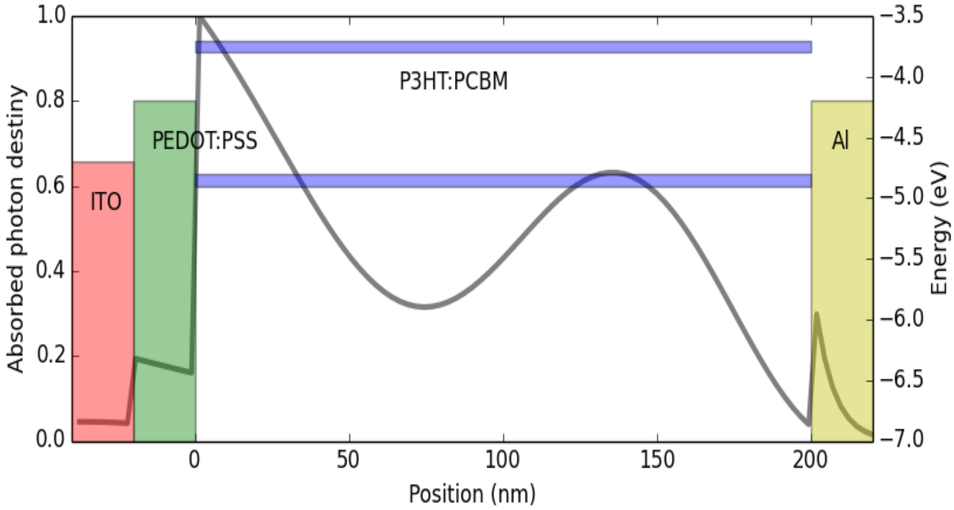

Figure 5b: Analysis on 200 NM

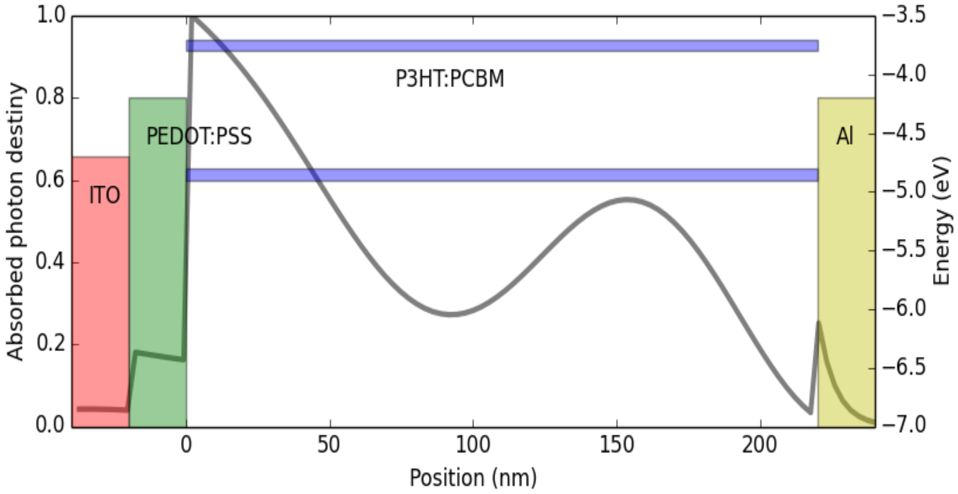

Figure 5c: Analysis on greater than 200 NM

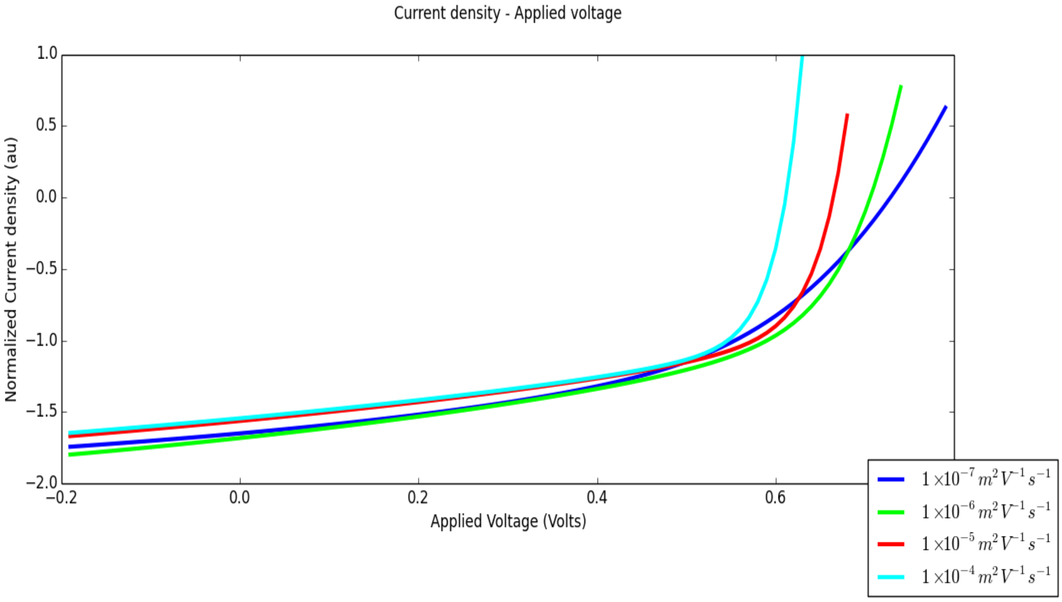

Figure 6: Analysis of j-v characteristics of the material

The twists in regular BHJ solar cell material, the efficiency increases when versatility lessens. The extended recombination of electron-opening consolidate and reduce detachment capability, decrease viability however the hardship in open circuit voltage at higher carrier compactness is at risk for the reduction of usefulness. If the transportability is extended from 1×10^{-5}cm2/Vs the division probability is extended and will be most prominent at 1×10^{-6}cm2/Vs, and again increase the flexibility the partition won't further addition and viability is decay. Obviously the sun situated cell is capable at unmistakable adaptability range.

Conclusion:

The presentation of otherworldly properties of P3HT: PCBM based mass hetero-intersection solar cell materials for different astounding layer thickness. The upkeep layout of the intriguing layer of standard sun organized cell changes with thickness. At 200 nm thickness, we get ingestion beat close to the terminals at which the best support occur. The short out current is impacted by the electron and opening movability and generally incredible short out current acquired at 1×10^{-6}cm2/Vs. Along these lines by changing the exceptional layer thickness and adaptability the productive upkeep and effectiveness of P3HT: PCBM based sunlight based cells can be updated.

It is in like manner construed that in the customary BHJ sun organized cell the limit increases, when flexibility lessens (from 10^{-4} to 10^{-6}) while more than 10^{-7} convey capacity, the efficiency further decreases. If the versatility is connected from 1×10-5cm^2/Vs the section probability is extended and will be all around incredible at 1×10^{-6}cm^2/Vs, and again increase the accommodation the division won't further development and capacity is rot.

References:

1. Alan Heeger J. "2^{5th} Anniversary Article. Bulk Heterojunction Solar Cells: understanding the Mechanism of Operation". Advanced Materials; 2014.
2. Arumugam, Sasikumar Li, arasu Yi, Senthil, Torah Russel, Kanibolotsky Alexander, Inigo Anto, Skabara, Peter, Beeby, Stephen. Fully spray-coated organic solar cells on woven polyester cotton fabric for wearable energy harvesting applications. J. Mater. Chem. A. 2016;4. DOI: 10.1039/C5TA03389F
3. Chen Hsiang-Yu, Hou Jianhui, Zhang Shaoqing, Liang, Yongye., Yang, Guanwen .,Yang Yang, Yu,Luping Wu, Yue Gang, Li. Polymer solar cells with enhanced open-circuit voltage and efficiency. Nature Photon. 2009;3:649–653.
4. Clarke TM, Durrant JR. Chargephotogeneration in organic solar cells Chem. Rev. 2010;110:6736–6767.
5. Dou Jingb, Yang Jun, ChenChun-Chao He, Youjun Murase, Seiichiro Moriarty, Tom, Emery, Keith , GangLi, Yang Yang. Tandem polymer solar cells featuring a spectrally matched lowbandgap polymer. Nature Photon. 2012;6:180–185.
6. He Z, Zhong C, Su S, Xu M, Wu H, Yong Cao Y. Enhanced power-conversion efficiency in polymer solar cells using an inverted device structure. Nature Photon. 2012;6:593–597. DOI: 10.1038/nphoton.2012.190

7. Jingbi Dou, Letian Ken, Yoshimura Takehito Kato, Ohya Kenichiro, Moriarty Tom, Chun-Chao Chen, Emery, Gao Jing, Gang Li, Yang Yang. A polymer tandem solar cell with 10.6% power conversion efficiency. Nature Commun. 2013;4:1446 .
8. Kroon R, Halls JJM, Walsh CA, Greenham NC, Marseglia EA, Friend RH, Moratti SC, Holmes AB. Efficient photodiodes from interpenetrating polymer networks, Nature. 1995;376:498–500.
9. Lone Mohammad, Jilte Ravindra. A review on phase change materials for different applications. Materials Today: Proceedings. 2021;46:10980-10986. DOI: 10.1016/j.matpr.2021.02.050
10. Majdi HS, Latipov ZA, Borisov V, *et al.* Nano and Battery Anode: A Review. Nanoscale Res Lett. 2021;16:177.doi.org/10.1186/s11671-021-03631-x
11. Markov DE, Amsterdam E, Blom PWM, Sieval AB, Hummelen JC. Accurate measurement of the exciton diffusion length in a conjugated polymer using a heterostructure with a side-chain cross-linked fullerene layer", J. Phys. Chem. A. 2005;109:5266–5274.
12. Michael M Lee, JoëlTeuscher, Tsutomu Miyasaka, Takurou N Murakami, Henry J Snaith. Efficient Hybrid Solar Cells Based on Meso-SuperstructuredOrganometal Halide Perovskites Science. 2012;02(338,6107):643-647. DOI: 10.1126/science.1228604
13. Peumans Peter, Uchida Soichi, Forrest Stephen. Efficient bulk heterojunction photovoltaic cells using small-molecular-weight organic thin films; 2010. DOI: 10.1142/9789814317665_0015.
14. Rait S, Kashyap S, Bhatnagar PK, Mathur PC, Sengupta SK, Kumar J. Improving power conversion efficiency in polythiophene/fullerene-based bulk heterojunction solar cells, Sol. Energy Mater. Sol. Cells. 2007;91:757–763.
15. Rastogi N, Singh N, Saxena N. Analysis of organic photovoltaic device at different series resistances. Universal Journal of Materials Science. 2017;5(4):83-87.
16. Rastogi N, Singh N. Electrical simulation of organic solar cell at different series resistances and different temperatures. IOSR Journal of Applied Physics (IOSR-JAP). 2016;8(3):54-57.
17. Singh N, Chaudhary A, Rastogi N. International Journal of Material Science. 2015;5:2226-4523/15/01 022-5.
18. Tang CW. 2-layer organic photovoltaic cell, Appl. Phys. Lett. 1986;48:183–185.

MATERIAL Bu-PPQ SHOWING CHARACTERISTIC PROPERTIES

Pratima V. Damre

Department of Applied Science,

GCOEAR, Awsari (Khurd), Pune

Corresponding author E-mail: pvdamre@gmail.com

Abstract:

All the PQ derivative materials formed were investigated though FTIR, NMR spectroscopic and Mass spectrometric analysis. The thermal properties of the materials were studied by TG and DT analysis. Morphological studies of the materials were carried out through XRD, AFM and SEM studies and material is further subjected to electrical characterization by DC-conductivity measurement using four probe conductivity instruments. The optical investigations, providing the temperature-dependent conductive defects formation in the obtained structures.

Keywords: Bu-PPQ, Conductive defects, CeCl3

Introduction:

Typically, poly(quinoline)s have high thermal stability with glass-transition temperatures (Tg) above 200◦C and onset thermal decomposition temperatures (Tdec) above 400◦C, high oxidative stability, high electrical conductivity, and outstanding mechanical and optically clear film forming properties [8 –10]. These characteristics make poly(quinoline)s interesting materials for electronic and/or electro-optical devices. Over the last decade, Jenekhe, Jen, and others have investigated extensively the optical and electronic properties of poly(-quinoline)s including photo-conductivity,[10] optical nonlinearity [2, 3], photoluminescence [1–8], electroluminescence [2–7], charge-transfer [3 - 8], and electron transporting properties [7–4] for their potential applications in OLEDs [2–3] organic photovoltaic devices [1] and selective chemosensors (proton and metal ions) [4 –5].

Experimental Section:

Material and Method:

1 equiv of the diacetyl monomer, 1 equiv of 3,3-dinonanoylbenzidine, 6.0 g of diphenyl phosphate, and 3 g of *m*-cresol were added to a cylindrical reaction ves-sel. The reactor was

purged with argon for 20 min. The mixture was mechanically stirred under static argon as the temperature was gradually raised to 140°C over a pe-riod of 12 h. The polymerization mixture was stirred at this temperature for 72 h and then precipitated into 10% triethylamine/ethanol. The precipitate was collected by vacuum filtration and extracted on a Soxhlet apparatus for 72 h with 20% triethy-mine/ethanol. The polymer was dissolved in CHCl3 and precipitated into ethanol, collected by vacuum filtration, and dried at 60 °C in a vacuum for24 h.

Results and Discussion:

Conjugated rigid-rod polyquinolines have excellent thermal stability and high mechanical strength [1,2]. These *n*-type semiconducting polymers [3] have interesting electronic [2 b], photoconductive [4], and nonlinear optical [5] properties. Recently, some polyquinolines were used as both the electron-transport layer and an emission layer in polyquinoline/poly(*p*-phenylenevinylene) heterojunction light-emitting diodes (LEDs) [6]. The attractive combination of excellent thermal, mechanical, and optoelectronic properties of the conjugated polyquinolines has motivated our synthe-sis of new derivatives for electroluminescent device applications.

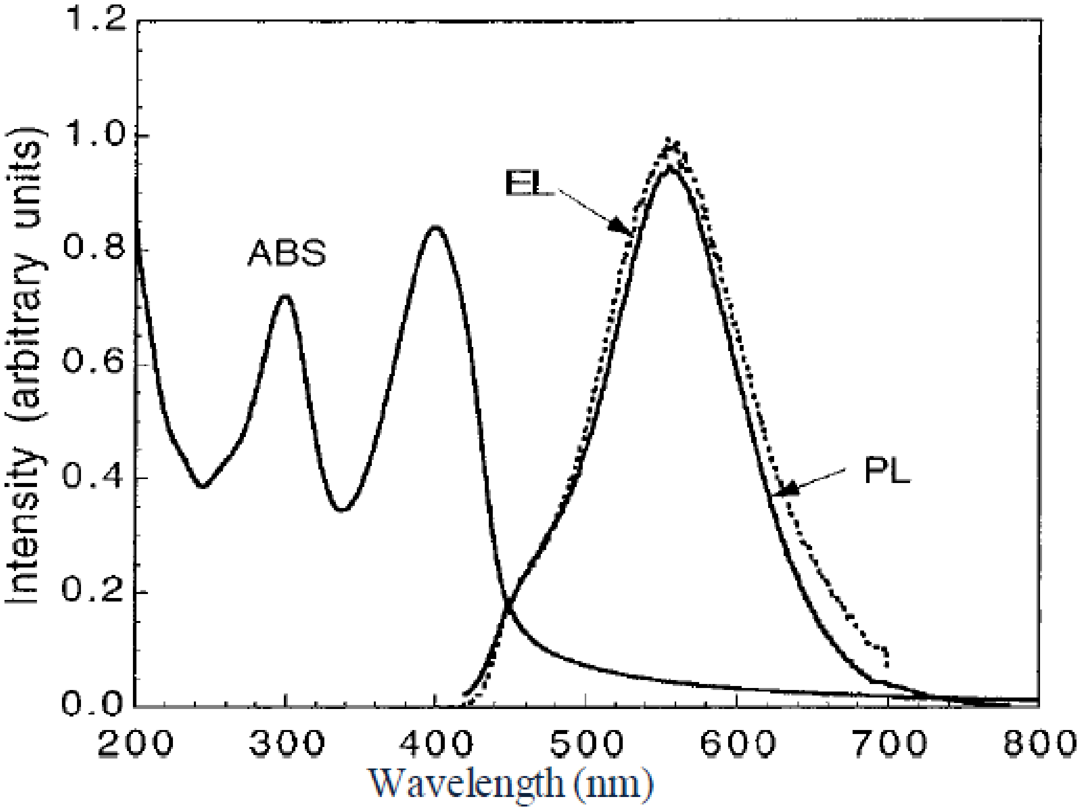

Figure 1: Optical absorption, photoluminescence (excited at 399 nm) and electroluminescence (8 V) spectra of Bu-PPQ thin films

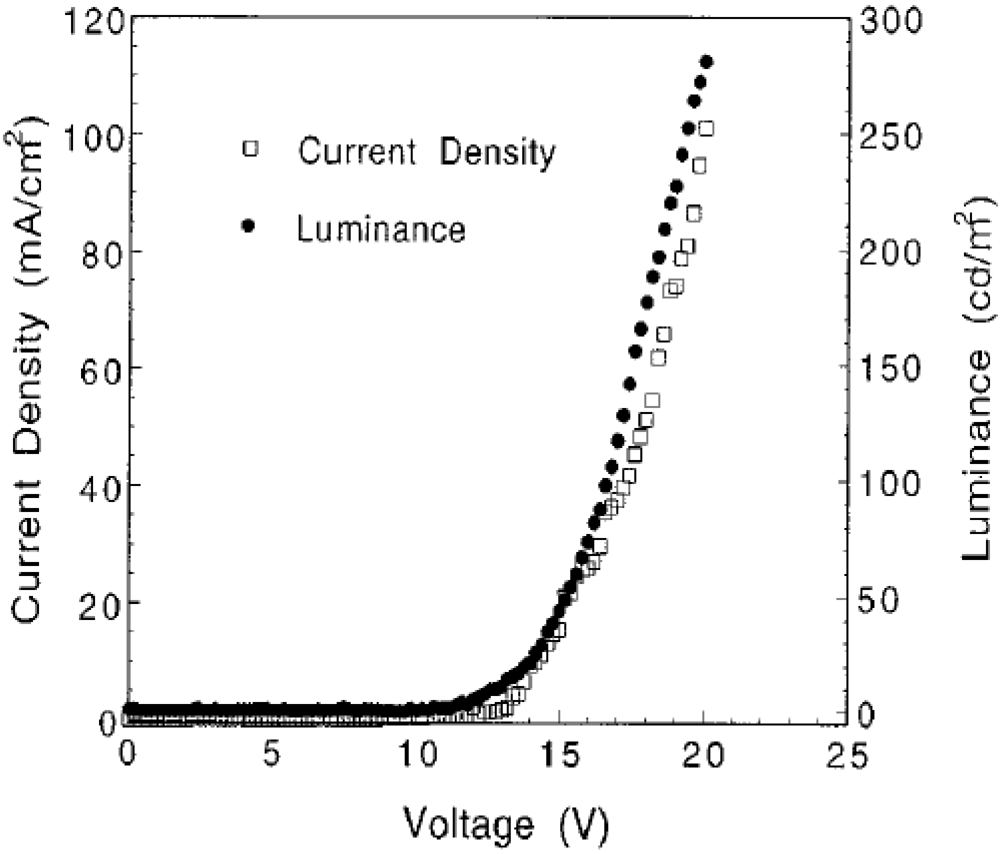

Figure 2: Current –voltage and voltage –luminance characteristics of the electroluminescent device ITO/TAPC: PS/Bu-PPQ/Al

Figure 1 shows the optical absorption, steady-state photoluminescence (PL), and electroluminescence (EL) spectra of Bu-PPQ. This polymer shows a strong ab-sorption with a p-p* transition at 399 nm. The optical absorption edge bandgap is 2.78 eV (446 nm). Bu-PPQ thus has absorption peak and bandgap identical to those of PPPQ, which were previously reported [2 b]. This suggests that the ground state electronic structure of PPPQ does not change with the introduction of the *tert*-butyl groups inBu-PPQ. Also shown in Fig. 1 is the steady-state PL spectrum of Bu-PPQ thin film excited at 399 nm. The PL spectrum shows an emission peak at 554 nm. The yellow emission corresponds to a large Stokes shift of 155 nm (0.87 eV), which is characteristic of excimer emission of the solid film of many conjugated polymers [10]. The PL emission of Bu-PPQ showed a 20 nm blue shift compared to PPPQ(**1**), which has a PL emission peak at 574 nm. This indicates that the introduction of the *tert*-butyl groups in Bu-PPQ modifies the excited state electronic structure of the par-ent polymer PPPQ. That chain packing of conjugated polymers should significantly influence their excited state properties more than their ground state electronic proper-ties has been predicted [10].

The EL spectrum of the device ITO/TAPC:PS/Bu-PPQ/Al at a bias voltage of 8 V is shown in Fig. 1. The EL emission peak is at 554 nm. It can be seen that the EL spectrum is identical to the PL spectrum, indicating that the EL emission is from the Bu-PPQ layer only and that the electroluminescence and photoluminescence of Bu-PPQ originate from the same excited states. Figure 2 shows the current–voltage and luminance voltage characteristics of the EL device. The turn-on voltage of the ITO/TAPC:PS(50 nm)/Bu-PPQ(50 nm)/Al device was 8 V. It showed bright yellow color emission, which can be clearly seen under room light. The luminance of the device was 280 cd/m2 at a current density of 100 mA/cm2. The EL efficiency of the device was estimated to be 0.26% photons/electron. These values were about six times higher than those of PPPQ (**1**) under the same conditions. For example, the de-vice ITO/TAPC:PS(50 nm)/PPPQ(50 nm)/Al had a luminance of 45 cd/m2 at the same current density of 100 mA/cm2. The large enhancement of electroluminescence in the *tert*butyl- substituted Bu-PPQ (**2**) compared to the parent polyquinoline **1** can be understood in terms of reduced concentration quenching of luminescence facilitat-ed by increased inter chain packing distances [10]. Observation of efficient electro-luminescence in the ITO/TAPC:PS/Bu-PPQ/Al devices implies that the emissive Bu-PPQ layer also exhibits good electron transport (*n*-type) characteristics, in accord with prior findings for other polyquinolines [3, 6].

In summary, a new electroluminescent, yellow lightemitting *n*-type conju-gated polymer, Bu-PPQ (**2**), has been synthesized and characterized. Although the substitution of *tert*-butyl groups in Bu-PPQ did not change the optical absorption properties of the parent PPPQ, a more efficient electroluminescence with an EL quantum efficiency of 0.26% photons/electron and a luminance of 280 cd/m2 was observed. The brightness and efficiency of light-emitting diodes from Bu-PPQ (**2**) were six times higher that those of PPPQ (**1**) with no *tert*-butyl substitution. These results also demonstrate that thin films of the new polyquinoline exhibit good elec-tron transport (*n*-type) characteristics in EL devices.

Acknowledgement:

This research was supported by the Department of Chemistry, Government Vidarbh Institute of Science and Humanities, Amravati.

References:

1. P.D. Sybert, W.H. Beever, J.K. Stille, Macromolecules 1981, 14, 493. [b] E.K. Zimmerman, J.K. Stille, Macromolecules 1985, 18, 321. [c] M.W. Pelter, J.K. Stille, Macromolecules 1990, 23, 2418.
2. A.K. Agrawal, S.A. Jenekhe, Chem. Mater. 1992, 4, 95. [b] A.K. Agrawal, S.A. Jenekhe, Macromolecules 1993, 26, 895.
3. A.K. Agrawal, S.A. Jenekhe, Chem. Mater. 1996, 8, 579.
4. M.A. Abkowitz, M. Stolka, H. Antoniadis, A.K. Agrawal, S.A. Jenekhe, Solid State Commun. 1992, 83, 937.
5. A.K. Agrawal, S.A. Jenekhe, H. Vanherzeele, J.S. Meth, J. Phys.Chem. 1992, 96, 2837.
6. S.A. Jenekhe, X. Zhang, X.L. Chen, V.-E. Choong, Y. Gao, B.R. Hsieh, Chem. Mater. 1997, 9,409.
7. D.M. Sutherlin, J.K. Stille, Macromolecules 1985, 18, 2669.
8. G.S. Skinner, J.A. Gladner, R.F. Heitmiller, J. Am. Chem. Soc.1951, 73, 2230.
9. R.B. Davis, L.C. Pizzini, J. Org. Chem. 1960, 25, 1884.
10. S.A. Jenekhe, J.A. Osaheni, Science 1994, 265, 765.
11. J.A. Osaheni, S.A. Jenekhe, J. Am. Chem. Soc. 1995, 117, 7389.

NUMERICAL ANALYSIS OF STRESS CONCENTRATION FACTOR IN RECTANGULAR PLATE WITH CIRCULAR HOLE USING ANSYS

Sivapriya. S, Manisha. C, Elavarasi. M
Department of Aerospace Engineering,
Periyar Maniammai Institute of Science and Technology,
Thanjavur, 613403, India

Abstract:

The elements, which are used for machining having geometrical irregularities. These in discretions divert the stress distribution. The stress distribution of rectangular plate having a circular hole is examined. The structural steel materials are used for analysis. The results are about stress distribution and deformation for the designing of the machine. Likewise, it is experimental that, as Thickness/Diameter ratio increases, stress concentration factor also increases. Therefore from the current study, it can be said that finite element analysis is a very active tool to calculate stresses in various materials.

Introduction:

Ansys develops and markets multi-physics engineering simulation software for product design, testing and operation and offers its products and services to customers worldwide. In the twenties, the company acquired numerous other engineering design companies, obtaining additional technology for fluid dynamics, electronics design, and physics analysis. Ansys Workbench is a convenient way of managing your simulation projects.

Ansys Mechanical proposals a lively environment with a comprehensive range of analysis tools, from making geometry for analysis to connecting added physics for even greater dependability. Ansys is one of the tools which are presently used with a lot of applications which have significant effects on our daily life. The elements with geometrical irregularities are used for machining, which disturb the stress distribution. Finite element analysis is a powerful technique used for solving engineering problems having designs that are subjected to boundary conditions. In the earlier period, some of the researchers have been deal with exact solutions of plate deflections with different boundary condition. Finite element analysis is used in new product design. Structural steel is a category of steel used for making construction materials in a variety of shapes. Many structural steel shapes take the form of an stretched out beam having a profile of a detailed cross section. Structural steel shapes, sizes, chemical composition, mechanical properties such as strengths, storage practices, are regulated by standards in most industrialized countries.

The accuracy of simulations depends on the quality of the material property information. Thus, there is a state of information about the stress concentration in the structural component. While, the majorities of service crashes occurred in the area of stress concentration at the edge of a hole. In this study, the stress distribution of rectangular plate with structural steel materials having circular hole is carried out and results is about the stress distribution and deformation for the design. The present work deals with the analysis of a rectangular plate with the hole being considered as a stress distribution.

Literature survey:

Dhanjal *et al.* (1) suggested that the elements, which are used for machining purposes offered with geometrical irregularities, which disturb the stress distribution and therefore, the state of stress in stress concentrated regions cannot be described in machine elements. Mekalke *et al.* (2) explained that the finite element method (FEM) is a numerical method of analysis for stresses and deformations in structures of any given geometry. There are many solutions to reduce the stress concentration includes providing relief notches, holes etc. and investigated a plate with a circular hole applied to a uniform stress and examined the deviation in the results obtained through different meshes. Shivlingesh *et al.* (3) studied SCF's depend on the dimension ratio defined as the hole diameter of the beam to the width of the beam. The maximum stress occurs at corners of holes in both materials. Brahmbhatt *et al.* (4) analysed that the rectangular plate with a central elliptical hole using ANSYS and having lower values of aspect ratio, stress intensity factor gives less error. Shaik *et al.* (5) have found that stress concentration is always taking place on cut-out boundary in a finite width plate with a central hole under in static loading. The rectangular plate having a central hole is a common structure, but stress concentration around the hole makes the material liable to failure across the cut-out region.

Material and Modelling:

In this study, a rectangular plate of structural steel material with hole has to be occupied for calculating stresses and deformations produced due to the applied force and fixed support. Likewise, the effect of Thickness/Diameter ratio has been analyzed by using various Thickness/Diameter (T/D) ratios which are 0.2, 0.4, 0.6, 0.8, and 1.0. The analytical method and finite element method were used to calculate the stress concentration factor using ANSYS.

Material properties of structural steel:

Property	Value
Tensile ultimate strength	460 MPa
Tensile yield strength	250 MPa
Young's modulus	2×10^{11} Pa
Poisson's ratio	0.3
Bulk modulus	1.6667×10^{11} Pa
Shear modulus	7.6923×10^{10} Pa

Source. Ansys database.

The rectangular plate with a circular hole has taken for calculating maximum stress and deformation due to applied force.

Length of the plate = 150 mm,

Width of the plate = 50 mm,

Diameter of the hole = 10 mm

The present investigation is the study of the rectangular plate having a circular hole exposed to a uniform stress. The length of the rectangular plate is 150 mm, thickness is varied from 2, 4, 6, 8, 10 mm & width is 50 mm, with a hole of diameter d is10 mm. The applied uniform stress is σ = 1000 N to the both sides.

The stress concentration factor is calculated below:

Stress concentration factor (K_t) = $3.0 - 3.13(d/W) + 3.66(d/W)^2 - 1.53(d/W)^3$

$K_t = 3.0 - 3.13(10/50) + 3.66(10/50)^2 - 1.53(10/50)^3$

$K_t = 2.50816$

Finite element method

The geometry is formed and calculated in ANSYS. The force is applied on both sides of the plate. The fixed support is applied in centre. The meshed body of rectangular plate with hole is shown below,

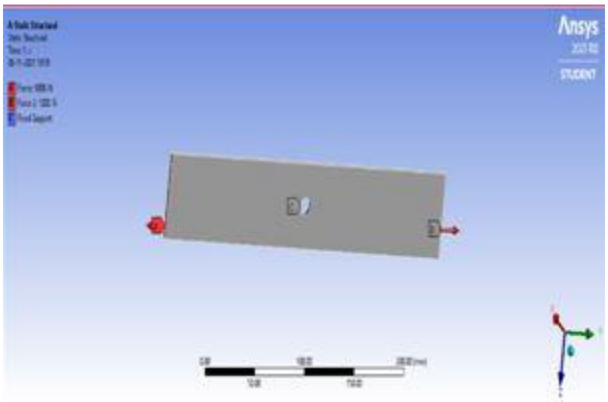

Figure 1: 3D Geometry with load applied on both sides

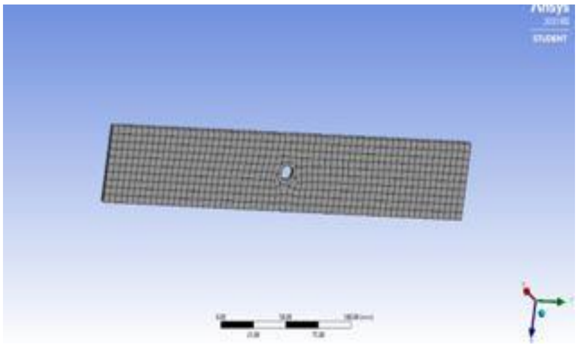

Figure 2: Meshed model of rectangular plate with hole

The stress concentration factor for a rectangular plate having a circular hole can be calculated by using the following equation,

Stress concentration factor (K_t) = $\sigma_{\text{Maximum stress}} / \sigma_{\text{Normal stress}}$ -----------------> (1)

Where,

σ_{max} - Maximum stress

σ_{nom} - Nominal stress.

σ_{nominal} = applied force / area = F/A ------------------> (2)

$\text{Area} = (W \times T) - (\pi/4 \times d^2)$

$= (50 \times 2) - (\pi/4 \times 10^2)$

$= 21.47 \text{ mm}^2$

$\sigma_{\text{Nominal}} = 1000 \text{ N} / 21.47 \text{ mm}^2$

$= 46.57$ Mpa

The values of nominal stress and K_t are shown in the following table:

Table 1: Values of nominal stress and K_t

Thickness	σ_{nominal}	K_t
2mm	46.57 MPa	1.042
4mm	8.232 MPa	2.625
6mm	4.515MPa	3.184
8mm	3.110 MPa	3.819
10mm	2.372MPa	4.523

Results:

The equivalent Von-Mises stress and deformations of structural steel for various thicknesses were shown below.

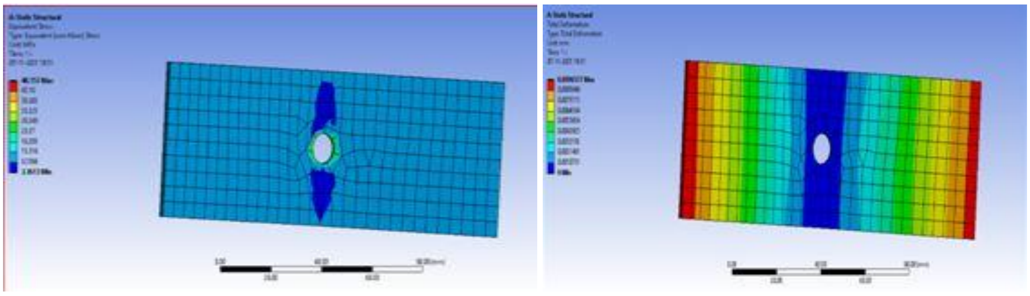

(a) Von-Mises for 2mm **(b) Deformations for 2mm**

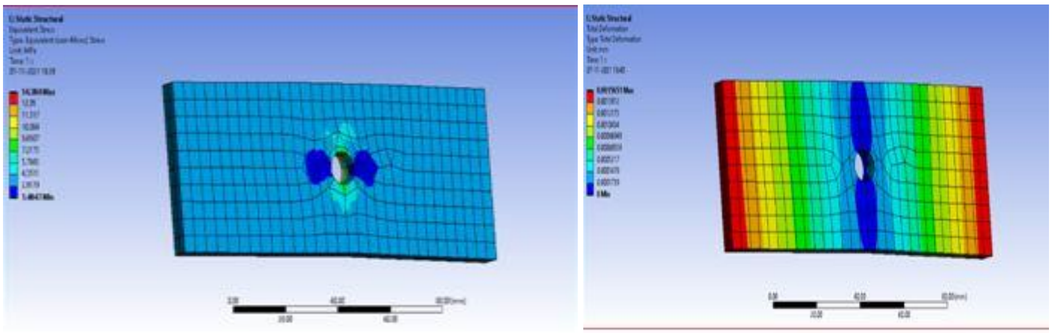

(a) Von-Mises for 4mm **(b) Deformations for 4mm**

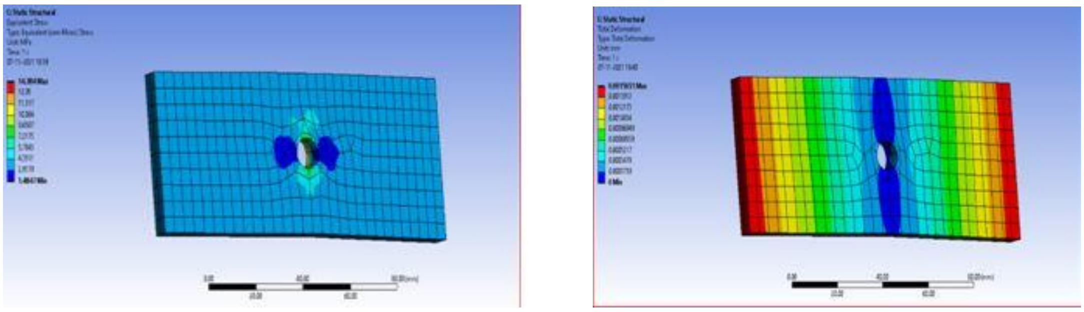

(a) Von-Mises for 6mm **(b) Deformations for 6mm**

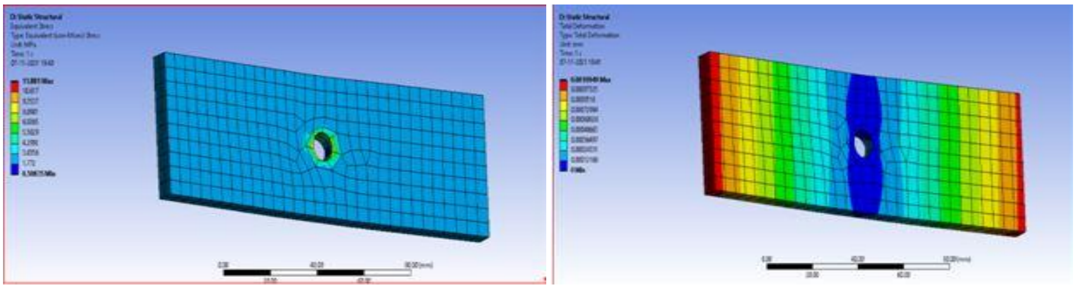

(a) Von-Mises for 8mm **(b) Deformations for 8mm**

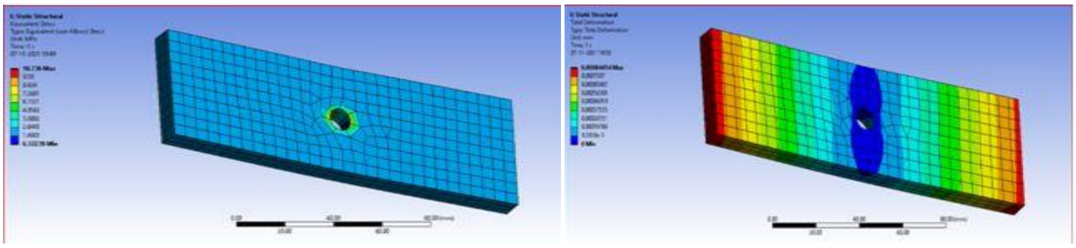

(a) Von-Mises for 10mm **(b) Deformations for 10mm**

Figure 3: Equivalent Von-Mises stress and deformations of structural steel for 2 mm thickness

Calculation of Percentage error

Percentage error in theoretical and practical values = Theoretical value – (FEM values/ Theoretical values)

Percentage Error for 2 mm = 2.5081-1.042 / 2.5081

= 2.092

= 0.31%

Error for 2mm = 0.31%

Error for 4mm = 0.25%

Error for 6mm = 0.18%

Error for 8mm = 0.14%

Error for 10mm = 0.10%

The values of Thickness/Diameter ratio, maximum Von-Mises stress, maximum deformation and stress concentration factor are represented in Table 2. The stress concentration factor is based on FEM values and theoretical values.

Table 2: Stress concentration factor is based on FEM values and theoretical values

T/D Ratio	Material	Maximum (Von-mises Stress) (MPa)	Max. Deformation (mm)	FEM values	Theoretical values	Error %
0.2	Structural steel	48.15	0.0096	1.042	2.5081	0.31
0.4		21.61	0.0028	2.625	2.5081	0.25
0.6		14.38	0.0015	3.184	2.5081	0.18
0.8		11.88	0.0010	3.819	2.5081	0.14
1.0		10.73	0.0008	4.523	2.5081	0.10

The graphical representations of various Thickness/Diameter (T/D) ratios were shown below, Equivalent Von-Mises stress and stress concentration factor of materials is represented in below figure.

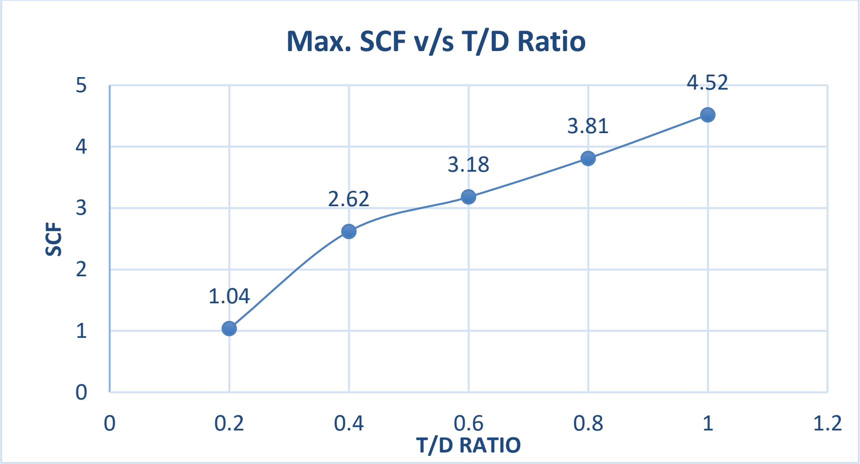

Figure 4: T/D ratio Vs SCF

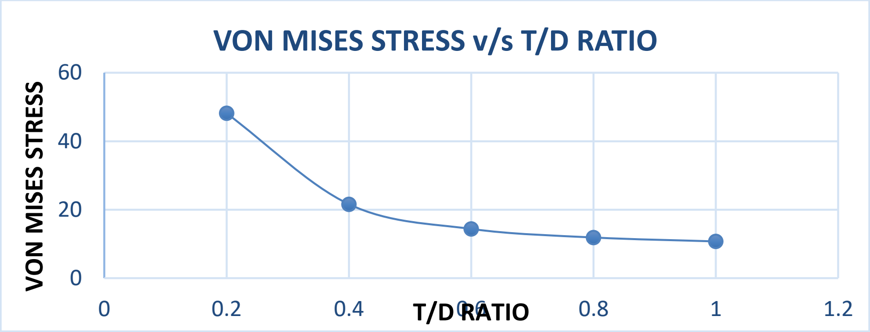

Figure 5: T/D ratio Vs Von-Mises Stress

Conclusion:

From the present study, it is observed that the deformation decreases with increase in Thickness/Diameter ratio, though an increase in Thickness/Diameter (T/D) ratio resulted as, decrease in von Mises stress and as Thickness/Diameter (T/D) ratio increases with increase in stress concentration factor. The stress concentration factor values obtained from finite element analysis shows error of 0.31% for structural steel. Therefore, from the present study, it can be said that finite element analysis is a very active tool to determine stresses in various materials.

References:

1. S. Dhanjal and R. Arora, Stress Analysis of a Rectangular Plate with Circular Hole Using Three Dimensional Finite Element Model, Int. J. Engg., Business and Enterprise Applications (IJEBEA), 1(12), 77-80 (2015).

2. G. C. Mekalke, M. V. Kavade and S. S. Deshpande, Analysis of a Plate with a Circular Hole by FEM, IOSR J. Mech. Civil Engg. (IOSR-JMCE), 1(5), 25-30 (2012).
3. Shivlingesh, S. B. Kivade, B. Mallikarjun. FEA Analysis of Stresses for Cantilever Beam with Hole Subjected to Different Mode of Loading Systems, Int. J. Adv. Engg. Technol., Manage. Appl. Sci., 3(1), 116-126 (2016).
4. D. Brahmbhatt, K. Brahmbhatt and D. Patel, Stress Concentration Factor Converts Into Stress Intensity Factor using ANSYS, European J. Adv. Engg. Technol., 2(1), 4649 (2015).
5. A. S. Shaik and I. M. Mirzana, Stress Concentration of Rectangular Plate with a Hole Made With Composite Material Using Finite Element Analysis, IOSR J. Mech. Civil Engg. (IOSR-JMCE), 13(4), 01-05 (2016).

ELASTICITY OF MATERIALS

D. B. Zade
Department of Physics,
Shri JSPM College, Dhanora, District - Gadchiroli MH 442 606
Corresponding author E-mail: dbzade04@gmail.com

Introduction:

In material science, elasticity is the ability of a body to resist a distorting influence and to return to its original shape and size when the force is removed.When an external unbalanced force is applied to a body; it gets deformed due to relative displacement of molecules. Due to this relative displacement of molecules, forces are developed inside the body which tends to oppose the deforming forces. If the deforming forces acting on the body are removed then the body is acted upon by internal elastic forces developed within the body which try to restore to its original dimensions. Solid objects will deform when adequate load are applied to them, if material elastic, the objects will return to its initial shape and size. Some bodies which return exactly to its original dimensions after removal of deforming forces are called perfectly elastic bodies. The reasons for elastic behavior are different for different materials.

Hooke's Law of Elasticity:

In 1676 Robert Hooke Physicist from U.K. discovered a relationship between stress and strain and has given fundamental law of elasticity. This relation is known as Hook's Law of elasticity.

It states that within the elastic limit, the force required to deform elastic body is directly proportional to the distance of deformation, regardless of how large that distance becomes.

Elastic moduli:

In engineering the elasticity of material is quantified by the elastic modulus. Such as the Young's modulus, (Y) Bulk modulus, (K) and Modulus of rigidity (ŋ) which measure the amount of stress required to achieve a unit of strain. Higher modulus shows that the material is harder to deform.

Young's modulus (Y):

The modulus of elasticity which is related to change in length of a body is called Young's modulus of elasticity.

It is defined as the ratio of longitudinal stress to longitudinal strain, within elastic limits.When there is change in length takes place then the strain is known as longitudinal strain.

Consider a metal wire of length L and radius r suspended from a rigid support. When a deforming force is applied to metal wire in one direction, change in length takes place. Let l be the increase in length which caused by the application of force, then

Longitudinal strain = $\frac{\text{change in length}}{\text{original length}}$

Longitudinal strain=$\frac{l}{L}$

Since force F is applied along the length and is perpendicular to its area of cross section,

∴Longitudinal stress = $\frac{\text{applied force}}{\text{area}}$

$= \frac{F}{\pi r^2}$

Hence, Young's modulus of elasticity =$\frac{\text{Longitudinal stress}}{\text{Longitudinal strain}}$

$$Y = \frac{\frac{F}{\pi r^2}}{\frac{l}{L}}$$

$$Y = \frac{FL}{\pi r^2 l}$$

The S.I. unit of Young's modulus is N/m^2 and its dimensions are [$L^{-1} M^1 T^{-2}$].

Bulk modulus:

The modulus of elasticity which is related to change in volume of body is called bulk modulus of elasticity.

It is defined as the ratio of volume stress to volume strain. When there is change in volume takes place due to application of force then the strain is known as volumetric strain.

Consider a rubber cube having volume 'V'. When a uniform pressure or force F applied perpendicular to its surface, it undergoes a change in volume. Let 'v'be the change in volume of cube then,

Volume strain = $\frac{\text{Change in volume}}{\text{Original volume}}$

$= \frac{v}{V}$

Volume stress = $\frac{\text{Applied force}}{\text{area}}$

$= \frac{F}{a}$

Hence, Bulk modulus of elasticity = $\frac{\text{Volume stress}}{\text{Volume strain}}$

$K = \frac{\frac{F}{a}}{\frac{v}{V}}$

But $\frac{F}{a}$ = P = applied pressure

$\therefore K = P.\frac{v}{V}$

When a very small pressure 'dP'is applied, the change in volume being very small i.e. dV, then

Bulk modulus, $K = -V\frac{dP}{dV}$

The negative sign indicates that an increase in applied pressure causes a decrease in volume.

Bulk modulus of elasticity is the property of solids, liquids, and gases. The S.I. unit of Bulk modulus is N/m^2 and its dimensions are $[L^{-1} M^1 T^{-2}]$.

Modulus of rigidity:

The modulus of elasticity which related with changes in shape of a body is called modulus of rigidity.

It is defined as within elastic limit, the ratio of tangential stress to shearing strain is called modulus of rigidity.

To find the value of shearing strain, consider a solid cube ABCDEFGH. The lower face DCGH is fixed and a tangential force F is applied at the upper face ABEF so that the upper face is displaced to a new position A'B'E'F' as shown in figure.

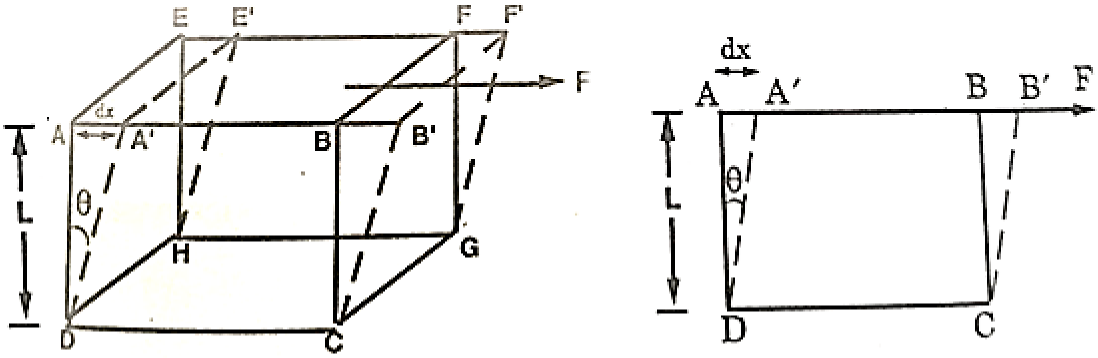

Shearing strain = $\frac{\text{Displacement of a upper plane}}{\text{Distance from the fixed plane}}$

$= \frac{AA'}{AD}$

$= \frac{dx}{L}$

$\therefore$ Shearing strain = tan θ

When θ is small, then tanθ = θ

∴Shearing strain = θ and

Now, Tangential stress = $\frac{\text{applied force}}{\text{area}}$

$= \frac{F}{a}$

Thus, modulus of rigidity = $\frac{\text{Tangential stress}}{\text{Shearing strain}}$

$= \frac{\frac{F}{a}}{\theta}$

∴Modulus of rigidity = $\frac{F}{a\,\theta}$

Poisson's ratio:

When a force is applied to a body along any direction, then, there is change in size along the direction of force and also change in size in perpendicular direction occurs.

When a force is applied to the free end of a metal wire, it gets elongated, its length increases but its diameter decreases. Consider a wire of length 'L' and diameter 'D' is stretched longitudinally by a force, then its length increases by 'l' and diameter decreases by 'd'

∴Longitudinal strain, α = $\frac{\text{Change in length}}{\text{Original length}}$

$\alpha = \frac{l}{L}$ and

Lateral strain, β = $\frac{\text{Change in diameter}}{\text{Original diameter}}$

$\beta = \frac{d}{D}$

Poisson discovered that within elastic limit, lateral strain is proportional to longitudinal strain

The ratio of lateral strain to longitudinal strain is called Poisson's ratio and it is denoted by 'σ'

Thus, Poisson's ratio = $\frac{\text{Lateral strain}}{\text{Longitudinal strain}}$

$\sigma = \frac{\beta}{\alpha}$

$\sigma = \frac{\frac{d}{D}}{\frac{l}{L}}$

$\sigma = \frac{dL}{Dl}$

Poisson's ratio is a unit less and dimensionless quantity.

Torsional Pendulum:

A solid heavy body like a disc fastened at its mid-point by long and thin elastic wire and suspended from a rigid support, constitute a **Torsional Pendulum.**

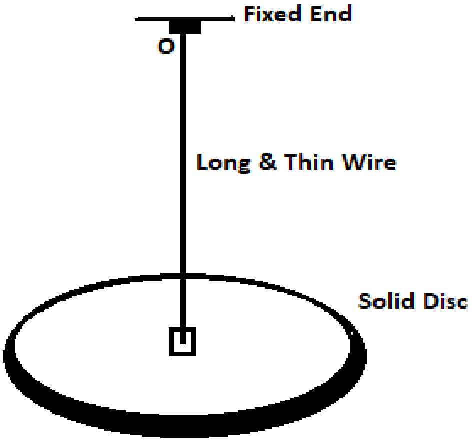

Torsion oscillations:

If the suspended body is slightly rotated through a small angle from its equilibrium position about the axis of suspension by applying a torque, then lower end of the wire will get twist and due to this twist restoring torque is produced in the wire.

Now if external torque is removed, then angular acceleration produced in the body in opposite direction to that of the twist. But due to inertia, body does not come to rest and it rotated in opposite direction. Now the wire is twisted in the opposite direction and again restoring torque is produced in the body. Thus the body oscillates about the wire as an axis and such oscillations are called **Torsion oscillations.**

Periodic time of Torsion Pendulum:

Let the disc is rotated through a small angle θ. Due to this restoring torque is produced in the wire which tends to bring it back into its original position.

Restoring torque, $\tau \propto \theta$

$\therefore$Restoring torque, $\tau = - C\theta$

Where C is restoring torque per unit angular twist of the wire and - ve sign indicates that the restoring torque is oppositely directed to the angular displacement.

If I is the M.I. of the disc about the wire as axis passing through its center and $\frac{d^2\theta}{dt^2}$ is its angular acceleration then twisting torque acting on it is given by

Twisting torque $= \frac{I\, d^2\theta}{dt^2}$

Now Twisting torque = Restoring torque

$\therefore \frac{I\, d^2\theta}{dt^2} = - C\theta$

$\frac{d^2\theta}{dt^2} = - (\frac{C}{I})\theta$

$\therefore \frac{d^2\theta}{dt^2} \propto -\theta$

T hus, the angular acceleration is directly proportional to its angular displacement and both are oppositely directed to each other. Hence the torsion pendulum performs an angular S.H.M. andits periodic time will be

$$T = \frac{2\pi}{\sqrt{\frac{C}{I}}}$$

$$T = 2\pi \sqrt{\frac{I}{C}}$$

Relation between elastic constants:

1) **Relation between Y, K, and σ**

   Consider a unit cube which is of homogeneous isotropic material and let the forces F_x, $F_y$and F_z act parallel to X, Y and Z direction respectively on the faces of cube as shown in fig.

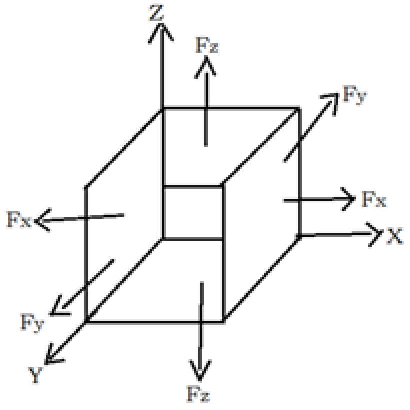

   If we assume pair of force F_x-F_x is acting on the cube then they produce elongation along x-axis and lateral contraction along y-axis and z-axis.

   Let α = Increase in length per unit length along the direction of force i.e. longitudinal strain per unit stress and

   β = Contraction produced per unit length per unit tension in a direction perpendicular to the force i.e. lateral strain per unit stress.

∴Increase in length along x-axis = αF_x

Contraction strain along y- axis = βF_y

Contraction strain along z- axis = βF_z

∴Net increase in length l_x produced in the side of a unit cube along x-direction is

$l_x = \alpha F_x - \beta F_y - \beta F_z$

$l_x = \alpha F_x - \beta (F_y + F_z)$---------------(1)

Similarly net increase in length along y-direction and z-direction are

$l_y = \alpha F_y - \beta (F_x + F_z)$-----------------(2)

$l_z = \alpha F_z - \beta (F_x + F_y)$-----------------(3)

If the forces acting on the three faces are equal, then

$F_x = F_y = F_z$

Therefore equation (1) becomes

$l_x = \alpha F_x - 2\beta F_x$

$l_x = (\alpha - 2\beta) F_x$

$\therefore\ l_x = l_y = l_z = (\alpha - 2\beta) F_x$

Therefore new length of each side of a unit cube = $[1 + (\alpha - 2\beta)F_x]$

Hence the new volume of the cube = $[1 + (\alpha - 2\beta)F_x]^3$

Since α and β are very small quantities, terms containing their square and higher power can be neglected. Therefore expanding and neglecting higher powers,

New volume of the cube = $1 + (\alpha - 2\beta)\, 3F_x$

∴ Increase in volume of the cube = $[1 + (\alpha - 2\beta)\, 3F_x] - 1$

$= (\alpha - 2\beta)\, 3F_x$

∴ Volume strain = $\frac{\text{Increase in volume}}{\text{Original volume}}$

$= \frac{(\alpha - 2\beta)\, 3Fx}{1}$

$= (\alpha - 2\beta)\, 3F_x$

Hence Bulk modulus, K = $\frac{\text{Volume stress}}{\text{Volume strain}}$

$K = \frac{F_x}{(\alpha - 2\beta)\, 3F_x}$

$K = \frac{1}{3(\alpha - 2\beta)}$

Divide the numerator and the denominator by α, then

$$K = \frac{\frac{1}{\alpha}}{\frac{3(\alpha - 2\beta)}{\alpha}}$$

$$K = \frac{\frac{1}{\alpha}}{3(1-2\frac{\beta}{\alpha})}$$

But $\frac{1}{\alpha} = Y$ and $\frac{\beta}{\alpha} = \sigma$

$$\therefore K = \frac{Y}{3(1 - 2\sigma)}$$

Or $Y= 3K (1 - 2\sigma)$

This equation gives the relation between Y, K and σ.

Relation between Y, η and σ:-

When a tangential force F is applied to the upper face of a cube ABCD then the upper face ABCD is displaced to the new position A'B'CD. The diagonal DB increases in the length to DB' and diagonal CA decreases to CA'

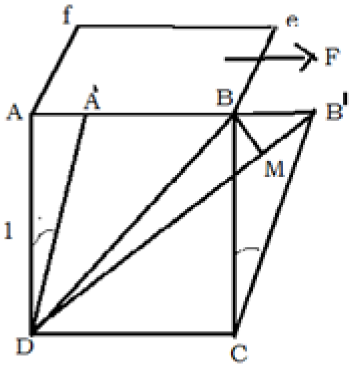

It means that, the unit cube is subjected to only two forces i.e. extensional force along x-axis and equal compressional force along z-axis

Therefore in this case $F_y= 0$ and $F_z = -F_x$

Thus equation (1), (2) and (3) becomes

$l_x = \alpha F_x - \beta (F_y+F_z)$

$l_x= \alpha F_x - \beta F_y- \beta F_z$

$l_x = \alpha F_x - 0 - \beta(-F_x)$ --------------By putting $F_y= 0$ and $F_z = -F_x$ $\therefore l_x= \alpha F_x+ \beta F_x$

$\therefore l_x= (\alpha + \beta) F_x$-----------------(4)

l_y=α F_y – β (F_x+F_z)

l_y= 0 –β (F_x–F_x)----------------By putting F_y= 0 and F_z = -F_x ∴ l_y= 0---------------------------(5) and

l_z= α F_z – β (F_x+F_y)

l_z= -α F_x - β (F_x+ 0) --------------By putting F_y= 0 and F_z = -F_x

∴ l_z= - (α + β) F_x ----------------(6)

From equation (4) and (6)

l_x = - l_zThus there will be equal extensional and contractional strains along x-axis and z-axis

Now modulus of rigidity, $\eta = \frac{\text{Shearing stress}}{\text{Shearing strain}}$

$= \frac{F_x}{\Phi}$

In this case, shearing strain = 2(α + β) F_x

$$\therefore \eta = \frac{F_x}{2(\alpha + \beta)\, F_x}$$

$$\eta = \frac{1}{2(\alpha + \beta)}$$

2η (α + β) = 1

Dividing both sides by α, we get

$$\therefore \frac{2\eta(\alpha + \beta)}{\alpha} = \frac{1}{\alpha}$$

$$2\eta\left(1+\frac{\beta}{\alpha}\right) = \frac{1}{\alpha}$$

But $\frac{1}{\alpha}$ =Y and $\frac{\beta}{\alpha}$ = σ

∴2η (1+σ) = Yor

$$\eta = \frac{Y}{2\,(1+\sigma)}$$

This equation gives the relation between **Y, η and σ.**

Relation between Y, K and η:-

We have the relation between Y, η and σ.

$$\eta = \frac{Y}{2\,(1+\sigma)}$$

or Y = 2η (1+σ)

$\therefore \frac{Y}{\eta} = 2\,(1+\sigma)$

$\frac{Y}{\eta} = 2 + 2\sigma$ --------------------(1)

The relation between Y, K and σ.

$K = \frac{Y}{3(1-2\sigma)}$

Or $Y = 3K\,(1-2\sigma)$

$\therefore \frac{Y}{3K} = (1-2\sigma)$ -----------------(2)

Adding equation (1) and (2) we get

$\frac{Y}{\eta} + \frac{Y}{3K} = 2 + 2\sigma + 1 - 2\sigma$

$\frac{Y}{\eta} + \frac{Y}{3K} = 3$

Multiplying above equation by $\frac{3}{Y}$

$\therefore \frac{Y}{\eta}\frac{3}{Y} + \frac{Y}{3K}\frac{3}{Y} = 3\,\frac{3}{Y}$

$\frac{3}{\eta} + \frac{1}{K} = \frac{9}{Y}$ or

$\frac{9}{Y} = \frac{1}{K} + \frac{3}{\eta}$

This equation gives the relation between **Y, K and η**

Relation between K, η and σ:-

The relation between Y, K and σ.

$K = \frac{Y}{3(1-2\sigma)}$

$\therefore Y = 3K\,(1-2\sigma)$ -------------(1)

The relation between Y, η and σ.

$\eta = \frac{Y}{2\,(1+\sigma)}$

Or $Y = 2\eta\,(1+\sigma)$ -------------------(2)

Equating equation (1) and (2) we get

$3K\,(1-2\sigma) = 2\eta\,(1+\sigma)$

$3K - 6K\sigma = 2\eta + 2\eta\sigma$

$3K - 2\eta = 2\eta\sigma + 6K\sigma$

$3K - 2\eta = \sigma\,(2\eta + 6K)$

$\frac{3K - 2\eta}{2\eta + 6K} = \sigma$

$$\therefore \sigma = \frac{3K - 2\eta}{2(3K + \eta)}$$

This is an expression for Poisson's ratio in terms of elastic constants.

References:

1. Theory of Elasticity and Fracture Mechanics.Vijay G. Ukadgaonkar.
2. Physics For degree student. C.L. Arora and P.S. Hemne.
3. Third edition of Elasticity theory, application and numerical. Marine H. Sadd
4. Theory of elasticity. Sadhu Singh.
5. Theory Of Elasticity 2021 Edition Sitharam T.G
6. Mechanics. D.S. Mathur, P.S. Hemne

NEWTONIAN AND NON-NEWTONIAN FLUIDS

Hariom Singh Tomar

Department of Mathematics

Chintamani College of Arts and Science,

Gondpipri, Dist- Chandrpur (M.S.) 442 702

Corresponding author E-mail: hstomar5@gmail.com

Blood/Fluid can be divided into two ways on the basis of shearing stress and rate of strain is as follows.

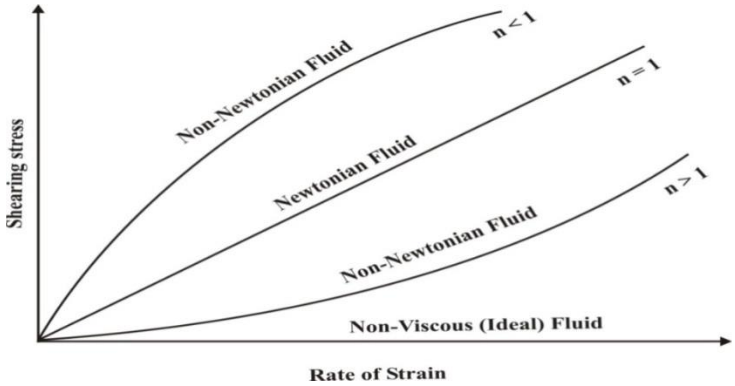

(i) Newtonian fluid

If $\tau = \mu e$, then fluid is called Newtonian viscous fluid where

τ = Stress

μ = Rate of deformation

e = Strain rate

(ii) Non-Newtonian fluid

If $\tau = \mu e^n$, $n < 1$ or $n > 1$ then fluid is said to be non-Newtonian fluid i.e. for which stress becomes non- linear, nonhomogeneous function of strain rate, such fluids are called non-Newtonian fluid, it may also of the form $\tau = \mu e + \tau_0$, $\tau \geq \tau_0$ where τ_0 is initial stress.

Some important non-Newtonian fluidare.

(a) Hershel - Bulkley fluid

$$\tau = \mu e n + \tau_0, \qquad \tau \geq \tau_0$$

(b) Casson fluid

$$\tau^{1/2} = \mu^{1/2} e^{1/2} + r_0^{1/2}, \; \tau \geq \tau_0$$

(c) Power law fluid

$$\tau = \mu e^n$$

(d) Ellis fluid

$$e = A\tau + B\tau^{n}$$

(e) Oka's equation

$$\frac{d\tau}{\tau + C} = K\frac{de}{(e+B)^{\beta}}$$

(f) Prandtleqution

$$\tau = A\sin^{-1}\left(\frac{e}{C}\right)$$

Classification of Non-Newtonian Fluid:

Non-Newtonian fluid has been classified into two main categories: (A) Inelastic Non-Newtonian fluid and (B) viscoelastic Non-Newtonian fluid. The first one can be subdivided into two types (i) visco-inelastic fluids or time independent and (ii)visco-elastic fluids or time independent.

(A) Inelastic Non-Newtonian fluid:

(i) Time independent Non-Newtonian fluid:

In the Time-independent fluids properties such as viscosity does not depends on time. The non-linearity relation between the shear stress and strain rate at a given point is solely written by the following way:

$\tau = f(\dot{\gamma})$

Where, τ and $\dot{Y}$ are the shear stress and shear rate.

The Time independent Non-Newtonian fluid can be subdivided into three varieties depending on the form of function of above equation:

(i) Pseudo plastic (shear thinning)
(ii) Dilatant (shear thickening)
(iii) Viscoelastic

Pseudo plasticfluids or shear-thinning fluids often exhibit a apparent viscosity which decreases with increasing stress. Polymer solutions, polymer melts, printing inks and blood are the pseudo plastic fluids. Dilatants often referred as shear-thickening fluids, exhibit viscosity increase with increasing shear rate. Gum solution, aqueous suspensions of titanium dioxide, wet sand, starch suspensions are treated as dilatants fluids. Shear-thinning behaviour is more common than shear-thickening.

(ii) Time-Dependent Fluids:

In these types of fluids apparent viscosity depends on the time of applied shear along with strain train rate. Such types of liquids are regarded as complex non-Newtonian fluid. It is recognized that there are two main classes of time-dependent fluids: (a) thixotropic and (b) rheopectic.

Thixotropic fluid: (Means changing)

It is most important fluid which exhibits time-dependent shear thinning property. Some more viscous fluids such as gels under static conditions cannot flow but when external force applied or stressed. Such types of fluid acquire the property of flow due to low viscosity. They take a stationary time to return to its previous state.

Rheopectic fluid:

It is a rare property of a time-dependent of some non-Newtonian fluids in which viscosity increase with time. Examples of some rheopectic fluids are lubricants. The viscosity of these types of fluids increase i.e. thickens or solidifies when shaken for a long time. The longer the fluid undergoes shearing force, the higher its viscosity. Sometimes the rheopectic behaviour of fluid may be considered as time-dependent dilatant behaviour.

The theories of the time-dependent fluids are less developed. In spite of many proposed models for the time-dependent fluids in the several literatures here two common models have been presented.

(B) Viscoelastic fluids:

Viscoelastic fluids are those that illustrate partial elastic recovery upon the removal of a deforming stress. Such materials possess properties of both fluids and elastic solids and obey Hooke's law of elasticity. For viscous fluids constitutive equation can be written as:

$$\gamma^{\cdot} = \frac{\tau}{\pi} + \frac{\dot{r}}{k}$$

Where, Ẏ and κ are the shear rate and rigidity modulus respectively.

References:

1. Briant J., J. Denis, G. Parc, (1989): Rheological Properties of Lubricants (Editions Technip, Paris)
2. George H.F., Qureshi F. (2013): Newton's Law of Viscosity, Newtonian and Non-Newtonian Fluids. In: Wang Q.J., Chung YW. (eds) Encyclopedia of Tribology. Springer, Boston, MA.
3. https://blog.craneengineering.net/what-are-newtonian-and-non-newtonian-fluids
4. https://www.frontiersin.org/articles/10.3389/fphy.2019.00071/full

NANOTECHNOLOGY: A REVIEW

Jeevarathinam Antony
Department of Home Science,
V. V. Vanniaperumal College for Women,
Virudhunagar, Tamilnadu, India
Correspopnding author E-mail: jeevsrathi@gmail.com

Abstract:

Nanotechnology deals with the materials size from 1 to 100 nm in length. The nanomaterials are using in many process of science and technology. Due to the change in life style the human needs also changed. The people expectations were also increased. They expect many features such as long lasting, eco-friendly products. It creates the path to nanotechnology to enter into the world. Nanoparticles are being used for various fields such as cosmetics or clothes, agriculture, environment and medicine. Due to their exceptional properties including Nanotechnology gives the specific properties such as antimicrobial activity, durability, and water repellence, antibacterial activity, high resistance to oxidation and high thermal conductivity have attracted considerable attention in recent years.

Introduction:

Nanotechnology is the science that deals with matter at the scale of 1 billionth of a meter (i.e., 10 −9 m = 1 nm), and is also the study of manipulating matter at the atomic and molecular scale. It exploits unique chemical, physical, electrical, and mechanical properties that emerge when matter is structured at the nano scale (Cristina Buzea *et al.,* 2007). Advancement in technology transformed the whole world. Nanotechnology is one of the field which is involved in changing of world. The idea of nanotechnology was initially presented by Richard Feynman in the year 1959, through his speech "There's Plenty of Room at the Bottom", which was delivered at an American Physical Society conference, at the California Institute of Technology (Feynman, 1959). The term Nanotechnology‟ was coined by Prof. Norio Taniguchi, Tokyo Science University in 1974 to describe the precision manufacture of materials with nanometres tolerances and was unknowingly appropriated by Drexler in his 1986 book „ Engines of creation: The Coming Era of Nanotechnology (Melgardt, 2008).

The term “nano” means one-billionth or 10^{-9} henceforth, one nanometer is referred to as one billionth of a meter. The nanomaterial exists in a very small scale (10^{-6} of a millimetre) as exemplified, a human hair is about 80000 nanometers and our hereditary DNA molecule (chromosome) is about only 5-10 nanometers. Nanoparticles or nanomedicines are 100-10000 times smaller than a human cell (~20-50 μm) and much smaller than microorganisms (~1-5 μm) that to be targeted or to be modified (figure 1).

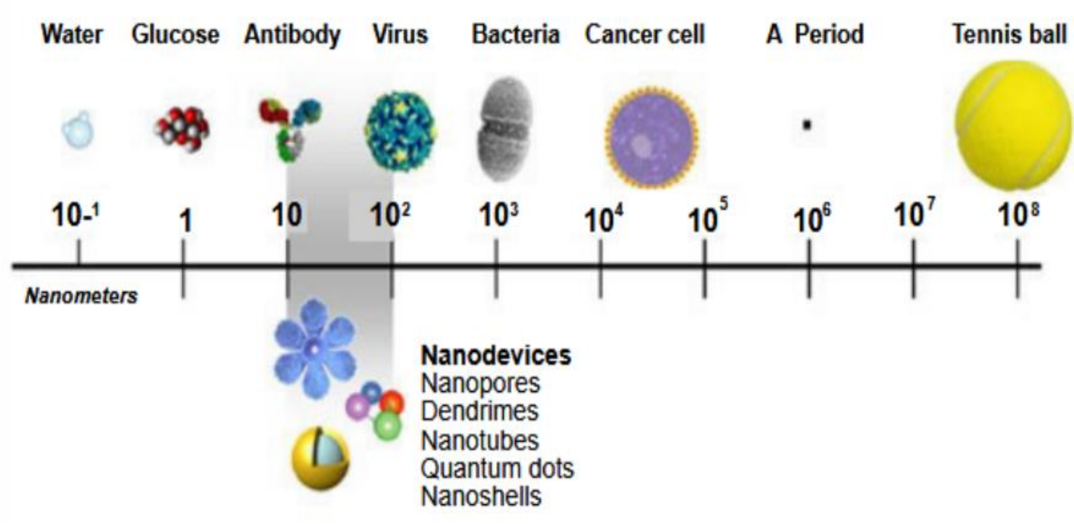

Figure 1: Size of Nanoparticles

Approaches for Nanoparticles synthesis

There are two general approaches for the synthesis of nanomaterials as shown in Figure 2.They are (1) bottom-up approach and (2) top-down approach (Iqbal *et al.,* 2012).

In bottom-up approach refers to the synthesis of nanoparticles by means of chemical reactions from the bottom: atom-by-atom, molecule-by-molecule, or cluster-by cluster. Various methods that use bottom-up techniques include supercritical fluid synthesis, plasma or flame spraying synthesis, laser pyrolysis, molecular condensation, the sol gel process and chemical reduction .

In Top-down approach involves mechanical methods to the breakdown the bulk material into several parts to form nanosized structures or particles. Various metallic nanoparticles are composed of top-down methods such as etching, sputtering, and laser ablation.

The techniques are categorized into physical, chemical, and biological techniques for synthesizing nanoparticles for both top-down and bottom-up approaches. The idea about these methods given in the figure 3 and 4. While bottom-up strategy suggests that nanoparticles are synthesized to the required material from smaller molecules. Chemical reduction is mostly used in this technique, sometimes combined with the capping agent for nanoparticles synthesized stabilizing purposes. But the chemical method synthesis causes environment harm due to release of chemical substances.

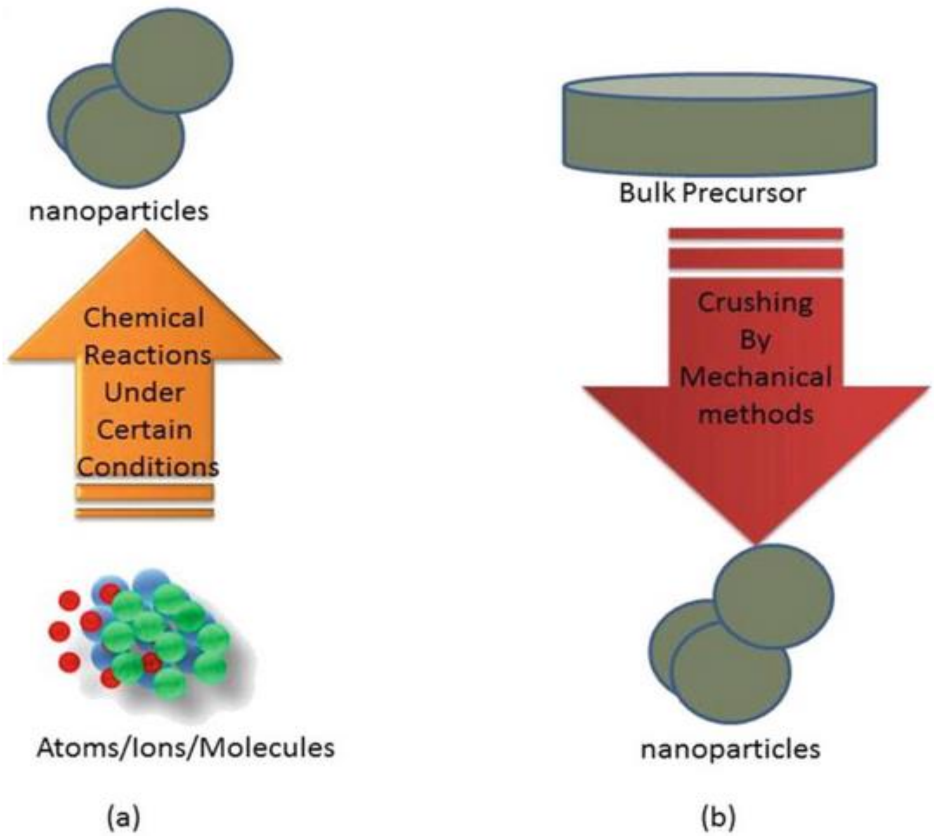

Figure 2: Synthesis approaches for nanoparticles (a) bottom-up and (b) top-down approaches source:https://www.intechopen.com/chapters/71200)

Biological method of nanoparticle synthesis is also categorized under bottom-up approach, where biomolecules incorporate with metallic substances for nanoscale material production. The biological method is preferred over the other two conventional as it is a green method, environmentally friendly, and does not require higher energy consumption (Santheraleka Ramanathan *et al.,* 2021).

Nanoparticles obtained through the biological approach have a greater specific surface area, increase the rate of catalysis, and have metal salt and improved enzymes (Liang *et al., 2012*). The use of biological materials, such as bacteria, yeast, mold, microalgae and plant extracts, to synthesize nanoparticles has some advantages like less energy consumption and moderate technology without using toxic chemical (Mie *et al.,* 2014). Biological sources that are used for nanoparticle synthesis provide a simple method and easy increase in biomass, ensuring a uniform particle size, as well as multiplication. The use of microbes is one of the most prominent methods among the biological approaches of nanoparticle synthesis. A generalized schematic representation of green synthesis of NPs is shown in figure 5.

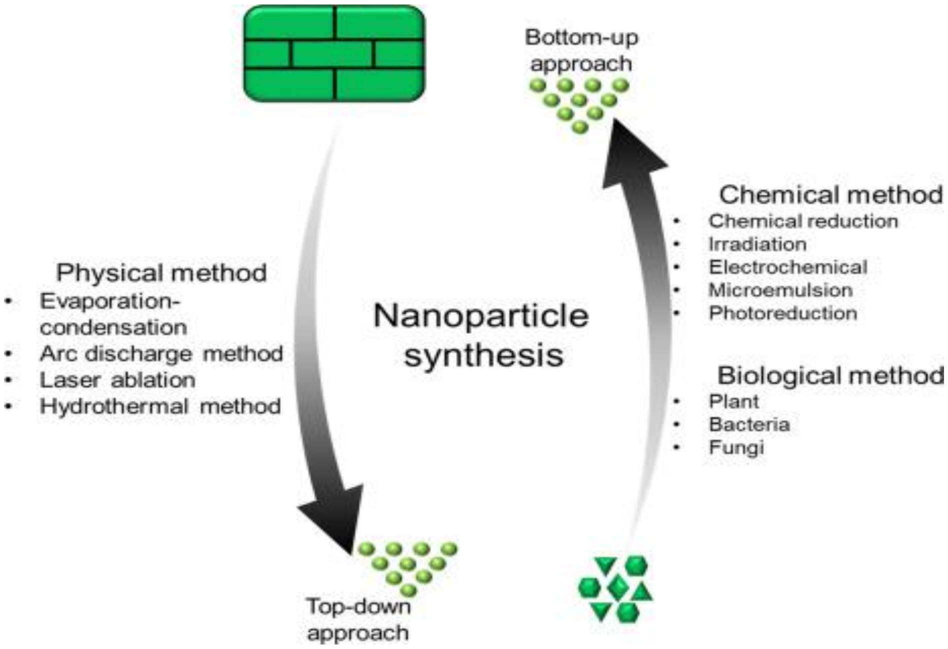

Figure 3: Schematic illustration of top-down and bottom-up approach in nanoparticle synthesis *(Santheraleka Ramanathan et al., 2021)*

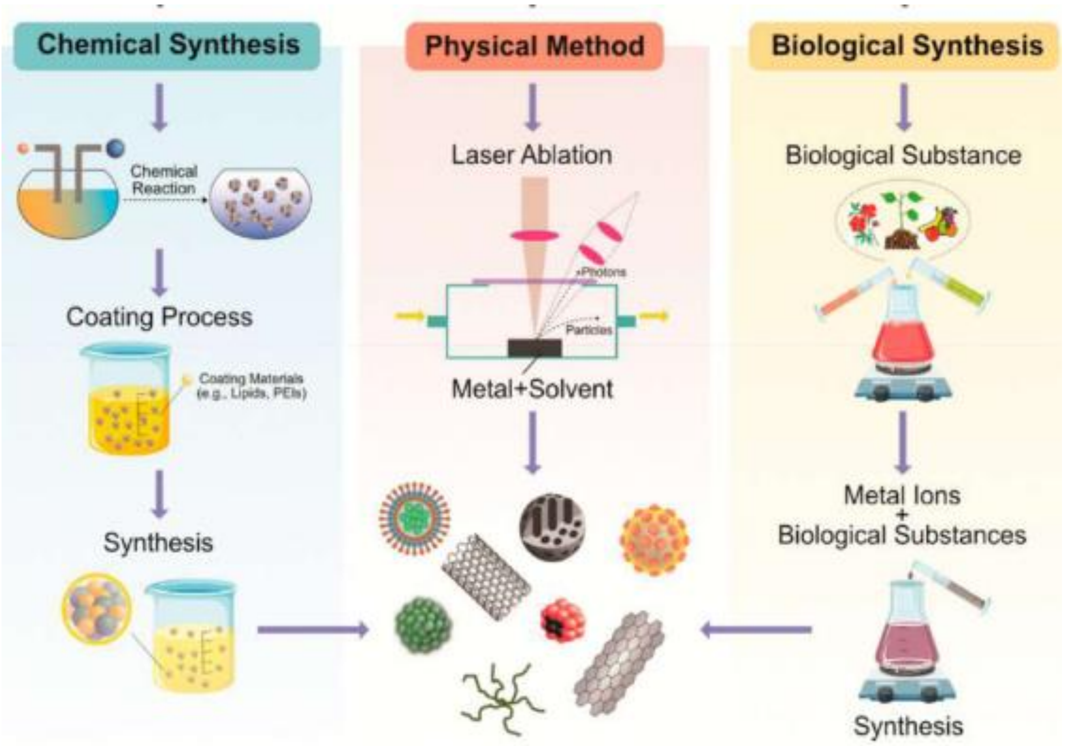

Figure 4: Different method of Nanoparticle synthesis (Muniyandi Jeyaraj *et al.*, 2019)

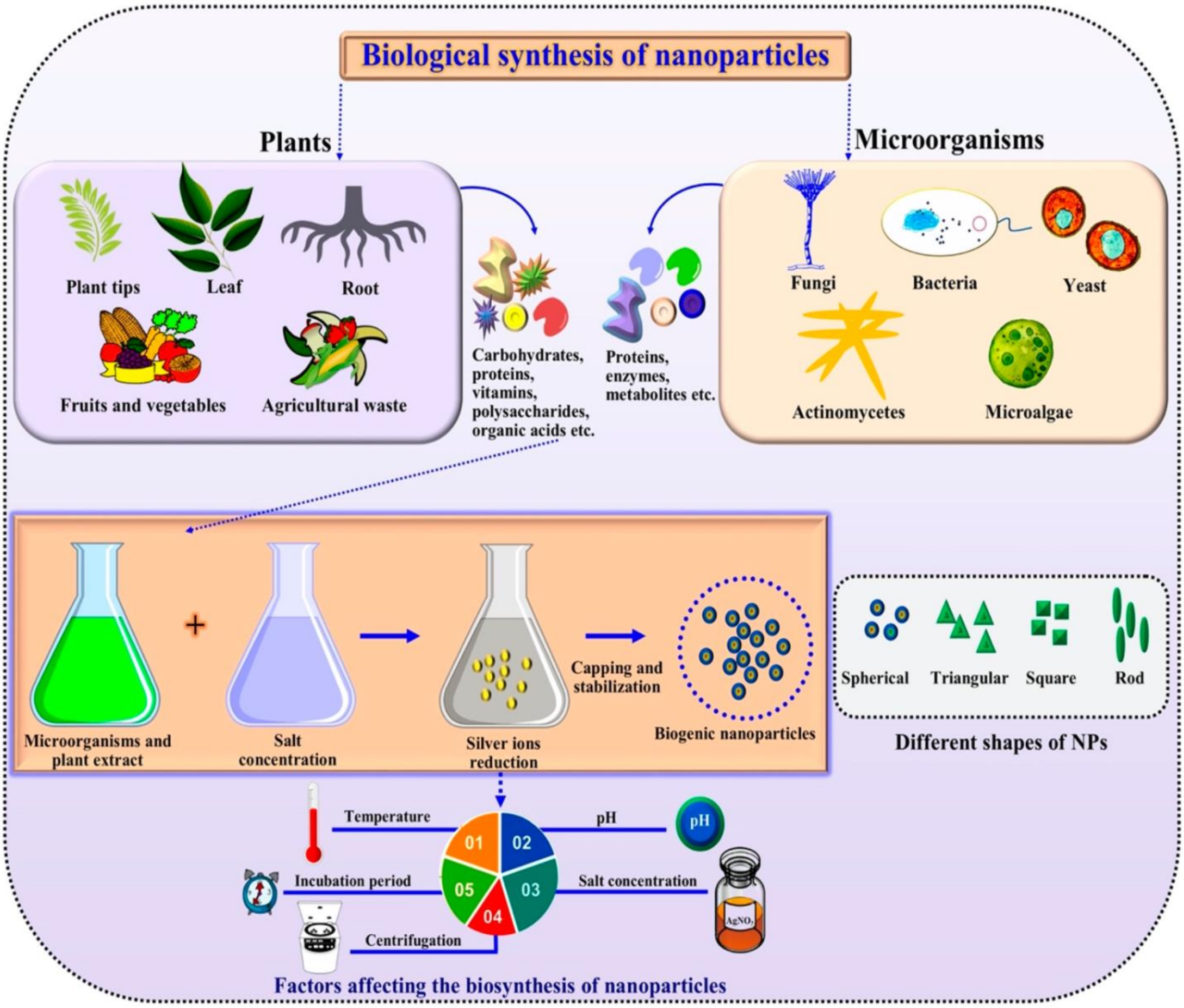

Figure 5: Generalized schematic representation of green synthesis of metallic nanoparticles (Md. Arshad Ali *et al.,* 2020)

Green synthesis of NPs is a cost-effective and eco-friendly technique that does not use toxic chemicals. This technique employs a number of reducing and stabilizing agents like microbes, plants and other natural resources to produce NPs for sustainable in manner (Ogunyemi *et al.,* 2019). The green synthesis of NPs has gained much attention due to it being eco-friendly, cost effective and highly stable (Dhuper *et al.,* 2012). Several studies have reported the production of NPs using plants and microorganisms (Korbekandi *et al.,* 2016). The green synthesis methods of NPs are diversified, but organisms or their extracts are simply reacted with a metallic salt and then biological reduction is carried out to convert the metal to NPs. The produced NPs are readily available to use after proper characterization (Mittal *et al.,* 2013).

Microbe-mediated synthesis of nanoparticles is a green approach that utilizes bacteria, fungi, viruses and their products for the production of nanoparticles. In comparison to microbial synthesis as a potential technique, plants can be used in convenient manner for nanoparticles production. The synthesis of nanoparticles can be scaled up easily by using plant extracts. In addition, the plant extracts can reduce metallic ions more quickly than microbes and produce stable metallic nanoparticles (Iravani *et al.,* 2011). In plants extracts, many compounds like polysaccharides, proteins, amino acids, organic acids and phytochemicals like polyphenols, flavonoids, terpenoids, alkaloids, tannins, and alcoholic substances are present that can reduce and stabilize the nanoparticles (Ahmed *et al.,* 2017).

Applications of Nanotechnology:

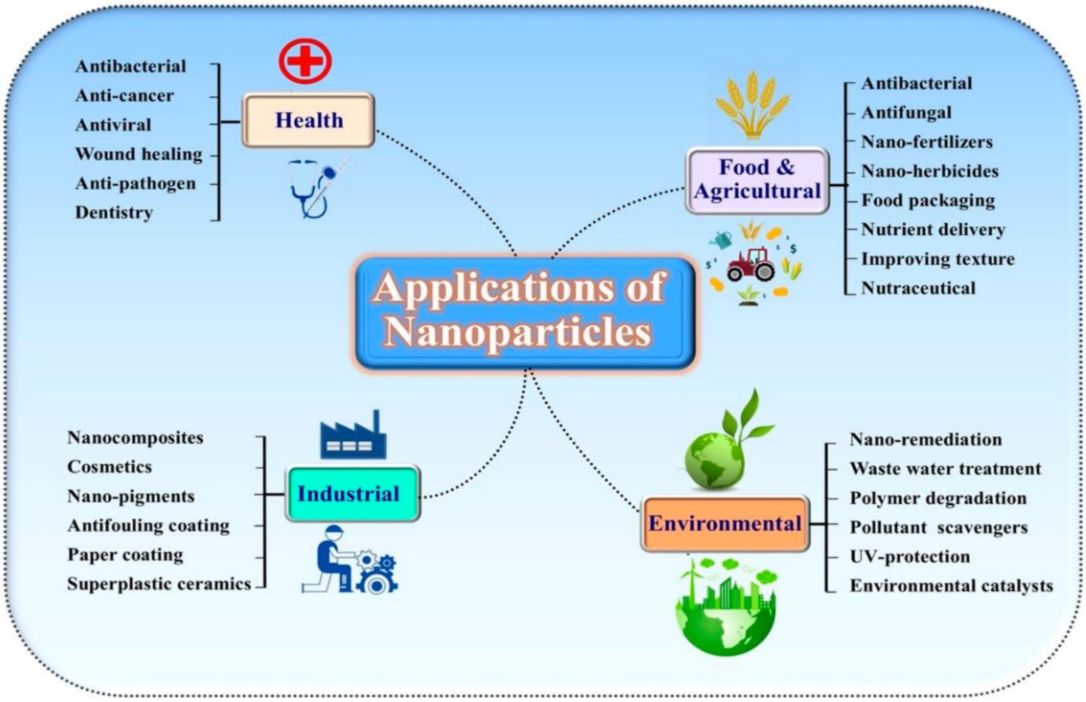

Figure 6: Application of nanoparticles in various fields

Nanoparticles, nanofluids, nanowires and nanofilms all give rise to implausible applications in the field of science and technology i.e. microbiology, optics, electronics, textiles, biomedical, coatings, aerospace, materials science, energy, plastics and mechanics etc. Conventional materials impregnated with nanoparticles possessing enhanced properties owing to large surface area of nanoparticles. A visible shift of change in properties has been seen while moving from microscopic to nanoscopic level (Hashim, 2012).

a) Applications in Textile

The application of nanoparticles in textile field causes the remarkable changes in the quality of life. Fabrics produced with Nanotechnology has specific properties such as static protection, self-cleaning, shrink resistance, stain resistance, fire resistance, electrical conductive, fragrance release, UV protection, water repellent (hydrophobic), moisture management, high strength, antimicrobial and wrinkle resistance.

Figure 7: A diagrammatic representation of various utilizations of nanotechnology-based textiles. Reproduced from reference (Yetisen *et al.*, 2016)

Nano textiles are used now days numerously, it ranges from fashioned technological clothing to protective occupational dresses, environmental waste savings to functional finished clothing. The application of nanotechnologies to textiles affords an expanded array of properties with potential for improved and novel use in materials and products (Brian, 2012). Nanotechnology can reduce the use of water as the nanostructure and surface functionality can be imparted using dry techniques on fabric ((Joshi, 2011). It has a great effect on environment and the process is also eco friendly.

The nanotechnology utilized in textile field in the following ways.

a) Nanofinished textiles

The nanofinished textiles are commercially available such as nanospherenanocare, lotus effect in fashion world. One of the earliest uses of nanofinish in fabric finishing was in surface coating for soil repellency and soil release properties. It has certain benefits over traditional finishing, which are principally: (i) In general, in the case of nanofinishing, it only requires a lesser quantity of nanomaterials relative to bulk materials utilized in traditional finishing, for obtaining a similar effect. (ii) They do not influence the aesthetic feel of the textile materials. (iii) These nanofinishings are more durable due to the increased surface area-to-volume ratio of nanomaterials along with its homogenous distribution in textile material. (iv) Certain functionalities that are hard to attain by traditional finishes could possibly be developed by nanofinishing (Gokarneshan *et al.,* 2018 and Ghosh *et al.,* 2020).

b) Nanocomposite textiles

A nanocomposite is a material where one of the dimensions/phases is less than 100 nanometers (nm). It has been found that by appropriate addition of nanoparticles to a polymer matrix its performance can be enhanced dramatically (Mandat *et al.,* 2012). Various textile fabrics have been treated with the nanocomposites developed to improve their fire retardancy and antibacterial properties.

c) Nanofibrous textiles

Nanofibers possess high surface area to volume area and small pore size with significantly improved chemical, mechanical, and biological properties as diameter decreases to nanoscale (Khan *et al.,* Parhizkar *et al.,* and Manea *et al.,* 2017). Therefore, nanofibers have attracted an attention of research over the few decades in the various fields of life. One of them is the medical textile, due to nanofibers' biocompatibility, biodegradability, non-biodegradability, strength, elongation, and porosity (Salehi *et al.,* 2017 and Senel-Ayaz *et al.,* 2018). Therefore nanofibers can be promising materials for many biomedical applications including the production of artificial blood vessels (Ma *et al.,* 2005), scaffolds for engineered tissues (Duan, 2013), wound dressings (Chen *et al.,* 2008), and filter (Yun, 2007). There are various techniques used in fabrication of nanofibers but electrospinning is the convenient method because of its low rate and high production rate.

2) Application in medicine

The application of nanotechnology in the health sciences has given rise to nanomedicine, a new discipline that aims to develop tools for diagnosing, preventing and treating diseases at an early stage of their development (Lechuga *et al.,* 2011). Nanomedicine is an interdisciplinary field in which nanoscience, nanoengineering and nanotechnology interact with the life sciences. It is expected that nanomedicine will lead to the development of better devices, drugs and other applications for early diagnosis or treatment of a wide range of diseases with high specificity, efficacy and personalization with the aim of improving the quality of life of patients. Because of its broad scope, it is expected that nanomedicine can be involved in all aspects of medicine, i.e., enter into conventional clinical practice. Nanomedicine differs from other types of conventional medicines in that it involves the development and application of materials and technologies with nanometric length scales (Pelaz *et al.,* 2017). Nanomedicine covers three main areas: nanodiagnosis, controlled drug delivery (nanotherapy), and regenerative medicine.

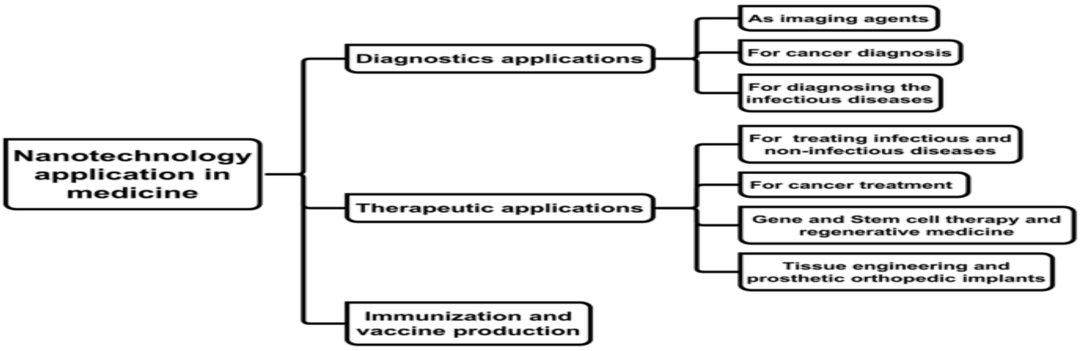

Figure 9: Applications of nanotechnology in medical field (Amr El-Sayed *et al.*, 2019)

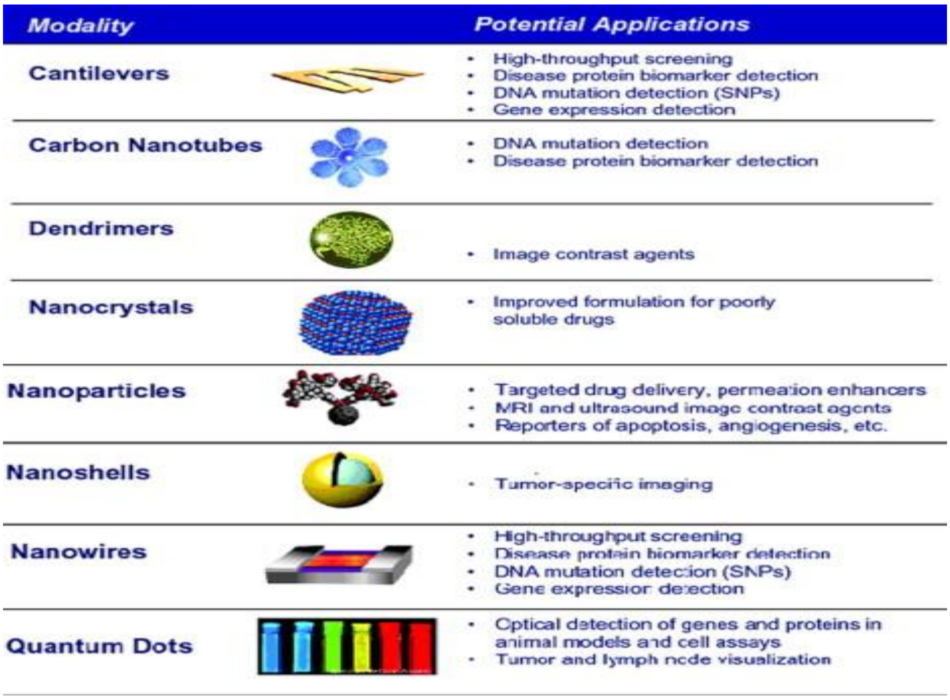

Modality	Potential Applications
Cantilevers	• High-throughput screening • Disease protein biomarker detection • DNA mutation detection (SNPs) • Gene expression detection
Carbon Nanotubes	• DNA mutation detection • Disease protein biomarker detection
Dendrimers	• Image contrast agents
Nanocrystals	• Improved formulation for poorly soluble drugs
Nanoparticles	• Targeted drug delivery, permeation enhancers • MRI and ultrasound image contrast agents • Reporters of apoptosis, angiogenesis, etc.
Nanoshells	• Tumor-specific imaging
Nanowires	• High-throughput screening • Disease protein biomarker detection • DNA mutation detection (SNPs) • Gene expression detection
Quantum Dots	• Optical detection of genes and proteins in animal models and cell assays • Tumor and lymph node visualization

Figure 10: Types of nanodevices are used in clinical Application (Khalid Khalaf Alharbi, 2014)

a) Nanodiagnostics:

In general, nanodiagnosis is considered as the design and development of analytical and imaging systems that allow for the detection of disease or abnormal cell function in early stages, both in vivo and in vitro (Lechuga *et al.,* 2011). Nanomaterials can be used for in vivo diagnosis, being used as contrast agents to visualize tissue structures inside the human body and to delimit healthy vs. pathological tissues. To this end, NPs are designed with different contrast properties for different modalities, such as computed tomography (CT), magnetic resonance imaging (MRI), positron emission tomography (PET), single photon emission computed tomography (SPECT) or fluorescence imaging. NPs will be designed to target specific tissues and generate the contrast.

b) Controlled drug release:

Bearing in mind the complexity, the conventional drug delivery system cannot deliver the chemotherapeutic agents in the most effective concentration to cause tumour cell death, and debilitating side effects occur. This has led to the development of NPs as a drug delivery system with the aim of achieving tumour specificity and improving the therapeutic index and pharmacokinetic profile of chemotherapeutic agents (Fernandes *et al.,* 2018). Thus, nanotherapy may allow for target active nanosystems containing recognition elements to act or transport and release drugs specifically on affected areas or cells, with the goal of achieving more effective treatment with fewer side effects (Lechuga *et al.,* 2011).

c) Regenerative Medicine:

Regenerative medicine aims to repair or replace damaged tissues and organs using nanotechnology tools (Lechuga *et al.,* 2011). Nanomaterials designed to deliver drugs or perform some action on diseased tissue are programmed to degrade later, but nanomaterials that are not removed and remain performing their function continuously are also being synthesized. These nanomaterials will allow for surface modelling and provide new functions in tissue engineering, such as new properties of implants. One example is carbon nanostructures, which are biocompatible and support the growth and proliferation of different cell types (Pelaz *et al.,* 2017).

d) Applications in agriculture

Technical innovations in agriculture are prime necessity to combat worldwide challenges of population boost, climate change and restricted food availability. Sustainable agricultural intensification is a concept aimed at increasing food production from the same existing farmland without adverse environmental impacts (The Royal Society, 2009). The application of nanotechnology approach to agricultural crop handouts is one of the proposed apparatus for sustainable agricultural intensification. Nanotechnology potential is explored in agriculture sector to chop applications of plant protection aggregates, lowers nutrient losses, promotes rapid pest detection and ameliorates yields through improved nutrient management (Ghormade et *al*., 2011). The broad range of nanotechnology applications in agriculture given in the figure 11.

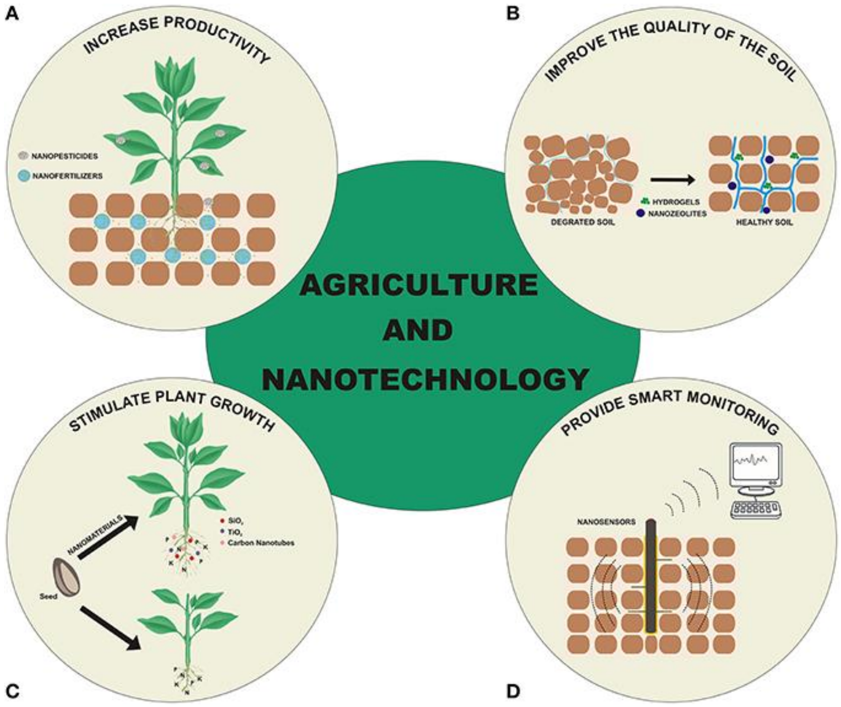

Figure 11: Potential applications of nanotechnology in agriculture (Fraceto *et al.*, 2016)
(A) Increase the productivity using nanopesticides and nanofertilizers;
(B) Improve the quality of the soil using nanozeolites and hydrogels;
(C) Stimulate plant growth using nanomaterials (SiO_2, TiO_2, and carbon nanotubes);
(D) Provide smart monitoring using nanosensors by wireless communication devices

Conclusion:

The introduction of nanoparticles in the world has resulted in the reduction of waste material and also production of labile biologically active substances in the field of agriculture, textile and medicine etc to improve the life. It also eradicates the diseases which affect the human and promise the healthy life. It also helps in the economic development of the nation.

References:

1. Ahmed, S., S.A. Chaudhry, S. Ikram (2017): A review on biogenic synthesis of ZnO nanoparticles usingv plant extracts and microbes: A prospect towards green chemistry, J. Photoch. Photobiol. B ,166 : 272–284.
2. Amr El-Sayed and Mohamed Kamel (2020): Advances in nanomedical applications: diagnostic, therapeutic, immunization, and vaccine production, Environmental Science and Pollution Research, 27: 19200–19213.

3. Brian Haydon (2012): Nanomaterials and their Applications in Textiles-Standards, Domestic Standardization for Canadian Manufacturers and Importers and International Standardization Developments, Multimedia Services Section, Canada industry: 1-36.
4. Chen, J.P., G.Y. Chang and J.K. Chen (2008): Electrospun collagen/ chitosan nanofibrous membrane as wound dressing, Colloids and Surfaces A: Physicochemical and Engineering Aspects : 313, 183-188.
5. Cristina Buzea , I. Ivan, Pacheco Blandino and Kevin Robbie (2007): Nanomaterials and nanoparticles: Sources and toxicity, Biointerphases , 2(4): MR17 - MR172.
6. Dhuper, S., D.Panda and P.L.Nayak (2012): Green synthesis and characterization of zero valent iron nanoparticles from the leaf extract of Mangifera indica. Nano Trends, J. Nanotechnol. Appl. 13: 16–22.
7. Duan, B., X. Yuan, Y. Zhu, Y. Zhang, X. Li, Y. Zhang and K. Yao (2006): A nanofibrous composite membrane of PLGA – chitosan/PVA prepared by electrospinning, European Polymer Journal , 42 : 2013-2022.
8. Fernandes, C, D. Suares and M.C.Yergeri (2018): Tumor Microenvironment Targeted Nanotherapy, Front.Pharmacol. 9: 1230.
9. Feynman, R.P(1959):There's plenty of room at the bottom, Eng. Sci., 23: 22–36.
10. Fraceto L.F., R.Grillo , G.A.de Medeiros, V.Scognamiglio, G. Rea and C. Bartolucci (2016): Nanotechnology in Agriculture: Which Innovation Potential Does It Have? , Front. Environ. Sci. 4:20.
11. Ghormade V, M.V. Deshpande, K.M. Paknikar (2011): Perspectives for nano-biotechnology enabled protection and nutrition of plants, Biotechnol Adv, 29:792–803
12. Ghosh, S.,T. Smith, S. Rana, P.Goswami (2020): Nanofinishing of Textiles for Sportswear, World Textile Information Network: Dublin, Ireland.
13. Gokarneshan, N., K.Velumani (2018): Significant Trends in Nano Finishes for Improvement of Functional Properties of Fabrics. In Handbook of Renewable Materials for Coloration and Finishing, Scrivener Publishing LLC: Beverly, MA, USA: 387–434.
14. Hashim A.A. (2012):Smart nanoparticles technology. InTech publishers, Croatia.
15. Iqbal P, J.A.Preece , P.M.Mendes (2012) : Nanotechnology: The "top-down" and "bottom-up" approaches , In Supramolecular Chemistry: From Molecules to Nanomaterials, J. W. Steed, P. A. Gale, eds., John Wiley & Sons Ltd, Chichester, UK : 3589-3602.
16. Iravani, S (2011): Green synthesis of metal nanoparticles using plants. Green Chem. 13: 2638–2650.

17. Joshi,M. and A Bhattacharyya (2011): Nanotechnology-a new route to high performance functional textiles, Textile Progress,43(3):155-233.
18. Khalid KhalafAlharbi and Yazeed A.Al-sheikh **(**2014**):** Role and implications of nanodiagnostics in the changing trends of clinical diagnosis**,** Saudi Journal of Biological Sciences , 21(2)**:**109-117.
19. Khan M.Q, L.Hoik , M.K.Jun, K.Zeeshan, S.Jianhua , S.I.Seung, Z.Chunhong , S.K.Ick (2017): Self cleaning effect of electro spun poly (1, 4-cyclohexanedimethylene iso sorbide terephthalate) nanofibers embedded with zinc oxide nanoparticles, Text Res J., 88(21):2493-2498.
20. Korbekandi, H., S.Mohseni, R.Mardani Jouneghani, M.Pourhossein, S.Iravani (2016): Biosynthesis of silver nanoparticles using Saccharomyces cerevisiae, Artif. Cells Nanomed. Biotechnol. 44, 235–239.
21. Lechuga, L (2012):Nanomedicina: Aplicación de la Nanotecnología en la Salud; Digital.csic.es.
22. Liang, X.J., A.Kumar, D. Shi, D.Cui, D (2012): Nanostructures for medicine and pharmaceuticals, J. Nanomater, 921897.
23. Ma, Z., M. Kotaki, T. Yong, W. Heb, S. Ramakrishna (2005): Surface engineering of electrospun polyethylene terephthalate (PET) nanofibers towards development of a new material for blood, vessel engineering, Biomaterials 26 : 2527-2536.
24. Mandat.,A.A., B.H. Chaudhar (2012): Patelanocomposite: manufaduring and applications in textiles , Melliand International · August 2012: 188-191.
25. Manea L.R., P.Alexandru , P.B.Andrei (2017) : Medical applications of functional electrospun nanofibers-a review, Key Eng Mater 752:132–138
26. Md. Arshad Ali , Temoor Ahmed , Wenge Wu , Afsana Hossain , Rahila Hafeez , Md. Mahidul Islam Masum , Yanli Wang , Qianli An , Guochang Sun and Bin Li (2020): Advancements in Plant and Microbe-Based Synthesis of Metallic Nanoparticles and Their Antimicrobial Activity against Plant Pathogens , Nanomaterials 10: 1146.
27. Melgardt M de Villiers(2008): Pharm Tech, 98.
28. Mie, R., M. W. Samsudin, L.B.Din, A. Ahmad, N.Ibrahim, S.N.Adnan (2014): Synthesis of silver nanoparticles with antibacterial activity using the lichen Parmotrema praesorediosum, Int. J. Nanomed. 9: 121–127.
29. Mittal, A.K., Y.Chisti, U.C. Banerjee (2013): Synthesis of metallic nanoparticles using plant extracts, Biotechnol. Adv, 31: 346–356.

30. Muniyandi Jeyaraj, Sangiliyandi Gurunathan, Muhammad Qasim, Min-Hee Kang and Jin-Hoi Kim.(2019): A Comprehensive Review on the Synthesis, Characterization, and Biomedical Application of Platinum Nanoparticles, *Nanomaterials, 9*(12): 1719.
31. Ogunyemi, S.O., Y.Abdallah, M. Zhang, H. Fouad, X. Hong, E. Ibrahim, M.M.L.Masum, A.Hossain, J.Mo, B.Li (2019):Green synthesis of zinc oxide nanoparticles using different plant extracts and their antibacterial activity against Xanthomonas oryzae pv. Oryzae, Artif. Cells Nanomed. Biotechnol, 47: 341–352.
32. Parhizkar M, M. Suntharavathanan , H.Shervanthi , E.Mohan (2018): Latest developments in innovative manufacturing to combine nanotechnology with healthcare, Nanomedicine, 13:5–8
33. Pelaz B, C.Alexiou, R.A. Alvarez-Puebla, F.Alves, A.M. Andrews, S.Ashraf, L.P. Balogh, L.Ballerini, A. Bestetti, C. Brendel (2017): Diverse Applications of Nanomedicine, ACS Nano 11: 2313 - 2381.
34. Salehi S, K. Mahshid , M.Nafiseh , F.Afsoon , T.Ali (2017): Medical textiles as substrates for tissue engineering, In Textile finishing recent developments and future trends. Wiley Beverly, Hoboken: 363–421.
35. Santheraleka Ramanathan, C.B.Subash, Gopinath, Veeradasan Perumal (*2021):* Nanoparticle synthetic methods: strength and limitations, Nanoparticles in Analytical and Medical Devices*, Science Direct: 31-43.*
36. Senel-Ayaz HG, H.Yah-El , A.Hasan , I.L.Peter (2018): Textile technologies for 3D scaffold engineering, In Functional 3D tissue engineering scaffolds, M. Liebert Inc. Publisher, New York: 175–201
37. The Royal Society (2009) :Reaping the benefits: science and the sustainable intensification of

    global agriculture. The Royal Society, London
38. Yetisen, A.K, H.Qu, A.Manbachi, H.Butt, M.R.Dokmeci, J.P.Hinestroza, S.H.Yun (2016): Nanotechnology in textiles, ACS Nano ,10:3042–3068.
39. Yun,K.M., Ch. J. Hogan Jr., Y. Matsubayashi, M. Kawabe, F. Iskandar, K. Okuyama, (2007): Nanoparticle filtration by electrospun polymer fibers, Chemical Engineering Science , 62: 4751- 4759.

VISCO-ELASTIC FLUIDS OR TIME-DEPENDENT FLUIDS

Hariom Singh Tomar
Department of Mathematics,
Chintamani College of Arts and Science,
Gondpipri, Dist- Chandrpur (M.S.) 442 702
Corresponding author E-mail: hstomar5@gmail.com

These fluids are characterized by the fact that the shear rate depends not only on the applied stress, but, in addition, on the duration of the stress. Fluids which show a decrease in viscosity with time under isothermal conditions and steady shear are called thixotropic while those fluids which show increase in viscosity are called rheopectic. The thixotropic fluids are more common thenrheopectic fluids and are of great importance in industries.

The behavior of a time-dependent fluid is attributed to the sequence of molecular structural changes and the knowledge, regarding the mechanism of breaking and of a deformation of the molecular changes, lacks precision. Also, the mathematical representation involves a large number of co-ordinates even to define the shape and operation of molecular changes. Due to these handicaps, no definite constitutive equation for such fluids has been proposed so far.

There are materials for which a suddenly applied and maintained state of uniform stress induces an instantaneous deformation, followed by a flow process which may or may not be limited to magnitude, as time grows. A material which responds in this manner is said to exhibit both an instantaneous elastic effect and creep characteristics. This behavior is clearly not described either by elasticity or viscosity theory but combines features of both. Hence, they are called visco-elastic materials.

When a visco-elastic fluid is in motion, a certain amount of energy is stored up in the material as strain energy while some energy is lost due to viscous dissipation. In this class of fluids, unlike the case of purely viscous fluids, the strain, however small, can not be neglected, as it is responsible for the recovery to the original state and for the reverse flow that may follow the removal of the stress. During the flow, the natural state of the fluid changes constantly and tries to attain the instantaneous state of deformation but never succeeds completely. This leg is a measure of elasticity of the so called ‘memory’ or elastic response of the fluid. In the formulation of the rheological models or constitutive equations, an account of this memory is taken by introducing ‘stress relaxation times’ and ‘strain-rate retardation times’. The problem of allowing for memory in rheological model has resulted in several theories of viscoelasticity. A number of workers like Oldroyd (1950, 1958), Lodge (1954), Dewitt (1955), Pao (1957), Green and Rivlin (1957), Noll (1958) and Walters (1960) have developed the constitutive equations ofvisco-elastic fluids.

For these fluids, the shear rate depends on the imposed stress and the extent of deformation so that.

$$\mu' = f(\tau, \gamma)$$

The Weissenberg ‘climbing’ effect was the pioneering work in this field. Weissenberg (1947, 1948) showed that elastic fluid ‘climb’ onto a sahft rotating within, in opposition to centrifugal forces. The Navier-Stoke's equations had, therefore, to be modified. The constitutive equations are derived from considerations of invariance and general assumptions regarding the variables occurring in these equations. A significant feature of such equations is that the choice of variables is motivated by physical conditions derived from practical experience.

There are two invariance conditions. The first expresses the fact that a simultaneous rotation of medium and reference system leaves the constitutive equation unchanged. The stress must, therefore, be capable of being expressed in terms of the basic kinematic variables like gradients of displacement, velocity and acceleration by means of systematic tensors defined in their terms. The second invariance condition expresses that the isotropy of the fluid in its undisturbed state imposes further restrictions on the way in which the stress must depend on these kinematic tensors.

We give below the description of four most well-known models:

(i) The Maxwell Model

One of the simplest model which can be constructed, is one spring and one dash-pot in series and is known as the Maxwell model.

$$\gamma_s = \frac{\tau}{G} \tag{1}$$

$$\dot{\gamma}_d = \frac{\tau}{\mu} \tag{2}$$

This is a fluid model since a constant applied stress will result in a continuous deformation due to unrestrained extension of the dash-pot.

The total strain, that is displacement of the model, is the sum of elastic strain γ_s of the spring and the fluid stream γ_d of the dash-pot. Thus,

$$\gamma = \gamma_s + \gamma_d \qquad (3)$$

Differentiating (3) with respect to time and with the help of (1) and (2), we get

$$\tau + \lambda \dot{\tau} = \mu \dot{\gamma} \qquad (4)$$

where, $\lambda = \frac{\mu}{G}$ is the relaxation time.

If $G \rightarrow \infty$ that is $\lambda \rightarrow 0$ the spring becomes a rigid connection and the model reduces to that of a Newtonian fluid.

Conversely, if $\mu \rightarrow \infty$ that is $\lambda \rightarrow \infty$, the dashpot becomes rigid and the model becomes that of a Hookean solid.

To get a feel for the behaviorof the Maxwell fluid, let us consider its response to a stress-relaxation test in simple shear, in which a shear strain of magnitude γ_0 is suddenly applied at time t = 0 and is held constant. If the initial extension were infinitely fast, the dash-pot would remain rigid, since an infinite strain-rate would require an infinite stress to expand it. Hence, only the spring will extend initially. If the extension is then maintained constant, however, the spring contraction force will react on the dash-pot causing it to extend as the spring relaxes.

Oldroyd (1953) proposed a more complicated equation

$$\tau + \lambda_1 \dot{\tau} = \mu\left(\dot{\gamma} + \lambda_2 \ddot{\gamma}\right) \qquad (5)$$

where, λ_1 is the relaxation time and λ_2 the retardation time. This means, that, if the motion is suddenly stopped, the shear stress decays as e^{-t/λ_1}. If all stresses are suddenly withdrawn, the rate of strain decays as e^{-t/λ_2}. In a normal oil, both G and λ_1 are small, but in oil paints, λ_1 is considerable, while G remains small. If λ_1 is small and G large, we have the description of a gel.

(ii) The Rivlin-Ericksen Model

This is the most general model put forward so far from purely phenomenological consideration.

Let visco-elastic isotropic material undergo deformation and let the components in the system of velocity, acceleration, second acceleration,......., nth acceleration at the instant be defined by $v_i(t), v_i^{(1)}, v_i^{(2)}(t), \ldots\ldots v_i^{(n)}(t)$ respectively.

It $\frac{D}{Dt}$ denotes the material time derivative, then,

$$v_i^{(\alpha+1)}(t) = \frac{D}{Dt} v_i^{(\alpha)}(t) \tag{6}$$

$$v_i^{(\alpha+1)}(t) = \frac{\partial v_i^{(\alpha)}(t)}{\partial t} + v_m^{(t)} \frac{\partial v_i^{(\alpha)}(t)}{\partial x_m(t)} \tag{7}$$

where, $\alpha = 0,1,2\ldots\ldots,(n-1)$

and $$v_i(t) = \frac{Dx_i(t)}{Dt} \tag{8}$$

where, a generic particle x_i in the rectangular cartesian frame x at some reference time t = 0 has co-ordinate $x_i(t)$ at a generic time t.

Rivlin and Ericksen (1955) assumed that the stress components τ_{ij} at a point x_i at time t are single valued functions of gradients in the system x of velocity, acceleration, ..., nth acceleration at the point x_i at time t, so that,

$$\tau_{ij} = f_{ij}\left(v_{p,q} v_{p,q}^{(1)} \ldots\ldots v_{p,q}^{(n)}\right)$$

where, p denotes differentiation with respect to x_p that is $x_p(t)$.

As observed by Nolls (1958), for a liquid, the only reference configuration is at the instant of measurement of the stress. Thus $X_i = x_i$.

In order to apply the mathematical model to high polymer solutions, it was assumed that stress components can be expressed as continuous functions of $x_{p,q}(t)$, the deformation gradient referred to the configuration at the instant of measurement and as ordinary continuous functions of the gradients of velocity, acceleration, ..., nth acceleration at the instant of measurement.

Thus $$\tau_{ij} = F_{ij}\begin{pmatrix} x_{p,q}^{T}(t), v_{p,q}, v_{p,q}^{(1)} \ldots\ldots v_{p,q}^{(n)} \\ t \to -\infty \end{pmatrix}$$

where,

$x^{T}_{p.q_{t\to-\infty}} = \frac{\partial x_p(t)}{\partial x_q}$ that is to say over the range $-\infty \le t \le T,$

$t \to -\infty$

all the terms being ordinary differentials.

Hence, the constitutive equation of an isotropic high polymer, that is to say a Rivlin-Ericksen fluid is,

$$\tau = |\tau_{ij}| = -pI + \Phi_1 d + \Phi_2 b + \Phi_3 d^2 \qquad (9)$$

where, $\tau = \|\tau_{ij}\|,\ I = \|\delta_{ij}\|,\ d = \|\delta_{ij}\|, b = \|b_{ij}\|, d_{ij} = v_{ij} + v_{j,i}$ (10)

$$b_{ij} = a_{ij} + a_{j.i} + 2v_{m,i}v^{m}j,$$

and $a_i = \frac{\partial v_i}{\partial t} + v_{i,j}v^{j}$

and Φ_1 is the coefficient of viscosity,

Φ_2 is the coefficient of visco-elasticity,

Φ_3 is the coefficient of cross viscosity.

These three being in general functions of temperature, material properties and invariants of d, b, d^2.

τ_{ij} is the stress tensor,

d_{ij} is the deformation rate tensor,

b_{ij} is the visco-elastic tensor,

a_i is the acceleration vector,

δ_{ij} is the Kronecker delta and

v_i is the velocity vector.

(iii) The Oldroyd Model

Oldroyd (1953), considering the problem in a general perspective, proposed the consitutive equation:

$$p'_{ik} + \lambda_1 \frac{D}{Dt} p'_{ik} = 2\eta_0 \left(e_{ik} + \lambda_2 \frac{D}{Dt} e_{ik} \right) \qquad (11)$$

where, $\frac{D}{Dt}e_{ik} = \frac{\partial}{\partial t}e_{ik} + v_j\frac{\partial e_{ik}}{\partial x_j} + w_{ij}e_{jk} + w_{jk}e_{ij},$ (12)

$$\frac{D}{Dt}p'_{ik} = \frac{\partial}{\partial t}p'_{ik} + v_j\frac{\partial}{\partial x_j}p'_{ij} + w_{ij}p'_{jk} + w_{jk}p'_{ij}, \tag{13}$$

$p_{ik} = p'_{ik} - p\delta_{ik}$, the stress tensor,

where, δ_{ik} is the Kronecker delta,

$$w_{ik} = \frac{1}{2}\left(v_{k,i} - v_{i,k}\right) \tag{14}$$

$$e_{ik} = \frac{1}{2}\left(v_{k,i} + v_{i,k}\right) \tag{15}$$

and η_0 is coefficient of viscosity.

These give rise to non-linear equations, the simplest generalized form of which is,

$$p'_{ik} + \lambda_1\frac{D}{Dt}p'_{ik} + \mu_0 p'_{ij}e_{jk} - \mu_1\left(p'_{ij}e_{jk} + p'_{jk}e_{ij}\right) - \upsilon_1 p'_{ij}e_{jk}\delta_{ik}$$

$$= 2\eta_0\left\{e_{ik} + \lambda_2\frac{D}{Dr}e_{ik} - 2\mu_2 e_{ij}e_{jk} + v_2 e_{jk}e_{jk}\delta_{ik}\right\} \tag{16}$$

Where, $\mu_0, \mu_1, \mu_2, \upsilon_1$ and υ_2 are scalar physical quantities, having dimensions of time. He emphasized that the above equations with proper choice of constants can explain the behavior of many real fluids including bio-fluids.

References:

1. Oldroyd, J. G. (1950). On the formulation of rheological equation of state. Proc. Roy. Soc. A200, pp.523-541.
2. Green, A. E and Rivlin, R. S. (1957). The Mechanics of non-linear materials with memory. Arch. Rational Mech. Anal. 1. pp.1-34.
3. Noll, W. (1958). The Foundations of Classical mechanics in the light of recent advances in continuous mechanics .Proc. of the Berkeley Symposium on the Axiomatic method.
4. Waltrs, K. (1960). The motion of an elastic-viscous liquid contained between coaxial cylinders. II. Quart. Journal App. Mech. pp. 444-450
5. Weissenberg, K. (1947). A continuum theory of rheological phenomena. Nature, 159 (4035). pp.310-311.

EFFECT OF WOOD DUST ON THE BONDING PROPERTIES OF MAGNESIUM OXYSULFATE: A GREEN CHEMICAL APPROACH

Meenakshi
Department of Chemistry,
University of Rajasthan, Jaipur, Rajasthan, India 302 004
Corresponding author E-mail: meenakshialwaraj@gmail.com

Abstract:

Non-hydraulic Magnesium oxysulfate cement provides numerous advantages over Portland cement, including faster setting, higher fire resistance, lower thermal conductivity, and better abrasion and chemical resistance. It does not require any type of energy, such as heat or light, for its preparation. Magnesium oxysulfate cement draws much research attention because of its energy-saving and environment-friendly properties. Despite its numerous benefits, its commercial application is limited due to its low early strength and poor water resistance. The modern world is fast growing world and the wood industry is a fast growing industry. Many everyday materials are made of wood or wood products. A lot of waste is produced during the cutting and manufacturing of wood materials. A parametric study was conducted to investigate the effect of wood dust on the bonding properties of Magnesium oxysulfate. There are two main objectives of this study: first is to use Magnesium oxysulfate as a pocket-friendly and eco-friendly cementing material in place of other non eco-friendly, costly cementing materials; and second is to use waste material from the wood industry (wood dust) as an additive to enhance the bonding properties of Magnesium oxysulfate.

Keywords: Magnesium oxysulfate, wood dust, setting times, compressive strength, moisture ingress, weathering effects, linear changes, etc.

Introduction:

Chemical binders are compounds that can be used to bind, adhere, or fasten substances directly or indirectly. Their cementing action is caused by polymerization tendencies or interlocking crystal habits. In 1867, a French engineer named Stanislas Sorel invented magnesia cement for the first time. Mainly there are two types of Magnesia cement: first is Magnesium oxychloride and second is Magnesium oxysulfate.

Magnesium oxysulfate is non-hydraulic, air-hardening cement that has a number of advantages over standard Portland cement, including light weight, low thermal conductivity and fire resistance (Newman, 1964; Beaudoin and Ramachandran, 1977; Matkovic *et al.,* 1977; Chandrawat and Yadav, 2000; Bensted and Barnes, 2002). Magnesium oxysulfate cement is used in the commercial manufacture of aesthetic materials, light-weight thermal insulating materials, and fire-resistant materials (Newman, 1964; Gomes and Camarini, 2014; Qin *et al.,* 2018). When compared to Magnesium oxychloride cement, Magnesium oxysulfate cement is less harmful to steel reinforcing and has better weather resistance (Walling and Provis, 2016).

Magnesium oxysulfate cement has attracted much research interest due to its energy-saving and environmental benefits. The manufacturing of lightly burnt Magnesium oxide used in Magnesia cement necessitates a much lower calcination temperature than Portland cement, resulting in a significant reduction in energy usage (Li *et al.*, 2010; Schollbach and Pollmann, 2011).

Magnesium oxysulfate cements are formed by the exothermic reaction between lightly calcined Magnesium oxide and Magnesium sulfate solution. Therefore, dolomite is used as an inert filler to reduce thermal shocks in the cement.

$$MgO + MgSO_4.7H_2O \longrightarrow MOS + Heat$$

(Deformation and expansion)

$$MOS + Heat \xrightarrow{\text{Inert filler}} MOS + \text{Inert filler*}$$

(Intact structure)

(MOS = Magnesium oxysulfate cement)

According to temperature ranges and preparation conditions following types of Magnesium oxysulfates are known. They are $5Mg(OH)_2.MgSO_4.3H_2O$, $3Mg(OH)_2.MgSO_4.8H_2O$, $5Mg(OH)_2.MgSO_4.8H_2O$, $Mg(OH)_2.MgSO_4.5H_2O$, $Mg(OH)_2.MgSO_4.3H_2O$. In all the compositions $5Mg(OH)_2.MgSO_4.8H_2O$ [5.1.8] and $3Mg(OH)_2.MgSO_4.8H_2O$ [3.1.8]compositions of oxysulfate of Magnesium are commonly found. Formation process of [3.1.8] and [5.1.8] composition are as follows:-

$$MgO+H_2O \longrightarrow Mg(OH)_2$$

$$3Mg(OH)_2+MgSO_4.7H_2O \xrightarrow{H_2O} 3Mg(OH)_2.MgSO_4.8H_2O$$

(3.1.8 form)

$$5Mg(OH)_2+MgSO_4.7H_2O \xrightarrow{H_2O} 5Mg(OH)_2.MgSO_4.8H_2O$$

(5.1.8 form)

Magnesia cement offers a number of useful engineering and mechanical features, but its commercial use is limited due to its low water resistance, which results in a considerable reduction in the hardened paste's strength in water (Chuanmei and Dehua, 1995; Chau *et al.,* 2009; Chandrawat *et al.,* 2011; Sglavo *et al.,* 2011). Poor water resistance is a drawback of Magnesium oxysulfate cement, which results in significant moisture absorption and structural deformability. One of the most effective strategies for improving the performance of cementing materials is to include additives.

Wood dust is finely pulverized wood that has consistency fairly equal to sand or sawdust. All high quality wood dust is made from hardwoods because of its durability and strength. Very low grade wood dust is occasionally made from sapless soft woods such as pine or fir. Its main components are cellulose, hemicelluloses and lignin. In the present research work wood dust of *Tectona grandis* is used as an additive. A comprehensive investigation was conducted to study the effect of wood dust on the bonding characteristics of Magnesium oxysulfate cement.

Materials and Method:

The raw materials used in the study were lightly calcined Magnesia, technical grade Magnesium sulfate heptahydrate, dolomite powder, and wood dust. Commercial grade Magnesia was used with the chemical composition shown in Table 1. The Magnesium sulfate ($MgSO_4.7H_2O$) used was an Indian Standard (IS: 2730-1977) technical grade with the following characteristics: colourless, crystalline, hygroscopic crystals; highly soluble in water. Its chemical composition is listed in Table 2. Waste material from dolomite mines (dolomite dust produced during cutting and shaping, etc.) was used as inert filler. The chemical composition of dolomite is shown in Table 3. Wood dust (waste) from wood industry was used in small amounts as an additive in the reaction mixture.

Table 1: Chemical composition of Magnesium oxide (in mass percentage)

MgO	SiO_2	CaO	Fe_2O_3	Al_2O_3	Loss on Ignition
82.68%,	8.38%,	2.97%	0.15%	0.94%,	4.25%.

Table 2: Chemical composition of Magnesium sulfate (in mass percentage)

MgO	CaO	Al_2O_3	Fe_2O_3	Acid insoluble	moisture
96.79%,	1.43%,	0.08%,	0.03%,	0.14%,	0.97%

Table 3: Chemical analysis of Dolomite (in mass percentage)

SiO_2	CaO	MgO	Fe_2O_3	Al_2O_3	LOI	$CaCO_3$	$MgCO_3$	Brightness	Whiteness
5.07%	29.41%	19.45%	0.84%	0.24%	44.51%	52.49%	40.97%	94.00%	94.32%

Pre experimental planning

1. Dry-mix preparation: Dry-mixes were made by mixing equal amounts of lightly calcined Magnesium oxide and dolomite (in 1:1 weight ratio) with varying amounts of wood dust (0%, 5%, 10%, 15% & 20%).
2. Gauging solution preparation: To prepare gauging solution, technical grade Magnesium sulfate was dissolved in lukewarm water to make a saturated solution. Insoluble impurities settled down at the bottom of the container when this solution was let stand overnight. The supernatant saturated solution is filtered with help of vacuum pump. This solution is known as gauging solution for oxysulfate cement. With the use of a Baume hydrometer, the concentration of the gauging solution is determined in degrees on the Baume scale. The higher the degree on Baume scale, the higher will be density and concentration of the gauging solution.
3. Wet-mix preparation: Gauging solution was added to the dry-mix (with different percentages of wood dust) to make a workable wet-mix of standard consistency.

Experiments

All of the experiments were carried out on the best Magnesium oxysulfate cement composition (MgO: Dolomite is in a 1:1 proportion, and the density of the gauging solution is 25^0Be) under the same temperature (30^0C) and humidity conditions (above 90 percent). The effects of wood dust on Magnesium oxysulfate cement were investigated in the following experiments.

- **Setting (Hardening) time investigation:** The effect of wood dust on setting characteristics of Magnesium oxysulfate cement was studied by admixing wood dust in the dry-mix in varying proportion. The amount of wood dust was calculated by weight of

Magnesia. Wet-mixes were prepared by gauging 1:1 dry mixes (by weight of Magnesia and Dolomite) having different quantities of additive (5%, 10%, 15% & 20%) with Magnesium sulfate solution of 25° Be. Standard procedures were adopted according to Indian Standard specification to determine standard consistency, Initial and final setting times using Vicat needle apparatus. Results are summarized in Table 4.

- **Weathering effect investigation:** Standard blocks prepared for setting time investigation were used to determine the effect of weather. Variation in weights of blocks was measured with passage of time after 24 hrs, 7days, 30 days and 45 days using chemical balance. Experimental findings are recorded in Table 5.
- **Moisture ingress investigation:** The effect of wood dust on soundness of the product was studied by performing steam test. For this all setting time blocks with different amounts of wood dust were first cured for sixty days under identical condition and then were exposed to boiling water for at least 30 hours in a closed steam bath. Their relative moisture efficacies were studied as a function of time. Moisture ingress and soundness are inversely proportional. Results are shown in Table 6.
- **Compressive strength investigation:** To study the effect of wood dust on compressive strength of Magnesium oxysulfate standard 50cm^2 cubes were prepared from the standard consistency pastes having wood dust in different amounts. These cubes were tested after thirty days of curing under identical conditions with the help of compressive strength testing machine as per standard procedure. Results are recorded in Table 7.
- **Linear Change investigation:** Standard size blocks (200mmX25mmX25mm) were prepared by wet-mixes having varying quantities of additive in order to study the effect of wood dust on linear changes of Magnesium oxysulfate. Trial beams were measured after 24 hours using micrometer scale (Vernier callipers). After thirty days of curing, under identical conditions, final lengths of the beams were determined. The difference of the two readings shows the linear change (expansion/contraction). If the difference is less, more will be the soundness of the product. Results are summarized in Table 8.

Results:

Results of wood dust on bonding properties of Magnesium oxysulfate cement are summarizes in Table 4-8.

Table 4: Effect of wood dust on setting time investigation of Magnesium oxysulfate cement

Sr. No.	% of wood dust in Dry-mix composition	Setting Time	
		Initial (min)	Final (min)
1.	0%	72	212
2.	5%	65	265
3.	10%	62	259
4.	15%	60	255
5.	20%	58	253

Table 5: Effect of wood dust on weathering effect investigation of Magnesium oxysulfate cement

Sr. No.	% of wood dust in Dry-mix composition	Weight of Blocks in gm After			
		24 hrs	7 days	30 days	45 days
1.	0%	258.07	254.41	252.89	252.09
2.	5%	258.59	252.55	249.26	248.66
3.	10%	244.39	239.21	233.62	233.15
4.	15%	241.57	234.82	228.89	228.46
5.	20%	231.51	224.02	216.96	216.77

Table 6: Effect of wood dust on Moisture Ingress investigation of Magnesium oxysulfate cement

Sr. No	% of wood dust in Dry-mix composition	Trial Blocks Kept In Boiling Water For					
		0-5 hrs	5-10 hrs	10-15 hrs	15-20 hrs	20-25 hrs	25-30 hrs
1.	0%	N.E.	N.E.	N.E.	N.E.	N.E.	N.E.
2.	5%	N.E.	N.E.	N.E.	N.E.	N.E.	N.E.
3.	10%	N.E.	N.E.	N.E.	N.E.	N.E.	N.E.
4.	15%	N.E.	N.E.	N.E.	N.E.	N.E.	N.E.
5.	20%	N.E.	N.E.	N.E.	N.E.	N.E.	N.E.

N.E.: No Effect

Table 7: Effect of wood dust on compressive strength of Magnesium oxysulfate cement

Sr. No	% of wood dust in Dry-mix composition	Compressive Strength (kg/cm^2)
1.	0%	262.430
2.	5%	310.412
3.	10%	306.571
4.	15%	298.513
5.	20%	272.531

Table 8: Effect of wood dust on linear change investigation of Magnesium oxysulfate cement

Sr. No.	% of wood dust in Dry-mix composition	Length of Beams (mm)		Change in Length (mm)
		Initial	Final	
1.	0%	200.00	199.980	0.020
2.	5%	200.00	199.936	0.064
3.	10%	200.00	199.904	0.096
4.	15%	200.00	199.874	0.126
5.	20%	200.00	199.844	0.156

Discussion:

Table 4 incorporates the setting time data of various compositions of Magnesium oxysulfate cement. Addition of wood dust in the matrix results in decrease in initial setting time due to the absorbing nature of the additive therefore hydrolysis takes place immediately during initial setting which accelerates the setting process.

Final setting time increases first with the initial addition of the additive (5%). This increase in final setting period may be due to the reduced concentration of MgO (main component of Magnesia cement) (eq. iii and iv). As the concentration of the additive increases (10% to 20%) chances of formation of interlinking crystals between Magnesia and Wood flour also increases hence final setting time decreases (eq. v).

Data regarding weathering effect investigations of Magnesium oxysulfate cement by incorporating Wood dust in the matrix are recorded in Table 5. Free moisture present in the matrix evaporates gradually causing decrease in weights.

Table 6 represents the water resistance results. Formation of interlinking crystals improves water tightness of the product and makes the product sound. Due to the absorbing nature of the additive absorption and desorption takes place which do not affect the soundness of the product.

Table 7 enumerates the results of compressive strength tests. Compressive strength of the product is increased initially by the addition of the additive (5%). Interlinking crystals are formed between OH group of the additive and Magnesium oxysulfate cement which provide strength to the compound (eq. v). Later on increasing the quantities of the additive (10% to 20%), the chances of formation of strength giving composition (5.1.8) reduced as with increasing amounts of the additive concentration of MgO decreases, hence compressive strength decreases.

Results of linear change investigations are recorded in Table 8. Due to absorbing nature of the additive the product swells and hence volume changes (after drying the product) are expected beyond the experimental limits.

The following probable chemical changes can explain the above discussion.

$CaO+H_2O \longrightarrow Ca(OH)_2$ ....(i)

$MgO + H_2O \longrightarrow Mg(OH)_2$ ....(ii)

$3Mg(OH)_2 + MgSO_4 + 8H_2O \longrightarrow 3Mg(OH)_2.MgSO_4.8H_2O$ ....(iii)

(3.1.8 form)

Magnesium oxysulfate cement

$5Mg(OH)_2 + MgSO_4 + 8H_2O \longrightarrow 5Mg(OH)_2MgSO_4.8H_2O$ ....(iv)

(5.1.8 form)

Magnesium oxysulfate cement

(Strength giving composition)

MOS + Wood Flour $\longrightarrow$ OH groups of Wood dust
|
MOS ....(v)
|
OH groups of Wood dust

Cross interlacing between Magnesium oxysulfate and wood dust

Conclusions:

- A decreasing trend in the initial setting period and increased final setting periods are observed after admixing wood dust in Magnesium oxysulfate cement.
- Resistance to moisture ingress is increased by wood dust.
- The mechanical strength of Magnesium oxysulfate cement is improved by wood dust.
- Contraction in the length of the beams was also observed due to the absorbing nature of the product.

References:

1. Sorel S. (1867). "Sur un nouveau ciment magnésien". *Comptes Rendus Hebdomadaires des Séances de l'Académie des Sciences*, volume 65, pages 102–104.
2. Demediuk, T., Cole, W.F. (1957). A study on magnesium oxysulfates. *Australian Journal of Chemistry,* 10 (3), 287-294.
3. Ball MC (1977) Reactions of compounds occurring in Sorel's cement. *Cement and Concrete Research* 7(5): 575–584.
4. Beaudoin, J. J., Ramachandran, V.S. (1975). Strength development in magnesium oxychloride and other cements. *Cement and Concrete Research* 5(6), 617–630.
5. Beaudoin, J. J., Ramachandran, V. S., Feldman, R.F. (1977). Impregnation of magnesium oxychloride cement with sulfur. *American Ceramic Society Bulletin* 56(4),424–427.
6. Guo, Z., Ding, Q., Liu, L., Zhang, X., Luo, X., Duan, F. (2021). Microstructural characteristics of refractory magnesia produced from macrocrystalline magnesite in china. *Ceramics International*, 47 (16), 22701-22708.
7. Wang, N., Yu, H., Bi, W., Tan, Y., Zhang, N., Wu, C. (2018). Effects of sodium citrate and citric acid on the properties of Magnesium oxysulfate cement. *Construction and Building Materials,* 169, 697-704.
8. Cui, K. X., Jiang,G.C., Yang, L. L., Deng, Z. Q., Zhou, L. (2021). Preparation and properties of Magnesium oxysulfate cement and its application as lost circulation materials. *Petrolium Science,* 18 (5), 1492-1506.
9. Wang, N., Yu, H., Bi, W., Gong, W., Zhang , N., Ma, H., Wu, C. (2022). Hydration and improved properties of Magnesium oxysulfate cement modified by phosphoric acid. *Advances in Cement Research,* 34(1), 36-44.
10. Liu, T., Chunqing, L., Wenqiang, L.L., Dong, Y., Liang, H., Yang, H. (2022). Effect of fly ash and metakaolin on properties and microstructure of Magnesium oxysulfate cement. *Materials. 15(4),* 1334.

11. Qin, L., Gao, X., Chen, T. (2018). Recycling of raw rice husk to manufacture Magnesium oxysulfate cement based lightweight building materials. *Journal of Cleaner Production,* 191, 220-232.
12. Wu, C., Yu, H., Zhang, H., Dong, J., Wen, J., Tan, Y. (2015). Effects of phosphoric acid and phosphates on Magnesium oxysulfate cement. *Materials and Structures,* 48 (4), 907-917.
13. Du, H., Li,J. , Ni, W., Hou, C., Liu, W. (2022). The hydration mechanism of Magnesium oxysulfate cement prepared by magnesium desulfurization byproducts. *Journal of Materials Research and Technology,* Volume 17, 1211-1220 .
14. Cui, K.X., Jiang, G.C. , Yang, L.L., Deng, Z.Q., Zhou, L. (2021). Preparation and properties of Magnesium oxysulfate cement and its application as lost circulation materials. *Petroleum Science*, 18 (5), 1492-1506.
15. Wang, L., Zeng, X., Yang, H., Lu, x., Guo, F., Shi, Y. (2021) Investigation and application of fractal theory in cement-based materials: a review,. *fractal and fractional,* 5 (4), 247.
16. Tan, Y., Yu, H., Sun, S., Wu, C., Ding, H. (2021). Properties and microstructure of basic magnesium sulfate cement: influence of silica fume. *Construction & Building Material,* 266, 121076.
17. Huang, J., Li, W., Huang, D., Wang, L., Chen, E., Wu,C. (2021). Fractal analysis on pore structure and hydration of Magnesium oxysulfate cements by first principle, thermodynamic and microstructure-based methods. *Fractal and Fractional*, 5 (4) 164.
18. Wang, L., Li, G., Li, X., Guo, F., Tang, S., Lu, X. (2021). Influence of reactivity and dosage of MgO expansive agent on shrinkage and crack resistance of face slab concrete. *Cement and Concrete Composites*, 126, 104333.
19. Guan, Y., Hu, Z. , Zhang, Z., Chang, J., Bi, W., Cheeseman, R. (2021). Effect of hydromagnesite addition on the properties and water resistance of Magnesium oxysulfate (MOS) cement. *Cement and Concrete Research*, 143, 106387.
20. Zhang, N., Yu, H., Ma, H., Ba, M. (2021). Effects of different pH chemical additives on the hydration and hardening rules of basic magnesium sulfate cement. *Construction and Building Materials ,* 305, 124696.
21. Tang,S., Wei, C., Cai, R., Huang, J., Chen, E., Yuan, J. (2020). In situ monitoring of pore structure of Magnesium oxysulfate cement paste: effect of $MgSO_4/H_2O$ ratio. *Journal of Industrial and Engineering Chemistry*, 83, 387-400.

22. Cui, K., Jiang, G., Quan, X., Wang, Z., Hua, Z. (2020). Study of effects of downhole conditions on the setting time and compressive strength of MOS settable system by orthogonal experimental design. *The 6th International Conference on Water Resource and Environment, IOP Publishing, Toyko, Japan*, 23-26.
23. Guo, T., Wang, H., Yang, H., Cai, X., Ma, Q., Yang, S. (2017). The mechanical properties of Magnesium oxysulfate cement enhanced with 517 phase Magnesium oxysulfate whiskers. *Construction and Building Materials*, 150, 844-850.
24. Wu, C., Chen, W., Zhang, H., Yu, H., Zhang,W., Jiang, N. (2017). The hydration mechanism and performance of Modified Magnesium oxysulfate cement by tartaric acid. *Construction and Building Materials,* 144, 516-524.
25. Hongping, H., Hongfa, Y., Na, Z., Haiwei, Z., Shun, L., He, F. (2016). Ingredients regularity and fundamental characteristics of basic magnesium sulfate cement. *Bulletin of the Chinese Ceramic Society*, 35 (8) 2561-2567.
26. Dang, L., Nai, X.,Zhu, Z., Jing, Y., Liu, X., Dong, Y. (2014). Study on the mechanism of surface modification of Magnesium oxysulfate whisker. *Applied Surface Science*, 317, 325-331.
27. Wen, J., Yu, H., Li, Y., Wu, C., Dong, J. (2014). Effects of citric acid on hydration process and mechanical properties of thermal decomposed magnesium oxychloride cement. *Journal of Wuhan University of Technology -Materials Science Ed,* 29 (1) pp. 114-118.
28. Rünčevski, T., Wu, C., Yu, H., Yang, B., Dinnebier, R.E. (2013). Structural characterization of a new Magnesium oxysulfate hydrate cement phase and its surface reactions with atmospheric carbon dioxide. *Journal of American Ceramic Society,* 96 (11), 3609-3616.
29. Dinnebier,R.E., Pannach, M., Freyer, D. (2013). $3Mg(OH)_2 \cdot MgSO_4 \cdot 8H_2O$: a metastable phase in the system Mg(OH)2-MgSO4-H2O. *Zeitschrift für anorganische und allgemeine Chemie* , 639 (10) (2013), pp. 1827-1833.
30. Li, J., Xiang, L., Jin, Y. (2006). Hydrothermal formation of Magnesium oxysulfate whiskers in the presence of ethylenediaminetetraacetic acid. *Journal of Materials Science,* 41 (5) 1345-1348.
31. Yue, T.,Gao, S., Lixia, Z., Shuping, X., Kaibei, Y. (2002). Crystal growth and crystal structure of Magnesium oxysulfate $2MgSO_4 \cdot Mg(OH)_2 \cdot 2H_2O$. *Journal of Molecular Structure,* 616 (1–3) 247-252.

32. IS 6932-1 (1973): Method of test for building limes, Part 1: Determination of insoluble residue, loss on ignition, insoluble matter, silicone dioxide, ferric and Aluminium oxide, Calcium oxide and Magnesium oxide [CED 4: Building Limes and Gypsum Products].
33. IS 2730 (1977): Magnesium sulphate (epsom salt) [CHD 1: Inorganic Chemicals].
34. IS 1760-3 (1992): Methods of chemical analysis of limestone, dolomite and allied materials, Part 3: Determination of Iron oxide, Alumina, Calcium oxide and Magnesia [MTD 13: Ores and Raw Materials]
35. IS 658 (1982): Code of practice for Magnesium oxychloride composition floors [CED 5: Flooring, Wall Finishing and Roofing]
36. IS 5513 (1996): Specification for vicat apparatus [CED 2: Cement and Concrete]

FERROSPINELS: A BRIEF REVIEW ON PHYSICO-CHEMICAL CHARACTERISTICS

Umesh Sankpal
Department of Chemistry,
Gogate - Jogalekar College, Ratnagiri, 415 612, Maharashtra, India
Corresponding author E-mail: umesh.sankpal@resgjcrtn.com

Introduction:

Recently, mixed-metal oxides have gained an important role in the development in various fields. Their physical properties such as magnetic permeability, high electrical resistivity make them useful for application in magnetic and electric devices [1-5]. Apart from their technological importance as magnetic materials, ferrites have also well-established catalytic properties as well as gas sensing properties [6-7]. All these properties mainly depend upon their chemical composition and microstructure of the materials. Generally, mixed-metal oxides are prepared by high temperature solid state reaction. On the other hand, like for gas sensing and catalytic activity, lower density and high surface area materials are preferred. In recent years' different methods have been developed in this area [8]. Study of these materials helps to correlate the chemical and physical properties of solids and thus in solving a variety of problems of practical and technological importance. It also offers to synthesize nanomaterials having improved characteristics.

Oxidicspinels with general formula AB_2O_4 have been studied by many researchers. This class of materials indicates aluminates, ferrites, chromites, manganetites, gallets, garnets, galloferrites etc. These types of materials have interesting structural, electrical and magnetic properties. These properties are mainly depending upon the cations, methods of preparation and sintering temperature. Their substitution over tetrahedral and octahedral sites is also remarkable.

The present trend in material science is the studies on materials in the nanometer size. The main emphasis is on the synthesis, characterization, study of the differences in the properties with respect to the corresponding bulk counter parts and on the application of nanomaterials for the benefit of human kind [9-11]. It is referred that 'small is beautiful' due the beautiful color, shape and properties of nanosized materials [12-13]. Nanoscience has become the focus of modern material science because of the potential technological importance, which stems from the unique physical properties of nanomaterials [10, 14 and 15]. Fundamentally, the nanoscience and nanotechnology is also a part of materials science. The nanosized materials are distinguished from bulk polycrystalline materials by the size of the crystallite that composes it. When the dimension of a particle is reached below 100 nm, it is called a nanoparticle. A nanocrystalline material might be a ceramic, metallic, oxide, semiconducting material or an alloy. In the case of magnetic materials, the nanoparticles show highest coercivity and superparamagnetic behavior below a particular critical particle size. Nanoparticles have higher surface to volume ratio, hardness and strength as compared to that of the bulk. The interesting and sometimes unexpected properties of nanoparticles are partly due to the dominating the properties of the surface in lieu of the bulk properties. The percentage of atoms at the surface of a material becomes significant as the size of the material approaches the nanoscale. The nanomaterials can be shaped as nanospheres, nanorods, nanocups, nanowires, nanotubes, nanoribbons, nanoplates, nanocubes and many more by specialized synthesis procedures. Depending on the enhanced properties of the nanomaterials compared to the bulk, several high quality applications have been predicted [16-20]. Some of the established, applied and some predicted applications of nanoparticles are: information storage [21], refrigeration [22-23], sensors [16,24-25], targeted drug delivery [26-27], catalysis [28], nanophotonicsand optoelectronics [29-30], etc. Nanoparticles of magnetic metals are also finding applications as catalysts, nucleators for the growth of high-aspect-ratio nanomaterials and toxic waste remediation. The magnetic nanopartciles are of great technological importance because of their use in magnetic fluids, information storage devices and medical diagnosis [31]. The area of research regarding magnetic nanoparticles continues to be a fascinating system both from fundamental as well as research point of view [32]. It is well known that the properties of the materials change drastically below a critical size [33] and study of size of the material is essential for creative use of nanoparticles in many devices.

Spinel:

The term spinel is named after the natural mineral, $MgAl_2O_4$. It has a general chemical formula of $A^{II}B_2^{III}O_4$, where A is a divalent cation (M^{2+}) and B is a trivalent cation (M^{3+}) [34]. There are three categories of spinel phases are normal, inverse and random spinels. In spinel structure A_xB_{1-x} [A_{1-x} B_{1+x}] O4, when x = 1, then all divalent ions occupy the tetrahedral or the A-sites and the spinel is called as normal spinel. The examples of normal spinel are $ZnFe_2O_4$ and $CdFe_2O_4$, in which the Zn^{2+} and Cd^{2+} ions are situated on the A-sites and all the Fe^{3+} are situated in the B-sites. When x = 0, the spinel is called as inverse spinel, *e.g.*$CoFe_2O_4$ and $NiFe_2O_4$. In this case the divalent Co and Ni are present on the octahedral sites. However, the value of x can lie between 0 and 1 also. In this case the spinel is called as random spinel, such as $CuFe_2O_4$, $MgFeCrO_4$ and $MgFe_2O_4$. In random spinel ferrite, all divalent ions and trivalent Fe^{3+} ions are randomly distributed over tetrahedral (A) sites and octahedral [B] sites. The cation distribution is sensitive to the method of synthesis and heat treatments. The magnetic, structural and optical properties of spinel ferrites are mainly dependent on the cation distribution and the microstructure of the final sintered products. Groenou*et al.* have reviewed the effect of microstructure control with emphasis on the sintering process of spinel ferrites [35]. The lattice characteristics of a spinel include a FCC site for the oxygen atoms and two cationic sites occupying the tetrahedral and octahedral interstices [36].

The general structure formula of the spinel can be written as

$$A_{(x)}B_{(1-x)}[A_{(1-x)}B_{(1+x)}]O_4$$

where (x) varies from 0.0 to 1.0 and the square bracket indicates the B-site cations. Normal, inverse and random spinelshave been discussed earlier. Spinelsare also classified on the basis of the valency of cations present in the lattice such as 2-3, 2-4 spinel etc. In some cases, the divalent ion may be replaced by monovalent + trivalent ions, while still retaining the spinel structure, e.g. $Li^{+}_{0.5}Fe^{3+}_{2.5}O_4$, $Li^{+}_{0.5}Mn^{3+}_{2.5}O_4$ and $Ni^{2+}Fe^{3+}_{1.5}Zn^{2+}_{0.25}Ti^{4+}_{0.25}O_4$. The represented compounds show the general AB_2O_4 structure. The cation distribution over the two different sites is dependent on the method of synthesis and is variable with temperature. By changing the existing cation distribution one can change the interesting magnetic (e.g. change in Curie temperature) and electrical (e.g. change in resistivity) properties of spinel ferrites and can be used for some new applications. There are several factors which determine the cation distribution. These are i) ionic radius, ii) electronic configuration, iii) electrostatic energy (Madelung energy), iv) elastic energy, v) polarization effect, vi) covalent bonding effect and the most important vii) crystal field stabilization energy.

The unit cell of spinel contains 8 formula units or each octant contain 1formula unit and may thus be written as $M_8Fe_{16}O_{32}$. The oxygen anions form an ideal face-centered cubic (fcc) lattice (Fig. 1). Within this lattice two types of interstitial positions occur viz. tetrahedral and octahedral, which are depicted pictorially in Fig. 2. There are 64 tetrahedral sites and 32 octahedral sites available, and, out of these 8 tetrahedral and 16 octahedral sites are occupied by cations. Each cation in the tetrahedral position has 4 neighboring oxygen ions and is often called an *A* site, while each cation in the octahedral position has 6 neighboring oxygen ions and is called a *B* site, in the general formula AB_2O_4. The oxygen (O) ions have a four-fold coordination, formed by three *B* cations and one *A*cation. The spinel ferrite space group is

Oh_7(Fd_3m) [37-38] and the space group number is 227. The oxygen ions in the ferrite structure are not generally located at the exact position of theFCCsublattice. Their detailed positions are determined by a parameter, *u*, called the oxygen parameter. *u*reflects the adjustments of the structure to accommodate difference in the radius ratio of the cations in the tetrahedral and octahedral sites [39-40]. Packing of the ions within the lattice is perfect when u = 3/8.

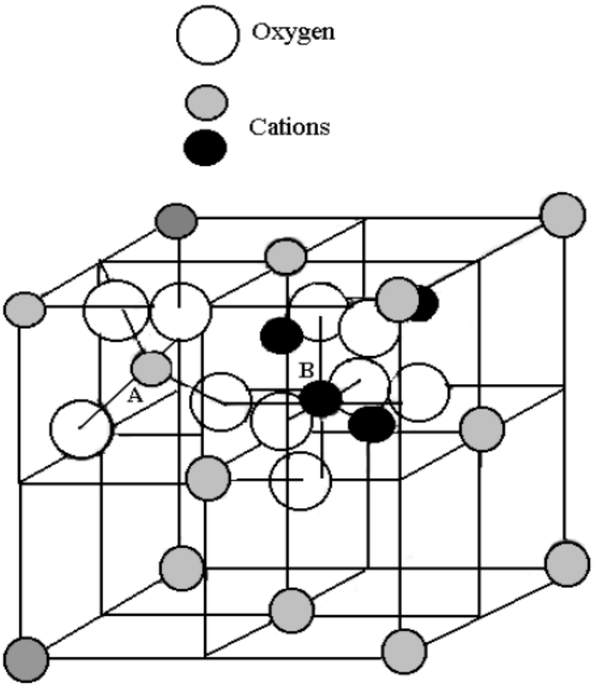

Figure 1: The Spinel structure

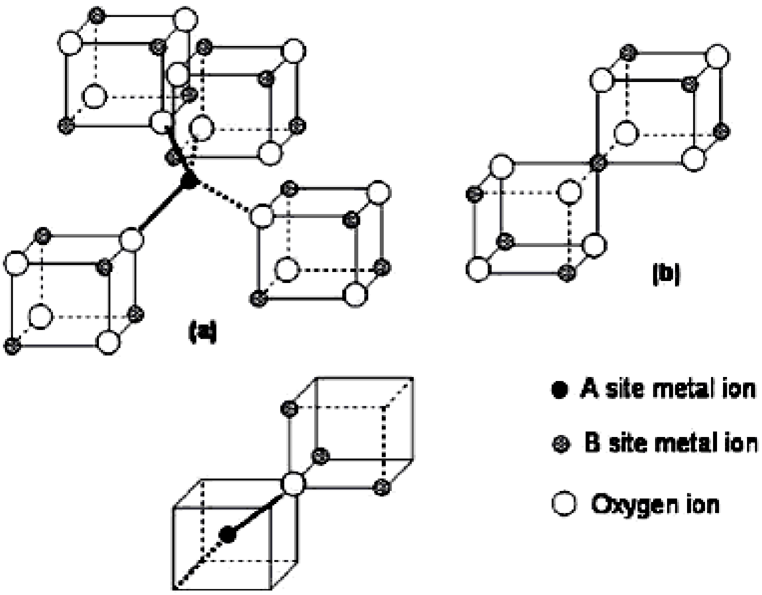

Figure 2: Corner sharing of *A* and *B*-site metal ions and oxygenions

Electrical properties:

Ferrites have vast applications from microwave to radio frequencies. They exhibit relatively high resistivity at carrier frequency, sufficiently low losses for microwave applications and wide range of other electric and dielectric properties. The electrical properties of ferrites are influenced by distribution of cations in the sites, type and amount of dopant, amount of Fe^{2+} present, sintering conditions, grain size etc. Due to the high electrical resistivity (low conductivity) of ferrites, they are used in microwave applications. The order of magnitude of conductivity greatly influences the dielectric and magnetic behaviour of ferrites. This has aroused considerable interest in the electrical conductivity, frequency and temperature dependence of dielectric behavior of ferrite. Mostly, spinel ferrites are found to have resistivity of the order of 10^6 ohm.cm. like semiconductors. The conductivity is due to the presence of Fe^{3+} and Me^{2+} (Me = Ni, Co, Mg, Mn, etc.) ions. The presence of Fe^{3+} results in 'n' type behavior and of Me^{2+} in 'p' type behavior. The conductivity arises due to the mobility of the extra electron from Fe^{3+} or the positive hole (Me^{2+}) through the crystal lattice. The movement is described by the hopping mechanism, in which the charge carriers jump from one ionic site to the next. According to Verweyet. al. [41], the conductivity of high resistivity oxides can be increased by the addition of small amount of impurities to the structure. The substitution of cations of the low valence state gives rise to 'p' type of conduction while the substitution of cations of high valence state to 'n' type of conduction [42]. The presence of Fe^{2+} ions is sometimes desirable [43] as it reduces magnetostriction effect and resistivity. Most of the spinel ferrites are semiconductors and their resistivity decreases with increase in temperature according to the Arrhenius relation. The activation energy (ΔE) is the energy needed to release the electron from the ion from a jump to the neighboring ion. The conduction mechanism can be explained on the basis of hopping mechanism as given below.

$$Me^{2+} + Fe^{3+} \leftrightarrow Me^{3+} + Fe^{2+} + \Delta E$$

where, Me represents divalent metal ions like Cu, Mg, Co, Ni, etc. and ΔE is activation energy required to transfer the electrons from Me^{2+} to Me^{3+} and vice versa. The conduction in ferrite can also be explained on the basis of hopping of polaron. The combination of electron and polarization field is called as polaron [44-45].

Dielectric studies:

Dielectric properties of ferrites depend upon the several factors including the method of preparation, chemical composition, grain structure and grain size of the particle. When the ferrospinelsare sintered under slightly reducing condition, the valence stage changes the individual cation formation in the sample leading to high conductivity and when such material is cooled in oxygen atmosphere, it is possible to form films of high resistivity over the constituent grains. Such a ferrite in which the individual grains are separated by either air gaps or low conductivity layer behaves as inhomogeneous dielectric material. This has arised considerable interest in low frequency (in the range of 10^2 Hz to 10^5 Hz) dielectric behavior of ferrites. Among many workers involved in this type of studies the prominent one are Koops [46], Moltgen [47], Kmiyoshi [48], Iwauchi [49-50], et. al. Rezlescu [51-52],Brockmon, [53-54], Avramenko [55] andJosyula [56] etc.

Recently, the polarization studies were further extended to understand and interpret the earlier theories in a microscopic manner relevant to different materials. These theories were also extended to interpret the low frequency dielectric properties of ceramic materials that include ferrites. Jonscher [57] interpreted the possible mechanism in this class of material, when the electric field is applied to the dielectric materials; there is tendency for positive and negative charge within the material to displace relative to one another. Hence the system acquires an electric dipole moment. The dipole moment per unit volume is called as polarization (P). The total polarization of dielectric can be represented as,

$$P = Pe + Pi + Po + Ps$$

where, Pe = electric polarization
Pi = Ionic polarization
Po = Orientational polarization
Ps = Interfacial or space change polarization

In electronic polarization, the center of gravity of electron is shifted relative to nucleus in an electric field. In ionic polarization, there is displacement of positive and negative ions relative to one another. In orientation polarization, electric dipoles are oriented by the application of an external field. The space charge also tends to have its own polarization in the case of ferrites.

The polycrystalline ferrospinels have high dielectric constant of the order of a few thousands at low frequencies following to a very low value of only 10 – 20 at microwave frequencies. The a.c. resistivity decreases with increasing temperature like d.c. resistivity, where as dielectric constant increases with increase in temperature. Similar process of conduction mechanism in dielectric polarization is like conduction process [58]. This is given as Koopsphenomological theory of dispersion.

Magnetism in ferrites:

Magnetization in ferrites occurs from the uncompensated antiferromagnetism, so the magnitude of magnetization depends on composition, cation distribution and the relative strength of the possible interactions. Since cation-cation distances are large in ferrites due to their crystal structure, direct exchange interactions are negligible. The major interaction that occurs in ferrites is the superexchange interaction between octahedral and tetrahedral cations or A-O-B interactions [59-60]. The next acceptable interaction is B-O-B superexchange. However, A-O-A interaction is not coming into picture, as it is very weak [40]. The magnetism in the ferrospinels has been explained by Neel et. al. [61] and the strength of exchange interactions control the saturation magnetization and the Curie temperature of the ferrites and this exchange interaction is controlled by cation distribution over tetrahedral and octahedral sites. The magnetic exchange forces between the metal ions in the ferrites are mediated via oxygen ions by an exchange mechanism best known as the superexchangeinteraction. Hence, the interaction between the neighboring atoms is indirect and takes place through non-magnetic ions. It has been established that the interaction energies are negative and hence induces antiparallel orientation, which give lowest energy. An angle of 180° gives rise to the greatest exchange energy and energy decreases very rapidly with increasing distance between the ions (Fig. 3).

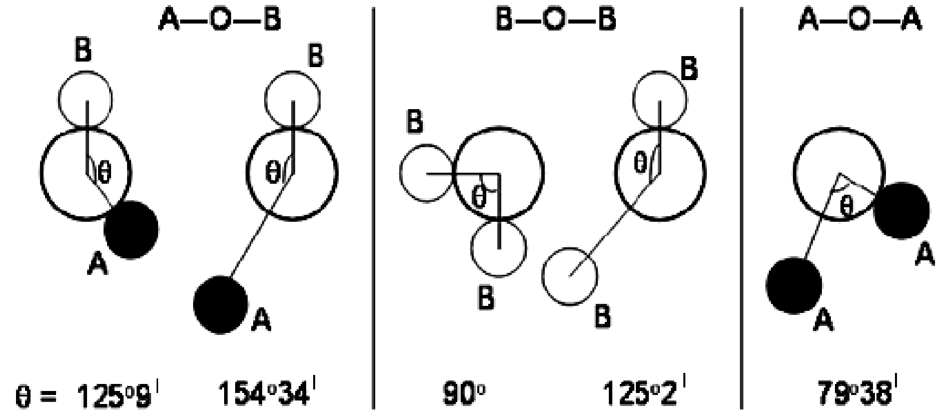

Figure 3: Different types of interactions for different types of lattice sites in ferrite

According to the Neel's theory the value of magnetic moment at B site (M_B) is greater than that of magnetic moment at A site (M_A) so that, the resultant magnetic moment is written as,

$$M_S = |M_B - M_A|$$

On the basis of their coercive field, ferritesare classified as soft and hard ferrites. If the coercive field (Hc) is in the range of 1.5 Oe to 6 Oe, it is termed as hard ferrite while the Hc is in the range 10 Oe to 100 Oe called as soft ferrite.

References:

1. R. Valenzuela, 1994, Magnetic Ceramics, Chemistry of Solid State Materials, Series Ed. B. Dunn, J. W. Goodby, A. R. West,(Cambridge Univ. Press, Cambridge).
2. A. R. West, 1988, Basic Solid State Chemistry, (John Wiley and Sons.Ltd.).
3. B. Viswanathan and V. R. K. Murthy,1990, Ferrite Materials: Science and Technology (Narosa Publishing House, New Delhi).
4. V. S.Bushkova, I. P.Yaremiy, 2018, Journal of Magnetism and Magnetic Materials 461, 1 37-47.
5. V. V.Jadhav, S. D.Shirsat, U. B.Tumberphale, R. S. Mane, 2020, Spinel Ferrite Nanostructures for Energy Storage Devices Micro and Nano technologies, 35-50.
6. C. G. Ramakutty, S. Sugunan, T. Bejoy, 2002, J. Mol. Catal. A : Chem. 187, 105.
7. L. Satyanarayana, K. M. Reddy, S. V. Manorama, 2003, Mater. Chem. Phys. 82, 21.
8. K. Vidyasagar, J. Goplakrishnan, C. N. R. Rao, 1984, Inorg. Chem. 23, 1206.
9. P. M. Ajayan, L. S. Schadler and P. V. Braun, 2003, NanocompositeScience and Technology, (Wiley-VCH GmbH and Co. KGaA, Weinheim).
10. V. Rotello, 2004, Nanoparticles: Building Blocks for Nanotechnology, Nano-structure Science and Technology Series, Springer, New York.
11. G. Cao, 2004, Nanostructures and Nanomaterials: Synthesis, Properties and Applications, (Imperial College Press, London).
12. G. Fasol, 1998, Science 280, 545.
13. A. Thiaville and J. Miltat, 1999, Science 284,1939.
14. H. Gleiter, 1992, Adv. Mater. 4, 474.
15. G. A. Ozin, 1992, Adv. Mater. 4, 612.
16. A. N. Shipway, E. Katz and I. Willner,2000,Chem. Phys. Chem. 1,18.
17. P. Gomez-Romero, 2001, Adv. Mater. 13,163.
18. P. V. Kamat,2002, J. Phys. Chem. B 106, 7729.
19. M. C. Daniel and D. 2004, Chem. Rev. 104, 293.
20. D. Wang and H. Mohwald, 2004J. Mater. Chem. 14, 459.
21. B. D. Terris and T. Thomson,2005,J. Phys. D: Appl. Phys. 38, R199.
22. R. D. McMichael, R. D. Shull, L. J. Swartzendruber, L. H. Bennett and R. E. Watson,1992, J. Magn. Magn. Mater. 111, 29.
23. Y. Z. Shao, J. K. L. Lai and C. H. Shek, 1996, J. Magn. Magn. Mater. 163,103.
24. M. J. Toohey, 2005, Sens. Actuators B: Chem. 105, 232.
25. L. Murphy, 2006, Current Opinion Chem. Bio. 10, 177.

26. A. K. Gupta and A. S. G. Curtis, 2004, J. Mater. Sci.: Mater. Medicinal 15, 493.
27. L. E. van Vlerken and M. M. Amiji, 2006, Expert Opin. Drug Deliv. 3, 205.
28. C. A. Mirkin, R. L. Letsinger, R. C. Mucic and J. J. Storhor, 1996, Nature 382, 607.
29. P. N. Prasad, 2006, Molecular Crys. Liquid Crys. 466, 1.
30. X. Zhang, B. Sun, R. H. Friend, H. Guo, D. Nau and H. Giessen, 2006,NanoLett. 6, 651.
31. R. Arulmurgan, J. Yadevan, 2005, J. Magn. Magn. Mater. 288, 470.
32. I. H. Gul, 2007, J. Magn. Magn. Mater. 311, 494.
33. J. Garcia Oters, M. Porto, J. Rivas, A. Bunde, 2000, Phys. Rev. Lett. 84, 167
34. R. A. McCurrie, 1994, Ferromagnetic Materials - Structure and Properties; (Hartcourt Brace and Company: London).
35. A. B. V. Groenu, P. F. Bongers and A. L. Stuyts, 1968, Mater. Sci. Eng. 3, 317.
36. C. R.Vestal& J. Z. Zhang, 2004, Int. J. of Nanotechnology 1, 240.
37. F. S. Galasso, 1970, Structure and Properties of Inorganic Solids, (Pergamon Press, Oxford,).
38. R. W. G. Wycko, 1968, Crystal Structures: Miscellaneous Inorganic Compounds, Silicates and basic structural information Vol. 4,2nd ed. (Interscience Publishers, New York) 540.
39. J. Smith and H. P. J. Wijn, 1959, Ferrites, Philips Technical Library, Eindhoven.
40. B. D. Cullity, 1988, Introduction to Magnetic Materials, (Addison-Wesley Publishing
    a. Company reading Massachusetts).
41. E. J. W. Verwey, E. L. Hsellmann, 1947, J. Chem. Phys. 15, 174.
42. S. L. Snoek, 1947, "New Development in ferromagnetic material" (Elsevier publishing co. New York, Amsterdam).
43. M. A. Elhiti, M. A. Ahmed, M. M. Mosad, S. M. Attia, 1995, J. Magn. Magn. Mater. 150, 399.
44. M. Singh,2006, J. Magn. Magn. Mater. 299, 397.
45. A.K. Rajarajan, S.M. Yusuf, P. Balaya, R.G. Kulkarni, 2002, Pramana 58, 787.
46. C. G. Koops,1951 Phys Rev. 83, 121.
47. S. Moltgen, F. Zeit, 1952, Angew Phys 4, 216.
48. K. Kashiyoshi, 1951, Sci. Rept. Res. Inst. (Tohoku Uni. Japan, A3) 716.
49. K. Iwauchi, 1971, J. Appl. Phys. 10, 1520.
50. K. Iwauchi, S. Yamamoto, Y. Bando, Japanies, 1971, J. Appl. Phys. 10, 513.
51. N. Rezlescu, E. Rezlescu, 1974, Phys. Stat. Solidi (a) 23, 575.
52. N. Rezlescu, E. Cuclreanau and V. Petrescu, 1970, Rev. Rom. Phys. 15, 965.

53. F. G. Brockman, K. E. J. Motteson, 1970, J. Am. Ceram. Soc. 53, 517.
54. F. G. Brockman, K. E. J. Motteson, 1971, J. Am. Ceram. Soc. 53 180.
55. V. P. Avermenko, O. V. Sinykov, Z. N. Ukr, 1968 , (Ukr. Ed.) 13, 1174.
56. O. S. Josyulu, K. Sabhanadri, 1980, Phys. Stat. Solidi (a), 59, 323.
57. A. K. Jonscher, 1983,“Dielectric Relaxation in Solids,” (Chelsea Dielectric Press, London).
58. M. K. Fayek, S. S. Ata-Alah, H. A. Zayed, M. Kaiser,S.M. Ismail, 2009, J. Alloys Compd. 46, 9.
59. Gurunam Singh, 1991, Ph.D. Thesis, University of Mumbai, Mumbai.
60. A. Goldman, 1990, Modern Ferrite Technology, (Van Nostrand Reinhold, New York,).
61. L. Neel, 1948, Ann. Phys. (Paris) 3, 137.

FUSED THIOPHENE BASED DYE SENSITIZED SOLAR CELL

Yamuna Ezhumalai[1]* and Prabakaran Kumaresan[2]
[1]Centre for Material Chemistry, Karpagam Academy of Higher Education,
Eachanari, Coimbatore-641021, India
[2]Department of Chemistry, PSG College of Arts and Science,
Peelamedu, Coimbatore-641014, India
*Corresponding author E-mail: yamuchemist@gmail.com

Abstract:

A new series of metal-free alkylated tetrathienoacene (TTAR)-based organic chromophores, TPA-TTAR-TA (R = branched-C_8H_{17}, **1**, **TTAR-b8**; R = $C_{15}H_{31}$, **2**, **TTAR-15**; R = C_9H_{19}, **3**, **TTAR-9**), are synthesized for application in dye-sensitized solar cells (DSSCs). Due to the extensively conjugated TTAR π-bridge, all three dyes exhibit high extinction coefficients (1×10^5 M^{-1} cm^{-1}). By systematically exploring the effects of the TTAR alkyl chain substituents, a significant influence of the dye coverage (orientation) on the TiO_2 surfaces is observed. The branched-alkyl **TTAR-b8** (dye **1**) promotes significant tilting and packing distortion on TiO_2 in comparison to more ordered monolayers of linear long alkyls **TTAR-15** (dye **2**) and **TTAR-9** (dye **3**). Photophysical measurements on the dye-grafted TiO_2 films reveal that the branched-alkylated TTA unit in dye **1** enhances the electron injection efficiency, in agreement with the high quantum efficiency. Notably, by utilizing a three-dimentional (3D) photonic crystal (PhC) layer to enahnce the coherent scattering an increase the light absorption**, TTAR-b8** exhibits higher short-circuit current densities and achievs a high PCE of 11.18 %. Thus, **TTAR-b8** is the highest performing fused-thiophene-based organic DSSC dye reported to date.

Introduction:

Dye-sensitized solar cells (DSSCs) have attracted enormous attention in the past couple of decades, due to their ability to efficiently convert solar energy to electricity at a low cost.[1] The improvement in DSSCs performance depends on the properties of the elements used in the device, such as the photosensitizer, counter electrode, photoanode, electrolyte, and their combination. Undoubtedly, the development of more effective sensitizers is one of the most promising ways to obtain further advances in DSSCs.[2-4] Among the various sensitizers, porphyrin sensitizer-based DSSC in combination with cobalt electrolyte and platinum counter show a certified PCE value of 13%.[5-7] However, the tedious synthesis process and low yield of porphyrin may limit the large-scale application of this sensitizer. As a result, metal-free organic dyes have attracted considerable attention for practical applications due to the following characteristics: i) chemical versatility and facile synthesis approaches in terms of molecular tailoring; ii) a tunable spectral property, to enable broad and high levels of solar spectral absorption in the visible region; and iii) low production cost.[8-11] However,the performance of DSSCs using organic dyes remains behind that of those using metal-incorporated sensitizers, because of their lower open-circuit voltage and higher recombination rate.[12-14] Still, a few recent reports have reported impressive efficiencies of 10.65% and 12.5% employing single metal-free organic dyes, thus showing good potential for the future development of DSSCs.[15,16]

Most of the metal-free organic sensitizers employed in DSSCs consist of an electron donor and an acceptor connected by a π -conjugated linker, thus presenting wide possibilities for structural modification.[17-20] In such dye systems, triarylamine and cyanoacrylic acid are widely employed as a donor and acceptor units, respectively, and various π-conjugated linkers are used to bridge the donor and acceptor units to create a diverse of D-π -A dyes for DSSCs.[21-23] It is well known that the π-spacer plays an important role in tuning the molecular band gap, as well as electronic and steric factors strongly affecting device performance. For these reasons we have been interested in implementing the unique planar conjugated tetrathienoacene (TTA) framework in DSSCs since it exhibits excellent hole/electron mobility in organic thin film transistors (OTFTs) due to long range order and favorable reorganization energies.[24,25] Following its successful application in OTFTs and two-photon processing, it was recently investigated as a bridge to construct D-π-A organic DSSC dyes, and achieved a device power conversion efficiency (PCE) of 10.1% with dye **TTAR-15** (Fig. 1).[26] The linear C15-alkyl chain substituent not only prevents dye aggregation but also curtails charge recombination. However, it does not efficiently suppress intermolecular π-π interactions when the molecules assemble on the TiO_2 surface.

Therefore, to enhance/compare/contrast the TTA unit effectiveness as a charge transporting π-linker and to increase the V_{oc} by suppressing close intermolecular π -π interactions, we designed and synthesized a new sensitizer functionalized with a branched alkyl group (b-C_8H_{17}), **TTAR-b8** (**1**). To examine effects on the short-circuit current density (J_{sc}) at higher dye coverage's, the **TTAR-15** C15 linear alkyl chain was also changed to C9. Therefore, the linear alkyl chain ($C_{15}H_{31}$ and C_9H_{19}) substituted dye molecules **TTAR-15** (**2**) and **TTAR-9** (**3**) (Figure 1) were prepared for this detailed comparatively study. The effects of the branched alkyl chains vs. linear chains TTARs on photovoltaic performance and charge recombination dynamics in DSSCs are fully investigated.

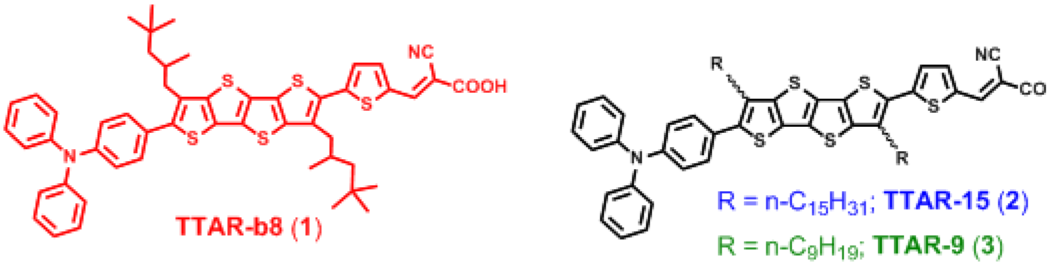

Figure 1: Chemical structures of TTA-based dyes (1-3)

Optical, electrochemical data, and DFT calculations

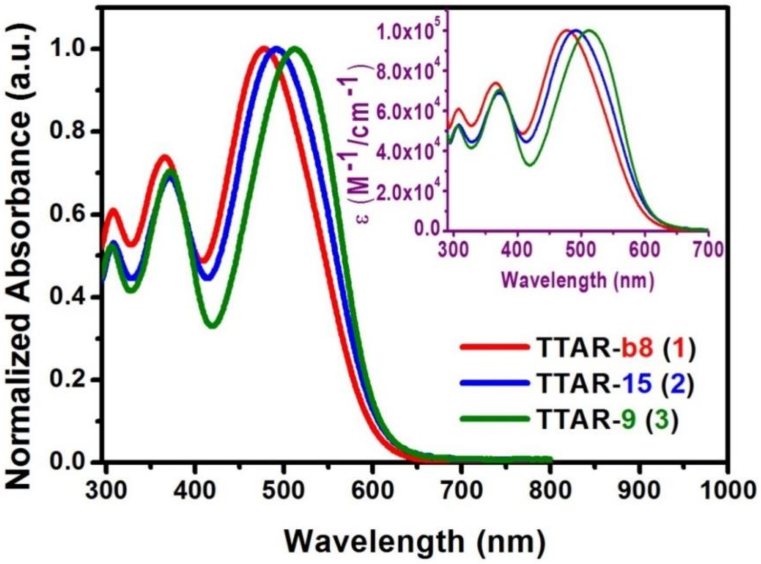

Figure 2: UV-vis absorption spectra of dyes 1-3 and their corresponding molar absorption coefficients measured in o-$C_6H_4Cl_2$ in a concentration of 10-5 M. Copyright (JMCA 2017)

The UV-vis absorption spectra of three sensitizers in *o*-$C_6H_4Cl_2$ solutions (1x 10^{-5} M) are shown in Figure 2.

Table 1: Distribution in HOMO and LUMO levels of TTA dyes

Dye	UV-Vis[a]	E_g (eV)	E_{Ox} [c]	Energy level (eV)		Energy level (eV)	
	λ_{max} (nm)	(UV)[b]	(V)	E_{HOMO}[d]	E_{LUMO}[e]	E_{HOMO}[f]	E_{LUMO}[f]
TTAR-b8	485	1.92	0.99	-5.19	-3.27	-5.02	-2.71
TTAR-15	498	1.91	0.99	-5.19	-3.28	-4.99	-2.71
TTAR-9	519	1.91	1.00	-5.20	-3.29	-4.99	-2.71

[a] in *o*-$C_6H_4Cl_2$ at 25 °C. [b]calculated from optical absorption onset. [c]E_{ox} = oxidative potential, by DPV in *o*-$C_6H_4Cl_2$ at 25 °C, ferrocene/ferrocenium was used as the internal standard and set at +0.6 V (-4.8 eV).[d]$E_{HOMO} = -(4.2+ E_{ox})$. [e]Estimated from $E_{HOMO}+\Delta E_g$.[f]By DFT calculation.

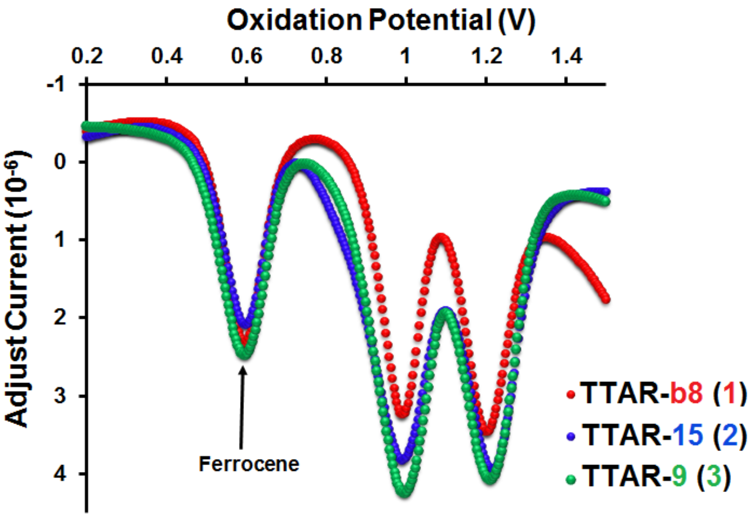

Figure 3: DPV oxidation potential curves of Dye(1– 3) in *o*-$C_6H_4Cl_2$ solution

To investigate substitution effects on TTA molecular energy levels, the electrochemical properties of these dyes were analyzed by differential pulse voltammetry (DPV) in 1,2-dichlorobenzene solutions with 0.1 M tetrabutylammonium hexafluorophosphate ($TBAPF_6$) as the electrolyte, and a three-electrode configuration consisting of a Pt disk working electrode, an auxiliary Pt wire electrode, and a nonaqueous Ag reference electrode. All potentials reported are referenced to a Fc^+/Fc internal standard (at +0.6 V). The DPVs of the oxidation peaks of **1-3** are exhibited at 0.99, 0.99 and 1.00 (V), respectively, as shown in **Table 1**

All the dyes adsorbed on the TiO_2 thin film exhibit red-shifted absorption profiles (Figure5) in comparison to that measured in the solution. The red shifted absorption may be attributed to the intermolecular interactions on the TiO_2 surface, which are likely to occur due to the presence of a TiO_2 layer.

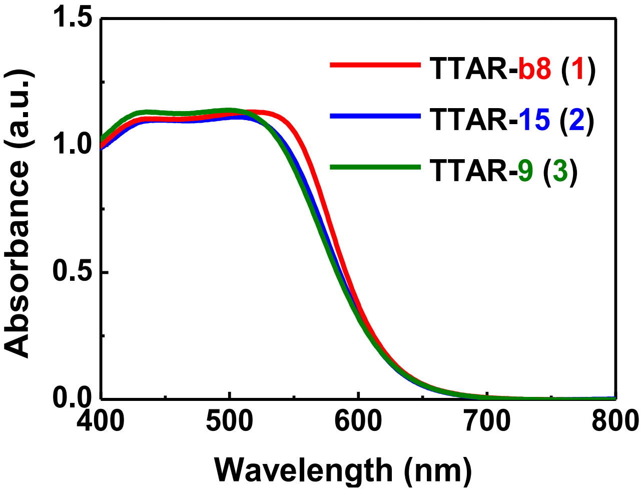

Figure 5: Absorption spectra of the dye-sensitized nanocrystalline TiO_2 films

The photovoltaic performances of the DSSCs with these dyes were measured under the irradiation of AM 1.5 G (100 mW cm^{-2}) simulated solar light, and the results are plotted in Figure6. The corresponding parameters are summarized in Table 2. The DSSCs fabricated with **TTAR-b8** show the best results among the three dyes, with a short-circuit current density(J_{SC}) of 17.45 mA cm^{-2}, an open-circuit voltage (V_{OC}) of 0.81, a fill factor (*FF*) of 0.72, and a cell efficiency (η) as high as 10.21%, while**TTAR-9** and **TTAR-15** provide relatively low ηvaluesof 7.60% and 9.02%, respectively. The superior performance of the cell based on dye **TTAR-b8** reflects the higher J_{SC}, attributable to the better light absorption characteristics of **TTAR-b8**. On the other hand, this higher J_{SC} of the **TTAR-b8**-sensitized cell could also be explained by the relatively lower aggregation of the dye due to the bulky 3-methyl-5,5-dimethylhexyl substituents.

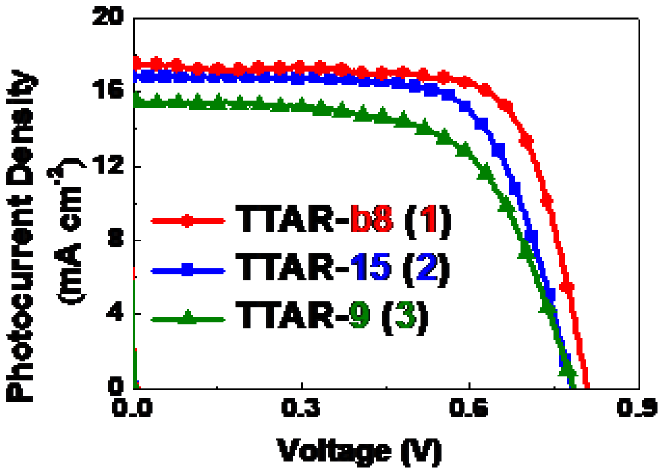

Figure 6: The photocurrent current density–voltage (J-V) characteristics of the DSSCs with various dyes, measured under 1 sun illumination

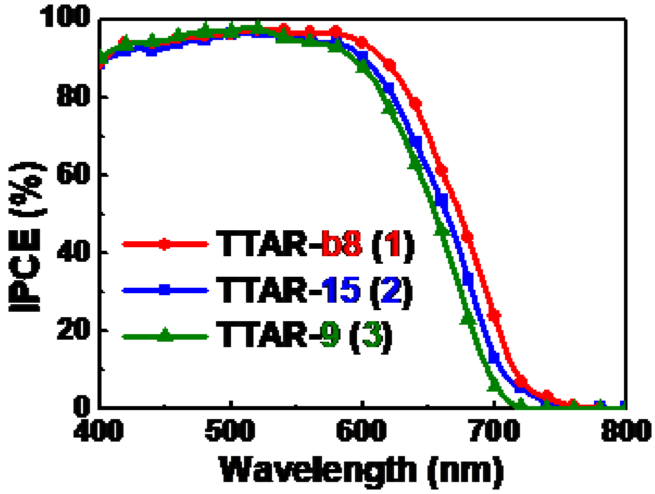

Figure 7: IPCE plots of the DSSCs with various dyes

Figure 7 shows the incident photon–to–electron conversion efficiency (IPCE) spectra for the DSSCs fabricated with these three dyes. The IPCE spectra broaden and extend to 700 nm, which is consistent with the UV-vis absorption spectra of the dye-sensitized TiO_2 films. The broadening of the IPCE spectra is associated with larger photocurrents[29] which is consistent with the higher ηobserved for the TTAR-series dyes.

Table 2: Photovoltaic parameters of the DSSCs with various dyes

Dyes	η (%)	V_{OC} (V)	J_{SC} (mA cm^{-2})	FF
TTAR-b8	10.21±0.17	0.81±0.01	17.54±0.05	0.72±0.01
TTAR-15	9.02±0.06	0.78±0.01	16.86±0.17	0.69±0.01
TTAR-9	7.60±0.07	0.78±0.01	15.54±0.06	0.62±0.01

Values obtained from three cells

As light traverses the cells, significant portions of the photon flux are not absorbed by the dye molecules, and by capturing the the lost photons, additional cell efficiency can be obtained. Therefore, a double-layer three-dimentional (3D) photonic crystal (PhC) with hole diameter of 375/410nm was placed behind the count electrode to efficiently reflect and diffract the transmitted photons back into the cell for further conversion.30,31 The photovoltaic performance of the TTAR-b8 dye DSSC with with a 3D PhC layer was measured under AM 1.5 G irradiation (100 mW cm-2) simulated solar light, and the results are plotted in Figure 8. The TTAR-b8-based cell gave a Jsc of 18.79 mA/cm^2, V_{oc} = 0.811V, a fill factor = 73.31%, and η = 11.18%. Performance parameters are summarized in Table 3. Thus, these TTAR-b8-based cells deliver the highest performance of any fused-thiophene-based DSSC reported to date.

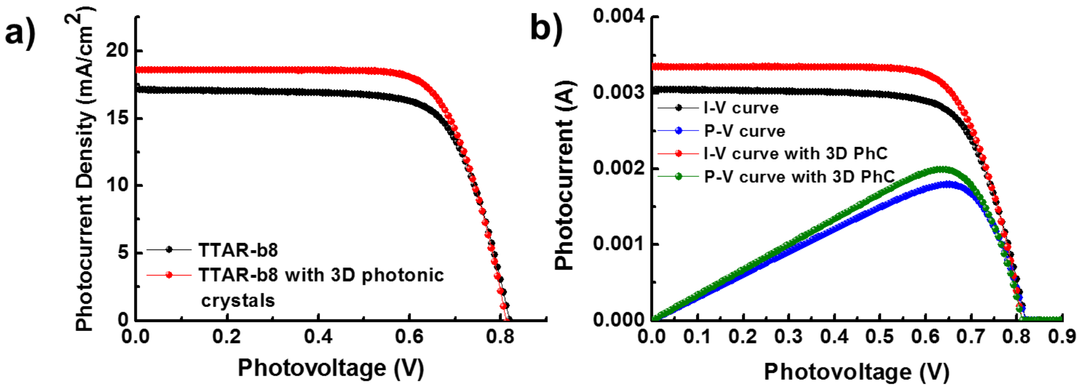

Figure 8: The photocurrent current density–voltage (*J-V*) characteristics of the DSSCs with TTAR-b8 and 3D PC under 1 sun illumination

Table 3: Photovoltaic parameters of the DSSCs with TTAR-b8 and 3D PC under 1 sun illumination

Compound	V_{OC} (V)	J_{SC} (mA cm^{-2})	*FF (%)*	*EFF (%)*
TTAR-b8	0.817	17.12	71.96	10.08
TTAR-b8 with 3D PhC	0.811	18.79	73.31	11.18

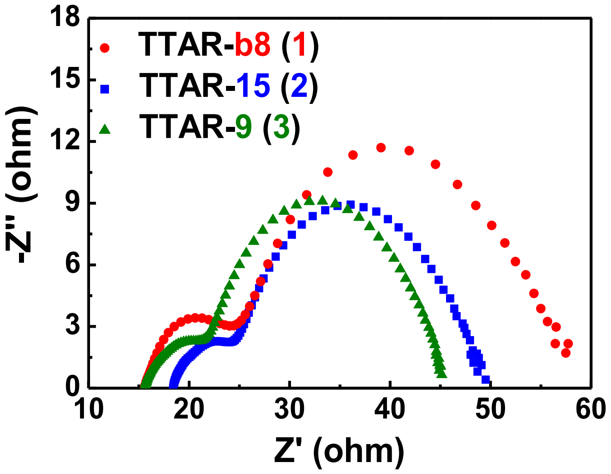

Figure 9: Nyquist plots of the DSSCs with various dyes, measured under dark conditions

Electrochemical impedance spectroscopy (EIS) was next performed under dark conditions to understand the differences in VOC for the cells sensitized by the present dyes (Figure 9). In general, the Nyquist plots show three semicircles, which are assigned to electrochemical reactions at the Pt/electrolyte interface, charge transfer at the TiO2/dye/electrolyte interface, and Warburg diffusion processes (I^-/I_3^-) in the electrolyte. In the present DSSCs, only two semicircles are observed. It is therefore assumed that in these DSSCsthe conventional diffusion resistance of the redox couple overlaps with the charge-transfer resistance, because of the relatively short length available for I- diffusion with the thin spacer and owing to the low viscosity of the electrolyte solvents. EIS analysis of the DSSCs was performed over the frequency range of 10 mHz to 65 kHz under dark conditions at an applied bias set at -0.85 V. The radius of the larger semicircle and the corresponding extracted Rrec value increase in the order, TTAR-9<TTAR-15<TTAR-b8, consistent with the observed increase of VOC in these DSSCs based on the TTAR-series dyes. A smaller Rrecvalue is indicative of faster exciton recombination, and may result in a comparatively small V_{OC}s.[32,33] Aggregation of

the dyes is reported to increase recombination rates and thus reduce the VOC.Upon illumination at 100 mW cm^{-2} under open-circuitconditions, the radius of the intermediate-frequency semicircle in the Nyquist plot (Figure 10a) hence the charge-transport resistance (R_{ct2}) follows the order, **TTAR-b8<TTAR-15<TTAR-9**. Lower values of the charge-transfer resistance should favor enhanced electron collection, and thus would play an important role in increasing the cell efficiency.

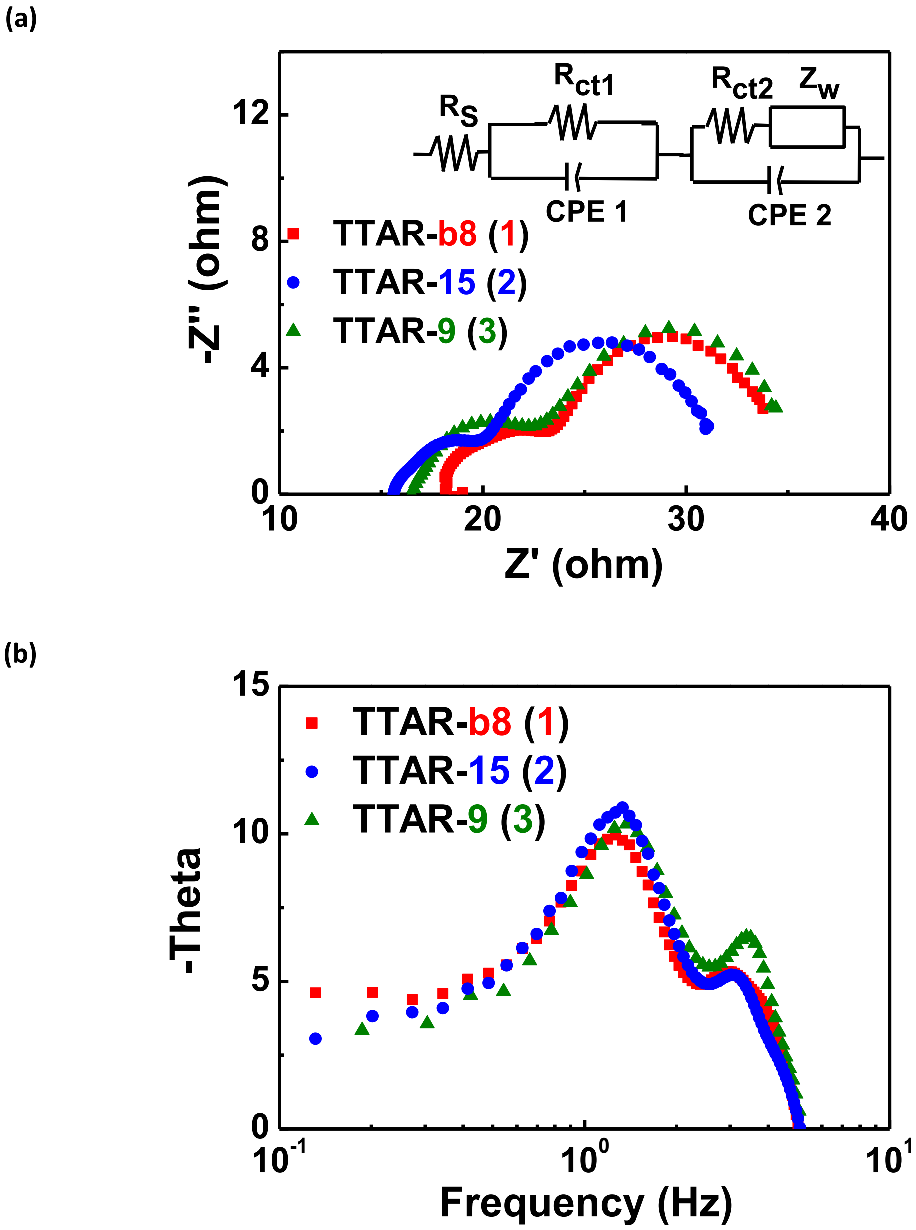

Figure 10: (a) Nyquist and (b) Bode plots of the DSSCs with various dyes, measured under 1 sun illumination

In addition, the electron lifetimes calculated from Bode plots (Figure 10b) further supports the ordering of V_{OC} in these cells. The Bode plots of the EIS spectra show the frequency peaks of the charge transfer process at different interfaces for cells with the different dyes. The electron lifetime (τe) for recombination in a DSSC is determined by the f_{max} value,[34] where $\tau_e = (2\pi f_{max})^{-1}$ and results are shown in in Table 4. The electron lifetimes measured for the dyes TTAR-b8, TTAR-15, and TTAR-9 are 8.69, 7.39, and 6.74 ms, respectively. The increase in electron lifetime for the TTAR-b8-based cell indicates the more effective suppression of the back reaction of the injected electrons with the I3- in the electrolyte, by alteration of the sensitizer HOMO, leading to increased photocurrent and photovoltage, hence to substantially enhanced η.

Table 4: Electrochemical parameters of the DSSCs with various dyes

Dyes	R_{rec}(ohm)	R_{ct2}(ohm)	f_{max}(Hz)	τ_e (ms)
TTAR-b8	35.95	14.27	18.31	8.69
TTAR-15	27.59	14.59	21.54	7.39
TTAR- 9	27.42	15.72	23.60	6.74

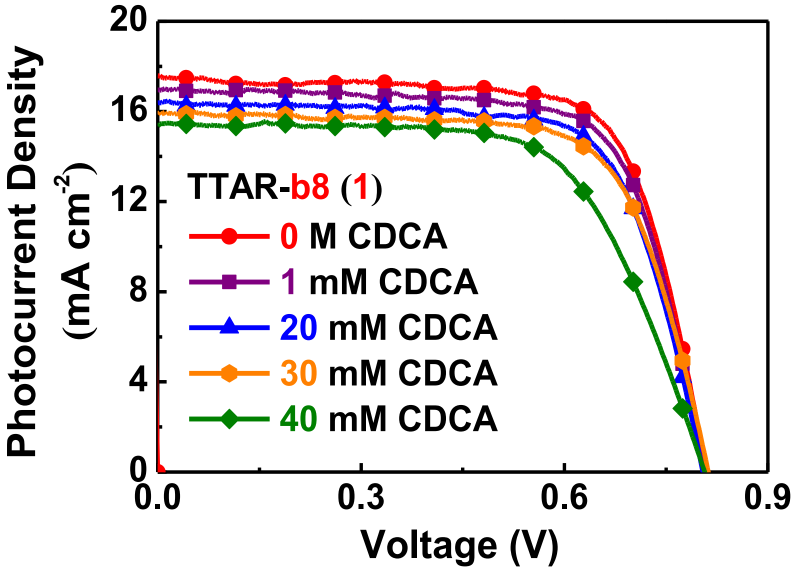

Figure 11: The photocurrent density–voltage (J-V) characteristics of the DSSCs using TTAR-b8 dye with various CDCA concentrations, measured under 1 sun illumination

Table 5: Photovoltaic parameters of the DSSCs using TTAR-b8 dye with various CDCA concentrations

CDCA	η (%)	V_{OC} (V)	J_{SC} (mA cm^{-2})	*FF*
0 M	10.21±0.17	0.81±0.01	17.54±0.05	0.72±0.01
1x10^{-3} M	9.83±0.12	0.80±0.01	16.97±0.08	0.72±0.00
10x10^{-3} M	9.37±0.06	0.80±0.01	16.40±0.05	0.71±0.01
20x10^{-3} M	9.13±0.15	0.81±0.01	15.98±0.04	0.70±0.01
30x10^{-3} M	8.12±0.15	0.81±0.01	15.39±0.05	0.65±0.01

Values obtained from three cells

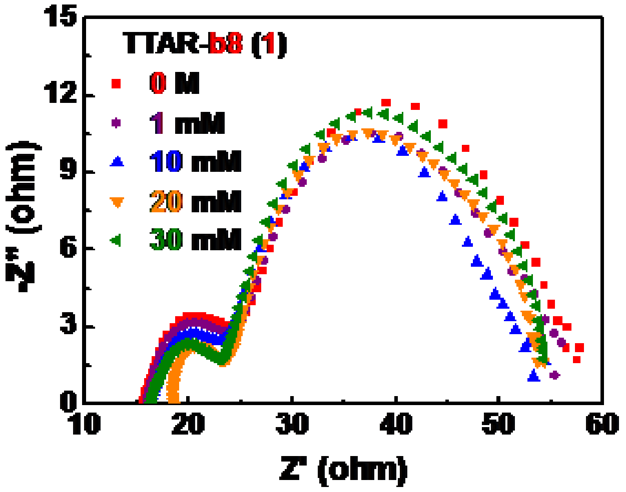

Figure 12: Nyquist plots of the DSSCs using TTAR-b8 dye with various CDCA concentrations, measured under dark conditions

(a)

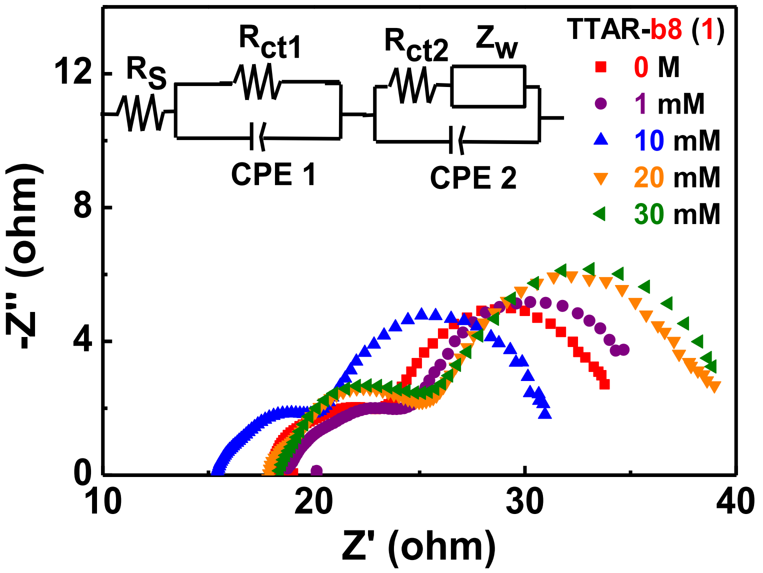

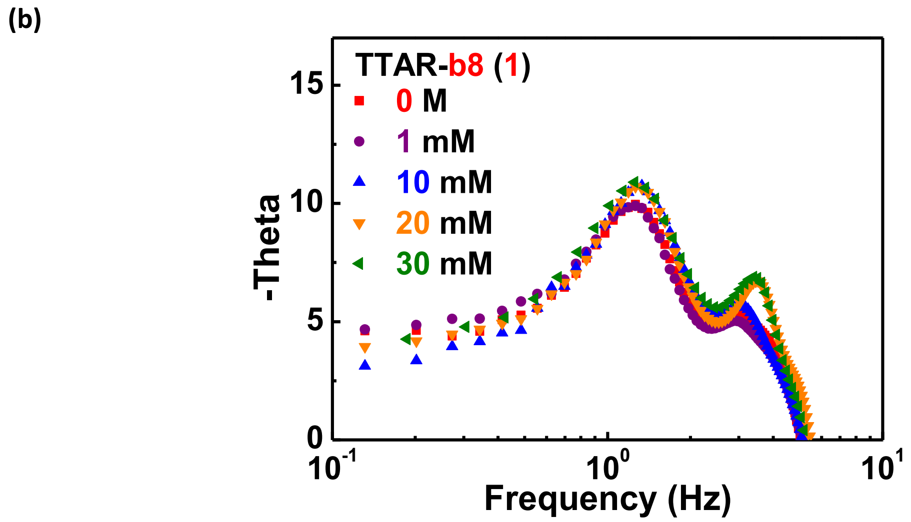

Figure 13: (a) Nyquist and (b) Bode plots of the DSSCs using TTAR-b8 dye with various CDCA concentrations, measured under 1 sun illumination

Generally, dye aggregation on the surface of TiO_2 reduces the electron lifetime and facilitates charge recombination in DSSCs fabricated using metal-organic or organic dyes.[35] To examine the possibility of dye aggregation, DSSCs were fabricated with various amounts of chenodeoxycholic acid (CDCA) co-adsorbed on the photoanodes**.** The effect of CDCA concentration on the photovoltaic properties of the DSSCs fabricated with **TTAR-b8** was first investigated, and the results are shown in Figure 11. The corresponding photovoltaic parameters are listed in Tables 5 and 6. Although dye aggregation should be suppressed by CDCA incorporation among the dye molecules, this would also decrease the dye coverage on the TiO_2. Note that $\eta$of the **TTAR-b8**-basedDSSCs decreases significantly with CDCAaddition (Table 5). The bulky 3-methyl-5,5-dimethylhexane substituent on **TTAR-b8** may be sufficient to suppress aggregation, and adsorption of the added CDCA may compete with dye adsorption on the TiO_2. Further evidence is found in the EIS data, and all extracted values are listed in Table 6. Figure 12 shows the Nyquist plots of **TTAR-b8**-based DSSCs with various CDCA concentrations, measured under dark conditions. The radius of this semicircle follows the same order, which indicates that dyes based on different concentrationsof CDCA possess similar charge-recombination resistances. Upon illumination at 100 mW cm^{-2} under open-circuit conditions, the radii of the intermediate-frequency semicircles in the Nyquist plots (Figure 13a) indicate that the electron-transport resistance (R_{ct2}) parallels the [CDCA] order 0.0 M $<$ 1 mM $<$ 10 mM $<$ 20 mM $<$ 30 mM. Moreover, the electron lifetimes can be extracted from the angular frequency

(ω_{min}) at the mid-frequency peak in the Bode phase plots (Figure 13b). The τ_e values obtained for all cells with or without added CDCA are almost identical.

Table 6: Electrochemical parameters of the DSSCs using TTAR-b8 dye with various CDCA concentrations

CDCA	R_{rec} (ohm)	R_{ct2} (ohm)	f_{max} (Hz)	τ_e (ms)
0 M	35.95	14.27	18.31	8.69
1x10^{-3} M	34.27	14.94	18.31	8.69
10x10^{-3} M	31.97	15.12	18.31	8.69
20x10^{-3} M	34.02	17.48	18.31	8.69
30x10^{-3} M	34.53	19.38	17.96	8.86

Three novel organic sensitizers containing the tetrathienoacene moiety for DSSCs. Their photophysical, electrochemical and photovoltaic properties were investigated. Introduction of a branched 3-methyl-5,5-dimethylhexane group at the TTA unit is favorable in retarding molecular aggregation and suppressing charge recombination through distorting the packing order, and thus achieves the highest cell efficiency of 10.2%. It is found that addition of CDCA has a negative effect on the DSSC photovoltaic performance.By utilizing a three-dimentional photonic crystal layer to increase light absorption, TTAR-b8 exhibits higher short-circuit current densities and achieves a high PCE of 11.2 %. This renders TTAR-b8 the highest performing fused-thiophene-based organic DSSC dye reported to date.

References:

1. O'regan, B.; Gratzel, M. *Nature* 1991, 353, 737-740.
2. Bach, U.; Lupo, D.; Comte, P.; Moser, J. E.; Weissortel, F.; Salbeck, J.; Spreitzer, H.; Gratzel, M. *Nature* 1998, 395, 583-585.
3. Grätzel, M. *Inorg. Chem.* 2005, 44, 6841-6851.
4. Hagfeldt, A.; Grätzel, M. *Acc. Chem. Res.* 2000, 33, 269-277.
5. Mathew, S.; Yella, A.; Gao, P.; Humphry-Baker, R.; Curchodbasile, F. E.; Ashari-Astani, N.; Tavernelli, I.; Rothlisberger, U.; Nazeeruddinmd, K.; Grätzel, M. *Nat Chem* 2014, 6, 242-247.
6. Yella, A.; Mai, C.-L.; Zakeeruddin, S. M.; Chang, S.-N.; Hsieh, C.-H.; Yeh, C.-Y.; Grätzel, M. *Angew. Chem.* 2014, 126, 3017-3021.

7. Yella, A.; Lee, H.-W.; Tsao, H. N.; Yi, C.; Chandiran, A. K.; Nazeeruddin, M. K.; Diau, E. W.-G.; Yeh, C.-Y.; Zakeeruddin, S. M.; Grätzel, M. *Science* 2011, 334, 629-634.
8. Hagfeldt, A.; Boschloo, G.; Sun, L.; Kloo, L.; Pettersson, H. *Chem. Rev.* 2010, 110, 6595-6663.
9. Jiao, Y.; Zhang, F.; Grätzel, M.; Meng, S. *Adv. Funct. Mater.* 2013, 23, 424-429.
10. Kozma, E.; Concina, I.; Braga, A.; Borgese, L.; Depero, L. E.; Vomiero, A.; Sberveglieri, G.; Catellani, M. *J. Mater. Chem.* 2011, 21, 13785-13788.
11. Qu, S.; Wu, W.; Hua, J.; Kong, C.; Long, Y.; Tian, H. *J. Phys. Chem. C* 2010, 114, 1343-1349.
12. He, J.; Wu, W.; Hua, J.; Jiang, Y.; Qu, S.; Li, J.; Long, Y.; Tian, H. *J. Mater. Chem.* 2011, 21, 6054-6062.
13. Kim, D.; Ghicov, A.; Albu, S. P.; Schmuki, P. *J. Am. Chem. Soc.* 2008, 130, 16454-16455.
14. Sauvage, F.; Di Fonzo, F.; Li Bassi, A.; Casari, C. S.; Russo, V.; Divitini, G.; Ducati, C.; Bottani, C. E.; Comte, P.; Graetzel, M. *Nano Letters* 2010, 10, 2562-2567.
15. Yang, J.; Ganesan, P.; Teuscher, J.; Moehl, T.; Kim, Y. J.; Yi, C.; Comte, P.; Pei, K.; Holcombe, T. W.; Nazeeruddin, M. K.; Hua, J.; Zakeeruddin, S. M.; Tian, H.; Grätzel, M. *J. Am. Chem. Soc.* 2014, 136, 5722-5730.
16. Yao, Z.; Zhang, M.; Wu, H.; Yang, L.; Li, R.; Wang, P. *J. Am. Chem. Soc.* 2015, 137, 3799-3802.
17. Chen, H.; Huang, H.; Huang, X.; Clifford, J. N.; Forneli, A.; Palomares, E.; Zheng, X.; Zheng, L.; Wang, X.; Shen, P.; Zhao, B.; Tan, S. *J. Phys. Chem. C* 2010, 114, 3280-3286.
18. Choi, H.; Raabe, I.; Kim, D.; Teocoli, F.; Kim, C.; Song, K.; Yum, J.-H.; Ko, J.; Nazeeruddin, M. K.; Grätzel, M. *Chem. Eur. J.* 2010, 16, 1193-1201.
19. Hagberg, D. P.; Marinado, T.; Karlsson, K. M.; Nonomura, K.; Qin, P.; Boschloo, G.; Brinck, T.; Hagfeldt, A.; Sun, L. *J. Org. Chem.* 2007, 72, 9550-9556.
20. Haid, S.; Marszalek, M.; Mishra, A.; Wielopolski, M.; Teuscher, J.; Moser, J.-E.; Humphry-Baker, R.; Zakeeruddin, S. M.; Grätzel, M.; Bäuerle, P. *Adv. Funct. Mater.* 2012, 22, 1291-1302.
21. Joly, D.; Pellejà, L.; Narbey, S.; Oswald, F.; Chiron, J.; Clifford, J. N.; Palomares, E.; Demadrille, R. *Sci. Rep.* 2014, 4, 4033.
22. Kim, B.-G.; Chung, K.; Kim, J. *Chem. Eur. J.* 2013, 19, 5220-5230.

23. Teng, C.; Yang, X.; Yang, C.; Li, S.; Cheng, M.; Hagfeldt, A.; Sun, L. *J. Phys. Chem. C* 2010, 114, 9101-9110.
24. Youn, J.; Huang, P.-Y.; Huang, Y.-W.; Chen, M.-C.; Lin, Y.-J.; Huang, H.; Ortiz, R. P.; Stern, C.; Chung, M.-C.; Feng, C.-Y.; Chen, L.-H.; Facchetti, A.; Marks, T. J. *Adv. Funct. Mater.* 2012, 22, 48-60.
25. Kim, C.; Chen, M.-C.; Chiang, Y.-J.; Guo, Y.-J.; Youn, J.; Huang, H.; Liang, Y.-J.; Lin, Y.-J.; Huang, Y.-W.; Hu, T.-S.; Lee, G.-H.; Facchetti, A.; Marks, T. J. *Organic Electronics* 2010, 11, 801-813.
26. Zhou, N.; Prabakaran, K.; Lee, B.; Chang, S. H.; Harutyunyan, B.; Guo, P.; Butler, M. R.; Timalsina, A.; Bedzyk, M. J.; Ratner, M. A.; Vegiraju, S.; Yau, S.; Wu, C.-G.; Chang, R. P. H.; Facchetti, A.; Chen, M.-C.; Marks, T. J. *J. Am. Chem. Soc.* 2015, 137, 4414-4423.
27. Yum, J.-H.; Holcombe, T. W.; Kim, Y.; Rakstys, K.; Moehl, T.; Teuscher, J.; Delcamp, J. H.; Nazeeruddin, M. K.; Grätzel, M. *Sci. Rep.* 2013, 3.
28. Numata, Y.; Ashraful, I.; Shirai, Y.; Han, L. *Chem. Commun.* 2011, 47, 6159-6161.
29. Paek, S.; Choi, H.; Choi, H.; Lee, C.-W.; Kang, M.-S.; Song, K.; Nazeeruddin, M. K.; Ko, J. *J. Phys. Chem. C* 2010, 114, 14646-14653.
30. Lee, B.; Hwang, D.-K.; Guo, P.; Ho, S.-T.; Buchholtz, D. B.; Wang, C.-Y.; Chang, R. P. H. *The Journal of Physical Chemistry B* 2010, 114, 14582-14591.
31. Lee, B.; Guo, P.; Li, S.-Q.; Buchholz, D. B.; Chang, R. P. H. *ACS Applied Materials & Interfaces* 2014, 6, 17713-17722.
32. Raga, S. R.; Barea, E. M.; Fabregat-Santiago, F. *The Journal of Physical Chemistry Letters* 2012, 3, 1629-1634.
33. Li, G.; Liang, M.; Wang, H.; Sun, Z.; Wang, L.; Wang, Z.; Xue, S. *Chem. Mater.* 2013, 25, 1713-1722.
34. Van De Lagemaat, J.; Park, N. G.; Frank, A. J. *J. Phys. Chem. B* 2000, 104, 2044-2052.
35. Lu, M.; Liang, M.; Han, H.-Y.; Sun, Z.; Xue, S. *J. Phys. Chem. C* 2011, 115, 274-281.
36. Chang, S. H.; Chiang, C.-H.; Cheng, H.-M.; Tai, C.-Y.; Wu, C.-G. *Opt. Lett.* 2013, 38, 5342-5345.
37. Giriffith, M. J.; James, M.; Triani, G.; Wagner, P.; Wallace, G. G.; Officer, D. L. *Langmuir* 2011, 27, 12944-12950.
38. Parratt, L. G. *Physical Review* 1954, 95, 359-369.

THE COMPOSITION OF COMETARY DUST PARTICLES

Madhujya Gogoi
Department of Physics,
Dhemaji College Dhemaji, Assam
Corresponding author E-mail: mgogoi2001@rediffmail.com

Introduction:

The comet is low-mass member of the solar system. Moving in a highly elliptical orbit and undergoing great changes in appearance as it approaches and then recedes from the sun. comet is highly insubstantial. their only solid part in the nucleus , typically no more than the few kilometers across a “dirty snowball” of Ice with a dust crust cometary nuclei spend most of their lives unseen in the outer reaches of their ,orbit far from the sun gravitational disturbance may send some of them on highly elliptical orbit towards the inner solar system as a comet nucleus approaches the sun, dirty snowball warms up and released gas and dust to from a coma, perhaps 10 times the diameter of the earth, yet so tenuous that it is transparent. Gas and dust steam away from the coma to produce tails that is extreme cases, could stretch from Earth to the Sun. Comet have two tails, one of dust and one of gas. Gas tails consist of ionized molecules and have a bluish color; they are almost straight and are carried directly away from the sun by the charged particles of the solar wind. Dust tails are curved because the dust particles lag behind the comet’s motion; they appear yellowish because the particles reflect sunlight. Cometary dust disperses into space where it is eventually swept up by the planets or falls into the Sun. Dust particles from comets produce the bright streaks known as meteors when they burn up in Earth atmosphere.

Review of Literature:

Comets were first recognized as solar system objects in 1577 but it was not until 1705 that Halley first derived a comet orbit and predicted the return of the comet. Since then, a great deal of orbital data has been obtained, some of admittedly dubious accuracy. The Standard catalogues of comet orbits are those of Galle (1894), Crommelin (1925, 1932), and, Porter (1961). The “dirty snowball” model proposes by F. whipple in (1950). The visual diameters range up to about 106 km, with an average value of say 5x104 km diameter (Beyer1933,1959), although photographic determinations will generally be somewhat lager. The emissions are given by Richter (1963). The following compounds and ions have been clearly identified in cometary heads: **CN, C_2, CH, CH', NH, NH_2, CO_2^+, CO', N_2^+, OH^+, OH', Na and C_3.**

There are two general classifications of comet tails known as Type I and Type II or III (Biermann 1951, 1953, 1963). Type I tails consist of relatively easily accelerated particles, mainly ion **S_6** such a s **CO^+, N_2^+, CO_2^+, CH', OH'** (Swings and Haser 1961). Missions to Periodic Comet Encke (1974) The frequent observation of Encke has resulted in well-established orbital parameters and well calculated perturb active influences. The compounds which have been detected in the coma of Encke are **CN, C_2, C_3** (Strongerin 1947 than in 1937), **NH, OH** (Nsstrong as NH), and CH (Swings and Haser 1961).

The dust contains a sizeable but hitherto unobservable component of extremely fine size $<10^{17}$ kg in mass. the dust contains a major fraction of so-call **CHON** basic elements. The overall composition shows that no lack of **C'**are earlier suspected relative to comparative solar values. Also, the isotopic ratios, **$^{13}C/^{12}C$, $^{15}N/^{14}$ N** and newly observed **$^{34}S/^{32}S$** although not precisely measured, appears to be a typical of solar system value. the **CO** molecule appear to be an order of magnitude more abundant than **CO_2,** while the abounded **NH_2** and **CH_4** can only be given as upper limits H_2O being the major ice (~80% of ice). The low density of the nucleus suggests that no serious radioactive heating has occurred, particularly not by **^{26}Al**. (**F.L Whipple** 1987).

The infrared observation, it seems that these particles ate mainly composed of silicates, as infrared by strong absorption featured at 9.7 μm. Among other a component of an amorphous olivine such as **$MgSiFO_2$** seems to fit the astronomical observation (Greenberg and Li,1996).

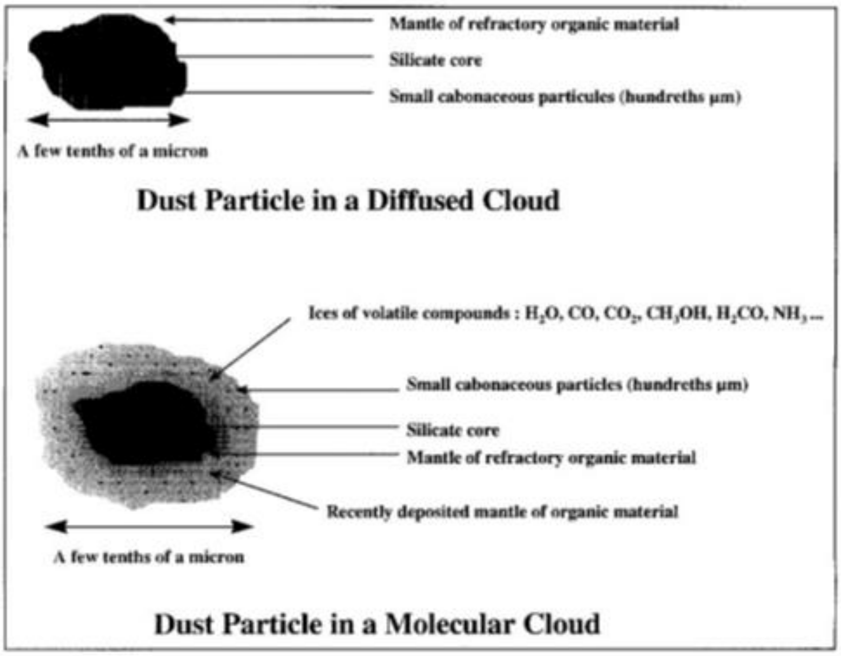

Figure 1: Interstellar dust particle in diffuse and molecule clouds. From Greenberg's Model

The observations and laboratory simulations: 26% of a comet consists of silicates, 23% of a refractory organic mantle and 9% are atto-gram particles. The 42% remaining consists of a mixture of volatile compounds dominated by water (around 80% by number). the heavy-ion mass spectra from the PICCA instrument led Huebner (1987) to conclude the presence of polyoxymethylene in comet Halley.

After further analyses Huebner *et al.* (1989) confirmed that detection and discussed the presence of POM derivatives such as sulfur copolymers. The presence of POM in comets is coherent with the detection of extended sources of ` and **H_zCO** in the coma. Indeed, these molecules could be photodecomposition products of POM. The authors also suggest the presence of HCN polymers such as poly amino cyan methylene (PACM: (NH, -C-CN),), even if these polymers should be very difficult to detect because in the coma HCN/HCO - 0.1(Huebner et al., 1989). Moreover, HCN polymers should be more difficult to detect than H, CO's ones: Krueger etna. (1991) have calculated from thermodynamic considerations that N containing polymers should be less volatile than O containing polymers. The presence of HCN/H, CO copolymers could also be suggested on comets because these two molecules polymerize very easily by themselves. Therefore, PICCA mass spectra do not imply the presence of POM, but only of a large diversity of CHON molecules, among which POM could be present. The most we can say, if we consider laboratory simulation results, is that the presence of **POM** on cometary nuclei is possible. (H. Cottin", M.C. Gazeau, F. Raulin 1998).

The observations from space were obtained with HST (Lamy et al., 1998; Stern et al., 1998), ISO (Colangeli et al., 1998) and SOHO (Bertaux et al., 1998). The neutral and ionized gas species detected in Comet 46P/Wirtanen. All of them are typically present in comets. The first gaseous species (CN) was firmly detected at rH = 2.34 AU (Schulz et al., 1998). A possible marginal detection of OH at rH = 2.47 AU was reported by Stern *et al.* (1998) The comets contain a mixture of silicates, both amorphous and crystalline, that do not necessarily share a common origin. Comets formed in regions of the solar nebula where the temperature was too low to sublimate refractory interstellar grains. Boss (1994, 1998) predicts that the temperature at $r \geq 5$ AU was ≤ 160 K. The high CO: H_2O ratio in comets implies that even interstellar ices may have survived. Thus, it is possible that all cometary silicates are of pre-solar origin. (MARTHA S. HANNER;1999).

The four giant planets are enriched in carbon with respect to the solar abundance (Gautier and Owen, 1989). the Galileo probe performing in situ measurements in the troposphere of Jupiter found that **C, N, S, Ar, Kr** and **Xe** were all enriched by a factor (Owen et al., 1999;

Mahaffy et al., 2000). This uniform enrichment was unexpected. Moreover, Cochran *et al.* (2000) and Cochran (2002) observed that N2 is strongly depleted with respect to CO in three comets originating from the Oort cloud. The six following elements were measured enriched by a factor 2 to 4 with respect to the solar abundance of Anders and Grevesse (1989): **Ar, Kr, Xe, C, N**, and **S** (Atreya et al., 1999; Mahaffy et al., 2000).

The composition of dust particles emitted from the Jupiter family comet 67P/C-G was measured with the COSIMA instrument on board the Rosetta spacecraft. the dust chemical properties and part of the physical structure (e.g., the porosity of the particles) (Hornung *et al.* 2016; Langevin *et al.* 2016). The relative elemental composition of 67P/C-G particles have been measured in about 30 particles for the following elements**: C, N, O, Na, Mg, Al, Si, K, Ca, Cr,** Mn and Fe (Bardyn *et al.* 2017; Fray *et al.* 2017). This is broadly similar to the results from 1P/Halley and 81P/Wild 2. Some caution has to be taken in comparing data in representations such as (Fig: -2).

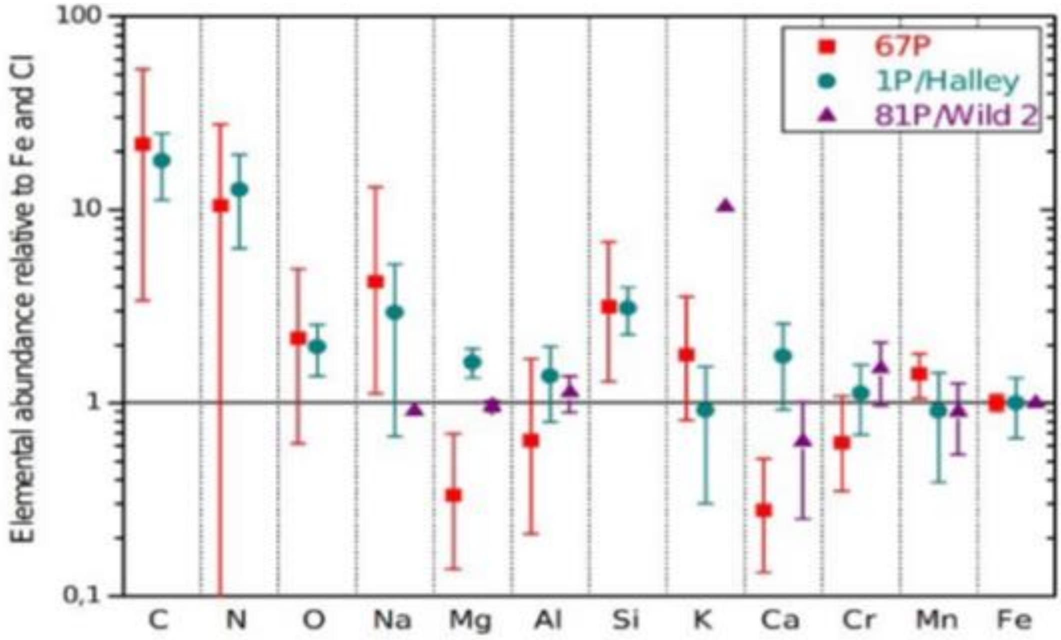

Figure 2: Comet 67P/C-G dust element ratio relative to Fe and to Cl Chondrite composition

The abundance of Si and Na show a similar trend in comets 1P/Halley and 67P/C-G. Na was also observed in the upper atmosphere of Mars by the MAVEN spacecraft, as the most abundant element detected during the ablation of particles from the passage of comet C/2013 A1 (Benna *et al.* 2015). Mg and Ca are quite low in 67P/C-G. The high K in (Fig:- 2) is based on TOF-SIMS analyses of craters in the Al foil of Stardust and of slices of tracks in the aerogel

(Stephan *et al.* 2008). The data for the three comets points toward rather primitive bodies, globally close to solar abundance, except for nitrogen, which although enriched with regard to the CI composition, is always strongly depleted with regard to the solar value.

Although interstellar silicates are known from astronomical observations to be almost entirely amorphous, approximately half of the silicates in 81P/Wild 2 samples are crystalline (Westphal *et al.* 2009; Stodolna *et al.* 2014). Among crystalline minerals, olivine's**, pyroxenes** and **Fe** sulfides are the most abundant minerals present in the 81P/Wild 2 samples, contained large amount of fine-grained matrix (individual size of minerals <1 μm) that did not survive well the impact. This fine-grained component got mixed with melted aerogel in the walls of the impact tracks and contains olivine, pyroxenes and Fe sulfides. The composition of this fine-grained component is close to the chondritic CI composition (Leroux *et al.* 2008; Leroux 2012; Leroux and Jacob 2013).

Although not common**, Fe–Ni** metal particles at least up to 20 μm in size are present in 81P/Wild 2. One particle that was studied in detail has an unusual composition reminiscent of metals found in ureilites, a family of meteorites that is poorly understood but may have a composition consistent with smelting of silicates in a carbon-rich environment, with Fe originally in silicates reduced to metal (Westphal *et al.* 2012; Humayun et al.2015). Small amounts of minerals possibly resulting from aqueous alteration have been identified in 81P/Wild 2 samples, like magnetite grains (Stodolna *et al.* 2012), carbonates (Flynn 2008; Flynn *et al.* 2009a; Mikouchi *et al.* 2007; Wirick *et al.* 2007; Leroux 2012), and a copper iron sulfide (cubanite) in association with pyrrothite and pentlandite (Berger *et al.* 2011). No hydrated silicates have been identified in 81P/Wild 2 samples. the material in the inner nebula, that must have been responsible for converting interstellar dust to nebular and cometary dust. Despite the evidence for the presence of inner Solar System material in 81P/Wild 2, the distribution of types and compositions of materials in 81P/Wild 2 differs from materials observed in meteorites.

The Rosetta space experiment, the material sampled directly from the surface of a cometary nucleus was examined for the first time. In its composition, 16 different organic compounds were identified, including carboxylic acids, polyoxymethylene, amino acid glycine (C_2H5NO_2), and phosphorous, without which proteins cannot be synthesized; four compounds—methylisocyanate (CH_3NCO), acetone (CH_3COCH_3), propionic aldehyde (C_2H_5CHO), and acetamide (CH_3CONH_2)—have never been detected in comets before. Some of these compounds, especially those containing carbon−nitrogen bonds, play a key role in the synthesis of amino acids, sugars, and nucleons. Thus, taking account of the large amount of water and carbon dioxide, we may conclude that the cometary matter contains building blocks to synthesize amino acids, sugars, and nucleons the components required for the germ of life. These results move us forward in understanding the origin of life on the Earth. The composition of the ice fraction of the 67P/C-G nucleus was studied from the composition of the coma, within which the relative abundances of 24 parent molecules were measured; among them are such macro components as H_2O, CO_2, and CO, light hydro carbons, compounds of nitrogen and sulfur, and molecular O_2. Molecular nitrogen N_2 was for the first time detected in the cometary coma; and its relative abundance was determined as $N_2/H_2O = (8.9 \pm 2.4) \times 10^{-4}$, which is more than 25 times lower than the solar proportion. The nitrogen deficit, which is typical of all comets, suggests that the temperatures in the region, where proto cometary bodies were formed, did not reach the temperature of formation of N_2(ice) (~22 K); and highly volatile N_2 and Ar may be accumulated in pores of amorphous water ice formed in the presolar nebula, which may be evidenced by a strong correlation determined for the N_2 and ^{36}Ar contents. (V. A. Dorofeeva 2019. Organic molecules detected in comets via Earth-based remote sensing.

Volatile component of the coma:

Around 30 molecules have been identified remotely in cometary atmospheres with abundance relative to water often varying by one order of magnitude. The range of abundances measured and the number of comets in which they have been detected. The Rosetta mission has nearly doubled this number of molecules. The present status of abundances measured in comets and in 67P is summarized in Table:1 and detailed hereafter.

Hydrocarbon:

Symmetric hydrocarbons such as CH_6, C_2H_6, C_2H_2, and C_2H_4 are investigated remotely in the IR. Based on the growing database of comet observations there is evidence that, C_2H_6, and C_2H_2 are depleted in Jupiter family based on the expanding information of comet observation. These and more complex hydrocarbons were detected in the coma of 67P using the ROSINA mass spectrometer during the Rosetta mission. Table:1 updated from information in Bockelee-Morvan and Biver (2017); Biver *et al.* (2021a); Rubin *et al.* (2019); Dello Russo *et al.* (2016a); Lippi *et al.* (2021).

Table 1: Molecule abundant in atmospheres (Abundance relative to water in %)

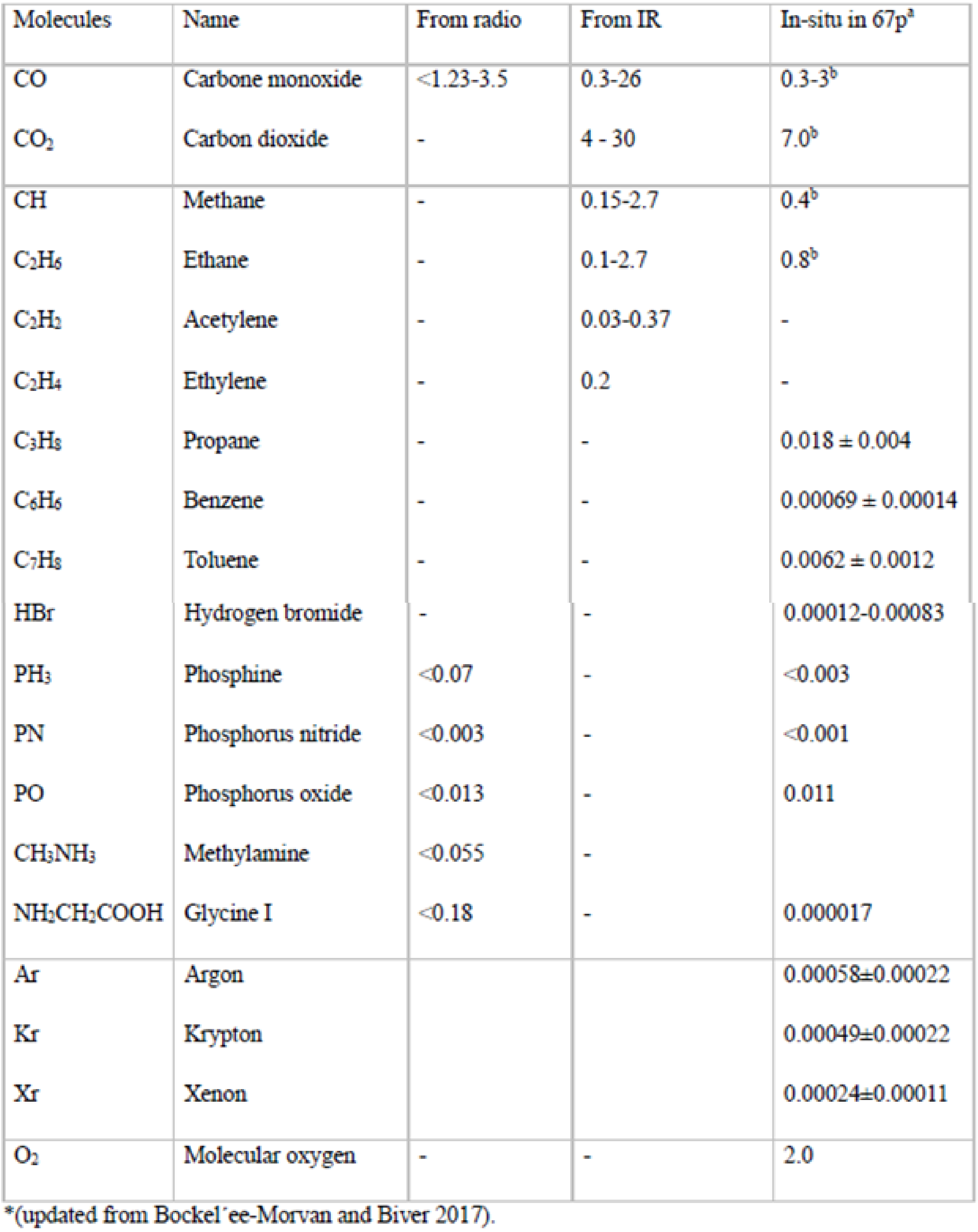

Molecules	Name	From radio	From IR	In-situ in 67p^{a}
CO	Carbone monoxide	<1.23-3.5	0.3-26	0.3-3^{b}
CO_2	Carbon dioxide	-	4 - 30	7.0^{b}
CH	Methane	-	0.15-2.7	0.4^{b}
C_2H_6	Ethane	-	0.1-2.7	0.8^{b}
C_2H_2	Acetylene	-	0.03-0.37	-
C_2H_4	Ethylene	-	0.2	-
C_3H_8	Propane	-	-	0.018 ± 0.004
C_6H_6	Benzene	-	-	0.00069 ± 0.00014
C_7H_8	Toluene	-	-	0.0062 ± 0.0012
HBr	Hydrogen bromide	-	-	0.00012-0.00083
PH_3	Phosphine	<0.07	-	<0.003
PN	Phosphorus nitride	<0.003	-	<0.001
PO	Phosphorus oxide	<0.013	-	0.011
CH_3NH_3	Methylamine	<0.055	-	
NH_2CH_2COOH	Glycine I	<0.18	-	0.000017
Ar	Argon			0.00058±0.00022
Kr	Krypton			0.00049±0.00022
Xr	Xenon			0.00024±0.00011
O_2	Molecular oxygen	-	-	2.0

*(updated from Bockel´ee-Morvan and Biver 2017).

Deuterated water (D_2O heavy water) in the interstellar medium:

It has long been known that the cold temperatures found in dense molecular clouds (∼10–30 K) would be conducive to the selective incorporation of deuterium atoms into interstellar molecules (see Watson 1976 and references therein). At 10 K, the zero-point energy difference between H_2D and leads to H_3^+ the former ion becoming sufficiently abundant that large numbers of D atoms can be distributed to other molecules through ion-molecule exchange reactions (e.g., Millar *et al.* 1989). The abundance of deuterated molecules can be significantly enhanced (to a few percent of the common variant), compared to the much smaller Galactic D/H ratio (∼1.5X 10-5). The main reservoir is HD, but electron dissociative recombination of H_2D+ leads to enhanced concentrations of free D atoms in the gas. Catalytic reactions on dust grains, driven by the accretion of H and D atoms from the gas, can therefore also produce large D enrichments in interstellar ices (Tielens 1983; Charnley *et al.* 1997). Deuterium enrichments are found in meteorites and comets, and so interstellar deuteration may have a connection with that of primitive solar system matter (e.g., Nuth *et al.* 2006). Over the last few years, observations have found very high D/H ratios in some molecules, ∼10,000 times the Galactic value (for reviews, see Ceccarelli 2002; Roueff & Gerin 2003; Ceccarelli *et al.* 2007), as well as doubly deuterated and triply deuterated isotopologues of common interstellar molecules such as ammonia, hydrogen sulfide, thioformaldehyde, formaldehyde, and methanol (Lis *et al.* 2002; van der Tak *et al.* 2002; Vastel *et al.* 2003, 2004; Marcelino *et al.* 2005; Parise *et al.* 2002, 2004). The region containing the low-mass protostellar binary system IRAS 16293-2422 has been particularly well studied in deuterated molecules (van Dishoeck *et al.* 1995; Ceccarelli *et al.* 2007). In IRAS 16293-2422, it appears that several of the deuterated molecules (e.g., water and methanol; Parise *et al.* 2002, 2005) are present in small "hot corinos," the low-mass analogs of the hot molecular cores found in regions of massive star formation, in which icy grain mantles have been evaporated (Cazaux *et al.* 2003; Kuan *et al.* 2004; Bottinelli *et al.* 2004). The origin of this "super deuteration" lies in gas-grain chemical processes associated with cold prestellar cores. In these dense regions (≥106 cm3) as CO molecules are lost from the gas through condensation onto dust (e.g., Bacmann *et al.* 2003), the abundances of D_2H^+,HD_2^+,D_2^+ and atomic D all increase dramatically and drive the fractionation chemistry to produce greatly elevated molecular D/H ratios (Roberts *et al.* 2003). Comparison of the HDO/H_2O ratios of comets with that of ocean water and with interstellar ratios can provide important cosmogonic information (Meier *et al.* 1998; Bockele´e-Morvan *et al.* 1998). In moving toward a complete understanding of interstellar deuterium chemistry, the detection of several key isotopologues will be required. An important, yet puzzling, aspect of interstellar deuteration concerns the markedly low levels of deuterium fractionation commonly measured in water, especially when compared to other molecules. The lower HDO/H_2O ratios (~3 X 10-4) measured in massive hot molecular cores (e.g., Jacq *et al.* 1990; Gensheimer *et al.* 1996) are consistent with ion-molecule chemistry at around 30 K (Millar *et al.* 1989), whereas the highest ratios (0.004–0.01) are more suggestive of grain-surface reactions (Pardo *et al.* 2001). Recently, it has become possible to compare solar system D/H ratios with those of more primitive analog systems. In the protostellar binary system IRAS 16293-2422, the bounds on the measured range of HDO/H_2O ratios (to; 2 X 10-4 to 3 x10-2) stark *et al.* 2004; Parise *et al.* 2005) are determined by the abundances measured in the cold extended envelope and in the hot corino. Furthermore, Ceccarelli *et al.* (2005) have detected HDO in the DM Tau protoplanetary disk and have argued that photo desorption of water ices could lead to (Cec- HDO/$H_2O \geq 0.01$ in the outer disk gas Cec-carelli & Dominik 2005). Interstellar water could be formed by three distinct chemical routes, and the deuterium fractionation expected from each has been evaluated: hydrogenation of oxygen atoms on cold dust grains (e.g., Caselli *et al.* 2002), ion-molecule reactions in cold gas (e.g., Millar *et al.* 1989), and neutral-neutral reactions in hot shocked gas (Bergin *et al.* 1999). Observations of multiply deuterated molecules could in principle distinguish between gas-phase or grain-surface deuteration pathways (Rodgers & Charnley 2001). In the case of, measuring the abundance of heavy H_2O water (D_2O) could shed light on both the origin of water and D_2O the evolution of molecular clouds (Rodgers & Charnley 2002). In this Letter, we report the discovery of interstellar heavy water in absorption toward IRAS 16293-2422. The D_2O Spectrum Figure 1 shows the resulting JCMT spectrum after subtraction of the 850mK continuum level (which was found to be consistent with the background continuum observed by SCUBA). In the same figure, we also display the spectrum of the HDO fundamental transition at 464 GHz, obtained with JCMT by Stark *et al.* (2004) and Parise *et al.* (2005). The D_2O and HDO spectra are very similar: they both show a narrow absorption dip at the systemic velocity of IRAS 16293-2422 (~4.0kms-1) superimposed on an emission component whose width is about 6 kmS-1. In addition, the D_2O spectrum shows the presence of an emission line at about 10 kmS-1. The reality of this line was checked by changing the tuning at a different frequency. In order to derive the para-D_2O line-integrated intensity, we fitted the data with a two-component Gaussian model, fixing the line centers of the absorption and emission component according to that found for the HDO line (Stark *et al.* 2004; Parise *et al.* 2005. One additional spectral component is present around 10 km s-1, corresponding to a rest frequency of 316.793 GHz, when considering the systemic velocity (~4.0 kmS-1). We inspected the Jet Propulsion Laboratory spectroscopy database and the Cologne Database for Molecular Spectroscopy (Pickett *et al.* 1998; Muller *et al.* 2001) and identified a few candidate species. Ethanol (C_2H_5OH) has a line at the right frequency (316.793460 GHz), but the observed signal would imply an implausibly large ethanol column density, and so we discard this possibility. Dimethyl ether (CH3OCH$_3$) and SO^{17}O, the next most plausible lines, would require velocity shifts of -1.2 and -3.9 kmS-1, respectively, from the nominal core to match the observed line profile. In ad- VLSR dition, the column density of both species would be 10 times larger than those derived by previous observations (Cazaux *et al.* 2003; Wakelam *et al.* 2004). We therefore consider these identifications to be highly unlikely. On the other hand, the line intensity of the CH$_3$OD (70-60 +) transition at 316.795074 GHz (Walsh *et al.* 2000) is in agreement with the previous detection of this molecule in IRAS 16293-2422 (Parise *et al.* 2002), and we therefore consider this to be the likely identification. The presence of the D$_2$O line and the line at 10 kmS-1 are confirmed by earlier lower spectral resolution data obtained with the Caltech Submillimeter Observatory (CSO) 10 m telescope on 2001 August 1. The spectra were taken in chopping secondary mode with a chop throw of 900. The back end used was an acusto-optical spectrometer with 500 MHz bandwidth, providing a velocity resolution of 1.33 kmS-1. The beam efficiency at 316 GHz was measured to be 0.75, and the beam size is 22". The system temperature was typically 1000 K, and a rms of 15 mK was reached after 60 minutes of integration. The integrated line intensities measured at CSO are about a factor 2 lower than those measured at JCMT; within the calibration uncertainties (~20%), this is consistent with the emission of both lines originating in a region of size equal to or smaller than the JCMT beam. Given their higher spectral resolution, only the JCMT measurements are presented here. In summary, using the velocity parameters of the known HDO emission, we can reproduce both the absorption feature and most of the broad emission centered around the nominal source velocity for the D2O line at 316.8 GHz. Another feature appears at about 10 kmS-1 due to CH $_3$OD.they are detected heavy water (D$_2$O) in an astronomical DO$_2$ environment for the first time. In IRAS 16293-2422, we determine a total D$_2$O column density of 1.0X 1013 cm2 and a 13 fractional abundance of D$_2$O/H2=1.7X 10-10. The derived deuterium fractionation ratios are D$_2$O/HDO=1.7 X 10 -3 and D$_2$O/H$_2$O=5 X10-5. Shock chemistry can be ruled out as contributing to the origin of the water in this source. At steady state, grain-surface chemistry and ion-molecule reactions both predict ratios DO/HDO2 ≈4–5 times higher than observed. However, in the latter case, lower ratios D$_2$O/HDO are possible if the gas-phase chemistry of water and its deuterated isotopologues did not attain a chemical steady state prior to most of the molecules condensing onto dust grains. This scenario is also consistent with the low fractional abundance of water measured in IRAS 16293-2422 and is generally consistent with rapid molecular cloud formation and proto stellar evolution (di Francesco *et al.* 2007; Ceccarelli *et al.* 2007). As it is becoming clear that extreme deuteration appears to be common around low-mass protostars (Ceccarelli *et al.* 2007; Parise *et al.* 2006), it is likely that the D$_2$O/HDO/H$_2$O ratios can be determined in other sources and so shed further light on the chemistry of interstellar isotopic fractionation. Multi transition observations of additional sources are also needed to obtain reliable H_2O abundances (Maret *et al.* 2002; Butner, *et al.* 2007) .

Water existences on earth:

One such isotopic ratio, that of deuterium to hydrogen (D/H), is particularly useful in the search for the origin of water on Earth. Hydrogen is the most abundant element in the universe, and its heavier isotope deuterium can sometimes take the place of a hydrogen atom in molecules like H_2O. Most deuterium was created in the Big Bang or in supernovae, The deuterium to hydrogen ratio for ocean water on Earth is known very precisely to be $(1.5576 \pm 0.0005) \times 10{-}4$. (Hagemann, R; Nief, G; Roth, E., January 1970) This value represents a mixture of all of the sources that contributed to Earth's reservoirs, and is used to identify the source or sources of Earth's water.

The amorphous component:

In order to find the mass fraction contained in the crystalline silicates, the total mass in the amorphous component has to be determined, which depends on its composition. The chemical composition of amorphous silicates is determined by the formation path. Amorphous silicates resulting from the amorphization of crystalline silicates will have the stoichiometry of that crystal, while amorphous silicates formed through direct condensation from a gas cloud or by collisions and subsequent merging of two distinct grains are most likely to have a non-stoichiometric composition. Most measurements of the optical properties of amorphous silicates are limited to the stoichiometries of olivine’s and pyroxenes, except for a recent study by Ja¨ger *et al.* (2003a), who applied the sol-gel method to construct amorphous silicates of some selected non-stoichiometric compositions. In the sol-gel method, Mg- and Si-hydroxides [$Mg\ (OH)_2$ and $Si\ (OH)_4$] are mixed in the liquid phase. Ex-traction of H_2O by chemical reaction between the Mg- and Si-hydroxides then gives rise to the formation of silicates. Because the two components can be mixed in any desired ratio, it is possible to synthesize non-stochiometric amorphous Mg-silicates. For more details, the reader is referred to the work by Ja¨ger *et al.* (2003a). However, the spectral appearance of these materials does not match the interstellar absorption feature, therefore we only consider stoichiometric compositions. We have used the optical constants determined by Dorschner *et al.* (1995) for olivine ($MgFeSiO_4$) and pyroxene ($MgFeSi\ _2O_6$). The use of laboratory optical constants allows us to immediately convert the derived optical depths into column densities of dust as well as derive their chemical composition. The appearance of the 10 μm feature depends on the grain shape and grain size of the silicate particles. overview of the most important effects is given for both amorphous olivine and pyroxene. Small spherical grains (up to ~ 0.1 μm in size) all produce exactly the same shape for the spectral feature. (For larger grains, the feature starts to broaden toward longer wavelengths. This effect becomes stronger with increasing grain size) The use of non-spherical grains, represented by a continuous distribution of ellipsoids (CDE; Bohren & Huffman 1983), tends to shift the peak of the feature to longer wavelengths. With CDE calculations it is impossible to include any information on grain size. Amorphous olivine, in the form of spherical grains small in size compared to the wavelength (the Rayleigh limit), provide a good fit to the 10 μm feature (Vriend 1999). It is even possible to exclude the presence of a high fraction of larger grains, as well as more than 1% of the mass in the form of forsterite, based on this spectrum (Bouwman *et al.* 2001). They are fine, however, that the fit using just amorphous olivine can be further improved by adding amorphous pyroxene (also in small spherical grains). This is consistent with the suggestion that part of the silicates in the ISM is converted from olivines into pyroxenes to explain the pyroxene presence in protostars (Demyk *et al.* 2000).

The results of a study on the crystallinity of silicates in the diffuse ISM have been presented. It is known that crystalline silicates are common in the circumstellar environment of both pre- and post–main-sequence stars. It is generally accepted that the dust particles found in the circumstellar environment of young stars originate from evolved stars, and have arrived in their current location after a long (several Gyr) residence time in the ISM. The puzzling lack of evidence of crystalline silicates in the ISM prompted us to set a firm upper limit on the crystallinity.

Studying the 10 μm silicate feature in absorption toward Sgr , they are able to determine that at most 0.4% of the silicates in the ISM have a crystalline structure. The data are best fitted with a degree of crystallinity of 0.2%. In addition, they have determined the composition of the amorphous silicate component in the diffuse ISM. They are founding that 84.9% of the amorphous grains are olivine ($Mg2x\ Fe\ 2(1\text{-}x)\ SiO_4$) and 15.1%are pyroxene ($Mg\ x\ Fe\ (1\text{-}x)\ SiO_3$). The amorphous grains were found to be spherical and smaller than ~0.1 μm in radius. Detailed analysis of the 10 μm feature indicates that the pyroxenes are probably slightly Mg-rich (with $0:5 < x < 0:6$), and the interstellar olivines may be Fe-rich (with $0:4 < x < 0:5$).

By comparison of these results with the crystallinity of the silicates produced by mass-losing stars, and the interstellar grain destruction rate, we have determined the interstellar amorphization rate and found that crystalline silicates are effectively amorphized in 5 Myr to achieve a final crystallinity of 0.2%, while an amorphization timescale of 9 Myr is consistent with the determined upper limit of 0.4%. These numbers are only estimates, as the crystallinity of stellar ejecta has not yet been determined very accurately.

The crystalline silicates found in the circumstellar environments of young stars, in the solar system, and in star formation regions have not survived the ISM unaltered but are probably crystallized locally. Both annealing and evaporation followed by condensation seem to be significant crystallization processes. (F. Kemper et al, 2004).

Exotic molecule:

The comet becomes visible when the coma's gas and dust are brighter by the sun's flood. A few comets have a lot of dust. Their apparent light is mainly just sunlight that has been bloom somewhat by the dust. Not much dust is arrived in other comets. Such gaseous comets grow extremely bright only by a twofold process because molecules and atoms in a gas scatter light quietly. At fast, the sun's UV radiation bust molecules apart; water, for instance, becomes split into hydrogen (H) and hydroxyl radical (OH). Later, the atom or break molecule has the ability to fluoresce, which signify that it may take in sun light at one wavelength and reradiate it at that same wavelength or, more frequently, a range of longer wavelengths. These wavelength bands, which are predominantly released by broken molecules of carbon, nitrogen, oxygen, and hydrogen, such as CH, NH, NH2, CN, and OH, as well as C2 and C3, consider for almost all of the light from gaseous comets. Which parent molecules disturb apart to form these unstable radicals? Although they haven't been proved, ammonia (NH3) and methane (CH4) are the main candidates. The CN parent molecule is a matter of some discussion. Is cyanogen gas (C2N2) what it may be? alternatively hydrogen cyanide (HCN)?

Examination of the comet at radio wavelengths show that it holds the "exotic" molecules methyl cyanide (CHaCN) and hydrogen cyanide (HCN). Since molecules of fairly form in interstellar clouds, their existence supports the imaginary that comets originate in such an environment.

The majority comets exhibit a massive tail that is just gently bent, mostly the brightest comets. Their fluorescence is indistinguishably to that of the gas in the coma. Still, the molecules that are led to the radiation have been ionized, or stripped of their electrons to leaving them positively charged. Such ion tails cover no un-ionized molecules or radicals, but rather ionized carbon monoxide (CO+), carbon dioxide (CO2), nitrogen (N2), and the radicals OH' and CH'.

While determined molecules can be ionized by sunlight, pressure can also sometimes cause molecules to be forced back into space. (Whipple, 1974)

Abundance of isotope in comets:

Isotopic ratios provide key information on the origin of cometary material. The abundances of the heavier elements in a molecule were determined by the reservoir of heavy isotopes such as HD, atomic D or H_2D^+ present during formation of these ices and the chemical reactions that happened during this time (e.g., Taquet *et al.* 2013). Reactions in the gas phase or in grain-gas interactions lead to various fractionation mechanisms in the ISM. Then when the planets formed in a warmer environment in the protoplanetary disk, further fractionation occurred due to sublimation, photodissociation screening, mixing, and recondensation at various distances and temperatures. The results of these temperature and processing conditions, including isotopologues abundances, may have been frozen in cometary ices. So, isotopic ratios measured in the sublimating gas phase today may reveal their original value 4.6 Gy ago.

The 14N/15N isotopic ratio:

Some comets' $^{14}N/^{15}N$ isotope ratios have been considered using ground-based studies employing NH_2, CN, and HCN (Bockel'ee-Morvan *et al.* 2015). A value was computed from the first measurements (Jewitt *et al.* 1997; Ziurys *et al.* 1999) of comet C/1995 O1 Hale-Bopp utilizing sub-millimeter observation of HCN.

Table 2: Nitrogen isotope ratios in comets

Species	Comet	14N/15N
HCN	C/1995	323±46
CN	C/1995	323±46

The sample of 20 comets of different origins and observed at different distances from the Sun (Manfroid et al.2009) measured an average $^{14}N/^{15}N=147.8\pm5.7$. They also point out that the isotopic ratios are remarkably constant (within the uncertainties) for all comets, irrespective of their origin.

Isotopic ratios of carbon:

Isotopic ratios of carbon, oxygen, and sulfur are available for a suite of comets (cf review by Bockel´ee-Morvan*et al.* 2015). Table:4 provides $^{12}C/^{13}C$ ratios measured in comets and corresponding references. Carbon isotope ratios are often consistent within uncertainties with the terrestrial V-PDB (Vienna Pee Dee Belemnite) reference. The ratios measured in radicals (C_2, CN) and may hence reflect a mixture of different parent species.

Table 3: Carbon isotope ratios in comets

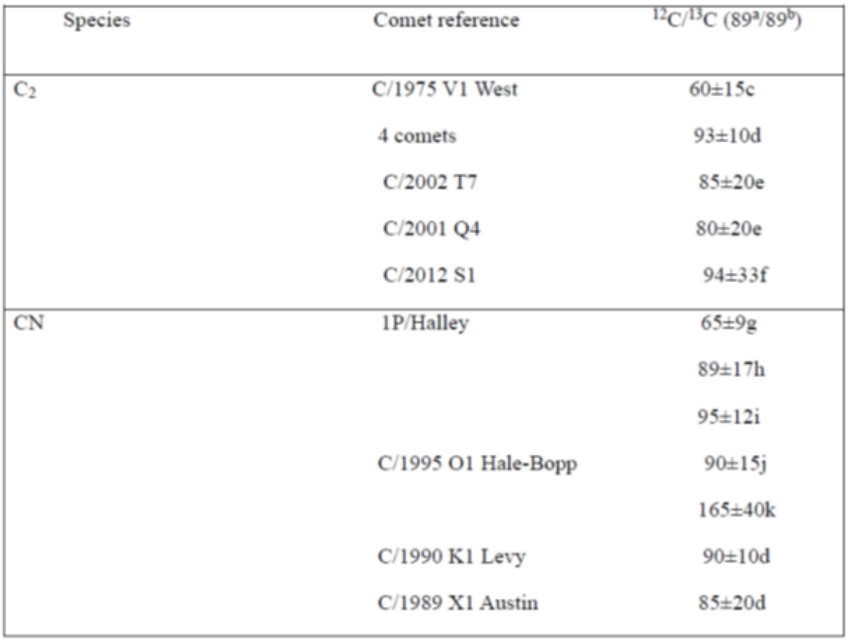

Species	Comet reference	$^{12}C/^{13}C$ ($89^a/89^b$)
C_2	C/1975 V1 West	60±15c
	4 comets	93±10d
	C/2002 T7	85±20e
	C/2001 Q4	80±20e
	C/2012 S1	94±33f
CN	1P/Halley	65±9g
		89±17h
		95±12i
	C/1995 O1 Hale-Bopp	90±15j
		165±40k
	C/1990 K1 Levy	90±10d
	C/1989 X1 Austin	85±20d

Oxygen isotope ratios of comets:

Table 4: Oxygen isotope ratios in comets.

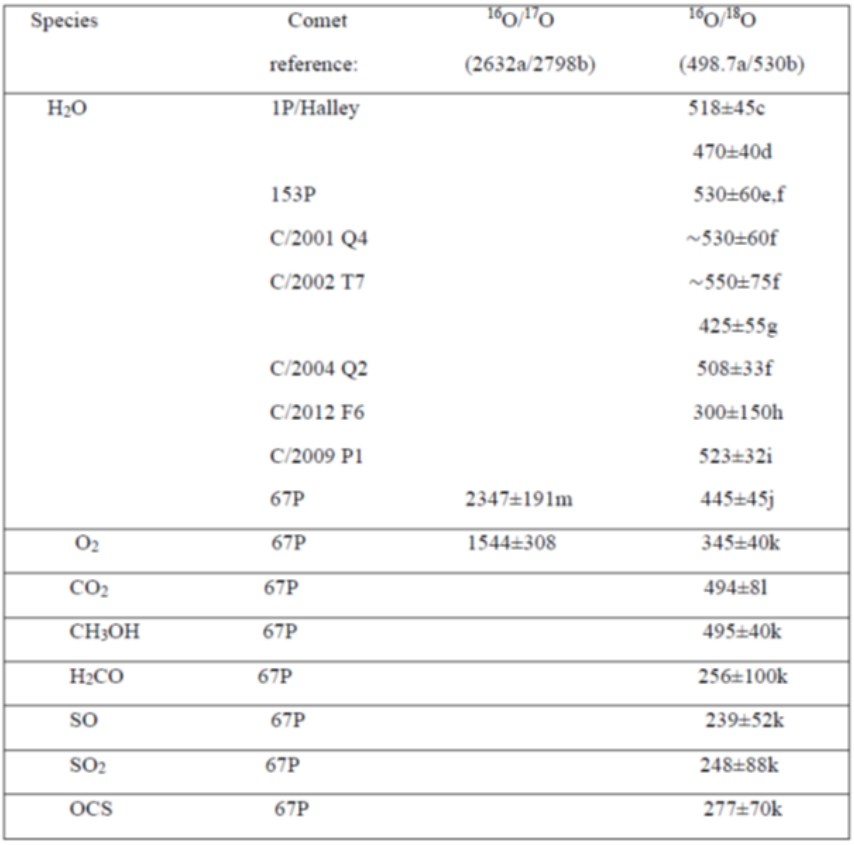

Species	Comet reference:	$^{16}O/^{17}O$ (2632a/2798b)	$^{16}O/^{18}O$ (498.7a/530b)
H_2O	1P/Halley		518±45c
			470±40d
	153P		530±60e,f
	C/2001 Q4		~530±60f
	C/2002 T7		~550±75f
			425±55g
	C/2004 Q2		508±33f
	C/2012 F6		300±150h
	C/2009 P1		523±32i
	67P	2347±191m	445±45j
O_2	67P	1544±308	345±40k
CO_2	67P		494±8l
CH_3OH	67P		495±40k
H_2CO	67P		256±100k
SO	67P		239±52k
SO_2	67P		248±88k
OCS	67P		277±70k

Noble gas isotope ratios in comets:

Table 5: Noble gas isotope ratios in comets 67P and reference material.

Species	Isotopes						Reference
Argon	^{36}Ar/^{38}Ar						
67P	5.4 ±1.4						Balsiger *et al.* (2015)
Solar wind	5.470 ±0.003						Heber *et al.* (2012)
Terr atm	5.319 ±0.008						Lee et al (2006)
Krypton	^{84}Kr/^{80}Kr	^{84}Kr/^{82}Kr	^{84}Kr/^{83}Kr	^{84}Kr/^{86}Kr			
67P	23±14	4.9±0.4	5.3±0.4	3.4±0.2			Rubin *et al.* (2018)
Solar	24.4	4.88	4.93	3.31			Lodders (2010)
Terr atm.	24.9	4.9	24.96	3.30			Aregbe *et al.* (2001)
Xenon	^{132}Xe/^{128}Xe	^{132}Xe/^{129}Xe	^{132}Xe/^{130}Xe	^{132}Xe/^{131}Xe	^{132}Xe/^{134}Xe	^{132}Xe/^{136}Xe	
67P	13±4	0.7±0.1	5.4±0.9	1.2±0.1	4.2±0.9	8.6±3.0	Marty *et al.* (2017)
Solar	11.8	0.96	6.02	1.21	2.73	3.35	Lodders (2010)
Terr atm	14.1	1.02	6.62	1.27	2.58	3.04	Valkiers *et al.* (1998)
Clorine	^{35}Cl/^{37}Cl						
67P	0.336 ± 0.017						Frederik Dhooghe *et al.* (2021)
Bromine	^{79}Br/^{81}Br						
67P	0.95 ± 0.07						Frederik Dhooghe *et al.* (2021)

Conclusion:

The analysis of grains in the coma of comet 81P/Wild 2 has provided insights into comets and their similarity to asteroid materials, particularly in the case of comet Wild 2. Surprising discoveries include crystalline silicates in comet Hale-Bopp, tough inorganic mineral grains in Wild 2's coma, and the absence of amorphous and presolar materials, possibly due to the collection process.

The nature of organic compounds in comets remains uncertain, but the Rosetta mission confirmed the presence of significant organic matter in cometary particles, resembling refractory organics in carbonaceous chondrites. Some organic phases in comets may form due to cosmic ray radiation in the outer protoplanetary disk.

Processes governing the formation and incorporation of mineral and organic components in comets are not fully understood. Cometary dust may carry soluble organics, like amino acids, potentially contributing to prebiotic materials on Earth.

Recent research blurs the distinction between asteroids and comets, with asteroid components found in cometary material and cometary activity observed in asteroids known as "main-belt comets."

Despite progress, critical gaps remain in our understanding of comets, including organics' formation, volatile inorganic condensation, presolar dust's role in early solar system solids, and cometary material's formation and processing. Scientists are also interested in the role of radiogenic nuclides like 26Al.

The idea of a cryogenic sample return from a comet nucleus for analysis in terrestrial laboratories is a promising but unrealized aspiration.

References:

1. Bardyn A, Baklouti D, Cottin H, Fray N. Carbon-rich dust in comet 67P/C-G measured by COSIMA/ROSETTA. Mon Not R Astron Soc. 2017;469:S712–S722.
2. Berdyn A, Baklouti D, Cottin H, Fray N, Briois C, Paquette J. Carbon-rich dust in comet 67P/C-G measured by COSIMA/Rosetta. Mon Not R Astron Soc. 2017;469:712–722.
3. Westphal AJ, Gainsforth Z, Goldstein JI, Humayun M, Kunz M. An ultra Ni-poor metal particle from comet 81P/Wild2. Meteorit Planet Sci. 2012;75:5309.
4. Sarafian AR, Hauri EH. Early accretion of water and volatile elements to the inner Solar System: evidence from angrites. Philos Trans A Math Phys Eng Sci. 2017;375(2094):20160209. doi:10.1098/rsta.2016.0209
5. Altwegg K. 67P/C-G, a Jupiter family comet with a high D/H ratio. Science. 2015;347.
6. Altwegg K. D_2O and HDS in the coma of 67P/C-G. Philos Trans A Math Phys Eng Sci. 2017;375.
7. Bacmann A, Lefloch B, Ceccarelli C, Steinacker J, Castets A, Loinard L. ApJ. 2003;585:L55.
8. Biver N. Isotopic ratios of H, C, N, O and S in comets C/2012 F6 (Lemmon) and C/2014 Q2 (Lovejoy). Astron Astrophys. 2016;589:A78.
9. Bergin EA, Neufeld DA, Melnick GJ. ApJ. 1999;510:L145.
10. Biermann L, Lust RH. Moon, Meteorites and Comets. In: Middlehurst BM, Kuiper GP, editors. Amsterdam: North-Holland; 1963. p. 618.

11. Biver N, Bockelée-Morvan D, Boissier J. Molecular composition of comet 46P/Wirtanen from millimeter-wave spectroscopy. Astron Astrophys. 2021;648:A49.
12. Bockelée-Morvan D, Biver N. The composition of cometary ices. Philos Trans A Math Phys Eng Sci. 2017;375:20160252.
13. Bockelée-Morvan D. Icarus. 1998;133:147.
14. Bohren CF, Huffman DR. Absorption and Scattering of Light by Small Particles. New York: Wiley; 1983.
15. Boss AP. Midplane temperatures and solar nebula evolution. Proc Lunar Planet Sci Conf. 1994;25:149.
16. Bottinelli S. ApJ. 2004;L69.
17. Bouwman J. Astron Astrophys. 2001;375:950.
18. Bowey JE, Adamson AJ. Mon Not R Astron Soc. 2002;334:94.
19. Brownlee D, Tsou P. Stardust: comet and interstellar dust sample return mission. Adv Earth Space Sci. 2003;108(E10).
20. Cazaux S, Tielens AGGM, Ceccarelli C, Castets A, Wakelam V, Caux E, Parise B, Teyssier D. ApJ. 2003;593:L51.
21. Ceccarelli C. In: Mannings V, Boss AP, Russell SS, editors. Protostars and Planets IV. Tucson: Univ. Arizona Press; 2000. p. 47.
22. Ceccarelli C. In: Reipurth B, Jewitt D, Keil K, editors. Protostars and Planets V. Tucson: Univ. Arizona Press; 2007. p. 47.
23. Ceccarelli C, Dominik C. Astron Astrophys. 2005;440:583.
24. Ceccarelli C, Dominik C, Caux E, Lefloch B, Caselli P. ApJ. 2005;631:L81.
25. Cesarsky D, Jones AP, Lequeux J, Verstraete L. Astron Astrophys. 2000;358:708.
26. Charnley SB, Tielens AGGM, Rodgers SD. ApJ. 1997;482:L203.
27. Cochran AL, Cochran WD, Barker ES. N^{+}_{2} and CO^{+} in comets 122P/1995 S1 and C/1995 O1 (Hale-Bopp). Astrophys J. 2000;583–593.
28. Colangeli L, Mennella V, Rotundi A, Palumbo P, Bussoletti E. Simulation of the Cometary 10 micron Band by Means of Laboratory Results on Silicatic Grains. Astron Astrophys. 1995;927–934.
29. Crommelin ACD. Catalogue of Comets. Mem Brit Astron Assoc. 1925;1:26.
30. Dauphas N. The late asteroidal and cometary bombardment of Earth as recorded in water deuterium to protium ratio. Icarus. 2000;148:508–512.
31. Dello Russo N, Kawakita H, Vervack RJ, et al. Emerging trends and a comet taxonomy based on the volatile chemistry measured in thirty comets with high-resolution infrared spectroscopy between 1997 and 2013. Icarus. 2016;273:301–332.

32. Demyk K. In: ISO Beyond the Peaks: The 2nd ISO Workshop on Analytical Spectroscopy. Noordwijk; 2000. p. 183.
33. Dominguez G. A heterogeneous chemical origin of the ^{16}O-enriched and ^{16}O-depleted reservoirs of the early solar system. Astrophys J Lett. 2010;713:L59–L63.
34. Brownlee D, Tsou P, Sléon J. Comet 81P/Wild 2 under a microscope. Science. 2006;314(5806):1711–1716.
35. Dorofeeva VA. Chemical and isotope composition of comet 67P/Churyumov–Gerasimenko: the Rosetta–Philae mission results reviewed in the context of cosmogony and cosmochemistry. Sol Syst Res. 2020;54:96–120. doi:10.1134/S0038094620020021
36. Dorschner J, Begemann B, Henning T, Jäger C, Mutschke H. Astron Astrophys. 1995;300:503.
37. Drozdovskaya MN. Prestellar grain surface origins of deuterated methanol in comet 67P/C–G. Mon Not R Astron Soc. 2021;500:4901–4920.
38. Dobrica E, Engrand C, Duprat J, Gounelle M, Leroux H. Connection between micrometeorites and Wild 2 particles: from Antarctic snow to cometary ices. Meteorit Planet Sci. 2009;44:1643–1661.
39. Whipple FL. The cometary nucleus: current concepts. Astron Astrophys. 1987;187:852–858. Available from: http://adsabs.harvard.edu/abs/1987A%26A...187..852W
40. Whipple F. Astrophys J. 1950;111:375.
41. Matrajt G, Messenger S, Joswiak D, Brownlee DE. Textures and isotopic composition of carbonaceous materials in A and B type Stardust track 130 (Bidi), track 141 (Coki), and track 80 (Tule). Geochim Cosmochim Acta. 2013;117:65–79.
42. Galle JG. Verzeichniss der Elemente der bisher berechneten Cometbahnen. Engelmann Leipzig. 1894.
43. Gautier D, Owen T. The composition of outer planet atmospheres. Space Sci Rev. 1989;21(4).
44. Gensheimer PD, Mauersberger R, Wilson TL. Astron Astrophys. 1996;314:281.
45. Greenberg JM, Li A, Kozasa T, Yamamoto T. In: Gustafson BAS, Hanner MS, editors. Physics, Chemistry, and Dynamics of Interplanetary Dust. ASP Conf Ser. 1996;104:497.
46. Cottin H, Gazeau MC, Raulin F. Cometary organic chemistry: a review from observations, numerical and experimental simulations. Planet Space Sci. 1998;47:1141–1162. doi:10.1016/S0032-0633(99)00024-0
47. Cottin H, Gazeau MC, Raulin F. Cometary organic chemistry: a review from observations, numerical and experimental simulations. Planet Space Sci. 1998;47:1141–1162.

48. Butner HM, Charnley SB, Ceccarelli C, Rodgers SD. Discovery of interstellar heavy water. Astrophys J. 2007;659:L137–L140.
49. Huebner WF. First polymer in space identified in comet Halley. Science. 1987;237:628–630.

    Huebner WF, Boice DC, Korth A. Halley's polymeric organic molecules. Adv Space Res. 1989;9(2):29–34.
50. Hill HGM, Grady CA, Nuth JA III, Hallenbeck SL, Sitko ML. Constraints on nebular dynamics and chemistry based on observations of annealed magnesium silicate grains in comets and in disks surrounding Herbig Ae/Be stars. Proc Natl Acad Sci U S A. 2001;98:2182–2187. doi:10.1073/pnas.051530998
51. Greenberg JM, Li A. Morphological structure and chemical composition of cometary nuclei and dust. Space Sci Rev. 1999;90:149–161.
52. Stodolna J, Jacob D, Leroux H. Mineralogy and petrology of Stardust particles encased in the bulb of track 80: TEM investigation of the Wild 2 fine-grained material. Geochim Cosmochim Acta. 2012;87:35–50.
53. Stodolna J, Gainsforth Z, Butterworth AL, Westphal AJ. Characterization of preserved primitive fine-grained material from the Jupiter family comet 81P/Wild 2: a new link between comet and CP-IDPs. Earth Planet Sci Lett. 2014;388:367–373.
54. Jacq T, Walmsley CM, Henkel C, Baudry A, Mauersberger R, Jewell P. Astron Astrophys. 1990;228:447.
55. Bertaux J, Frohlich F, Ildefonse P. Multicomponent analysis FTIR spectra quantification of amorphous and crystallized mineral phases in synthetic and natural sediments. Sediment Res. 1998;68:440–447.
56. [Merged with 55 as it's the same reference continued.]
57. Jäger C, Dorschner J, Mutschke H, Posch T, Henning T. Astron Astrophys. 2003;408:193–408.
58. Altwegg K, Balsiger H, Fuselier SA. Cometary chemistry and the origin of icy solar system bodies: the view after Rosetta. Annu Rev Astron Astrophys. 2019;57:113–115.
59. Altwegg K, Balsiger H, Bar-Nun A, Berthelier JJ, Bieler A, Bochsler P, Briois C. Prebiotic chemicals–amino acids and phosphorus–in the coma of comet 67P/C-G. Sci Adv. 2016;2.
60. Hornung K, Merouane S, Hilchenbach M, Langevin Y, Mellado EM, Della Corte V, Kissel J, Engrand C, Schulz R, Ryno J, Silen J. A first assignment of the strength of cometary particles collected in situ by the COSIMA instrument onboard ROSETTA. Planet Space Sci. 2016;133:63–75.
61. Kemper F. Nature. 2002;415:295.

62. Lamy PL, Toth I, Jorda L, Weaver HA, A'Hearn M. The nucleus and inner coma of comet 46P/Wirtanen. Astron Astrophys. 1998;335.
63. Leroux H. Fine-grained material of 81P/Wild 2 in interaction with the Stardust aerogel. Meteorit Planet Sci. 2012;47:613–622.
64. Li A, Draine BT. ApJ. 2001;550:L213.
65. Lippi M, Villanueva GL, Mumma MJ. Investigation of the origins of comets as revealed through inferred high-resolution spectroscopy I: Molecular abundances. Astron J. 2021;162:74.
66. Beyer M. Astron Nachr. 1959;284:241.
67. Mahaffy PR, Niemann HB, Alpert A, Atreya SK, Demick J, Donahue TM, Harpold DN, Owen T. Noble gas abundance and isotope ratios in the atmosphere of Jupiter from the Galileo Probe Mass Spectrometer. J Geophys Res. 2000;105(E6):15061–15072.
68. [Duplicate of 67 – merged.]
69. Meeus G. Astron Astrophys. 2001;365:476.
70. Schwamb ME, Knight MM, Jones GH, Snodgrass C, Bucci L, Sánchez Perez JM, Skuppin N. Potential backup targets for Comet Interceptor. Earth Planet Astrophys. 2020 Feb 5:1–5. arXiv:2002.01744.
71. Millar TJ, Bennett A, Herbst E. ApJ. 1989;340:906.
72. [Duplicate of 71 – merged.]
73. Molster FJ, Waters LBM, Tielens AGGM, Barlow MJ. Astron Astrophys. 2002;382:184.
74. Muller D. High D/H ratios in water and alkanes in comet 67P/C-G measured with Rosetta/ROSINA DFMS. Astron Astrophys. 2022;662:A69.
75. Biver N, Dello Russo N. Chemistry of comet atmospheres. [No date].
76. Biver N, Dello Russo N, Opitom C, Rubin M. Chemistry of comet atmospheres. [Preprint]. 2022 Jul 11.
77. Biver N, Dello Russo N, Opitom C, Rubin M. Chemistry of comet atmospheres. Earth Planet Astrophys. 2022 Jul 11:12–31. doi:10.48550/arXiv.2207.04800
78. Nuth JA III, Charnley SB, Johnson NM. In: Lauretta DS, McSween HY, editors. Meteorites and the Early Solar System II. Tucson: Univ. Arizona Press; 2006. p. 147.
79. Onaka T, Okada Y. ApJ. 2003;585:872.
80. Eberhardt P, Reber M, Krankowsky D, Hodges RR. The D/H and $^{18}O/^{16}O$ ratio in water from comet P/Halley. Astron Astrophys. 1995;302:301.
81. Pardo JR. ApJ. 2001;562:799.
82. Parise B. Astron Astrophys. 2006;453:949.

83. Parise B. Astron Astrophys. 2002;393:L49.
84. Parise B. Astron Astrophys. 2005;431:547.
85. Hartogh P, Lis DC, Bockelée-Morvan D, de Val Borro M, Biver N, Küppers M, et al. Ocean-like water in the Jupiter-family comet 103P/Hartley 2. Nature. 2011;478:218–220.
86. Pickett HM. J Quant Spectrosc Radiat Transfer. 1998;60:883.
87. Hagemann R, Nief G, Roth E. Absolute isotopic scale for deuterium analysis of natural waters: Absolute D/H ratio for SMOW. Nature. 1970;712–715.
88. Richter NB. The Nature of Comets. 1963;VII:181.
89. Robert H, Herbst E, Millar TJ. ApJ. 2023;L41.
90. Rodgers SD, Charnley SB. ApJ. 2001;553:613.
91. Rodgers SD, Millar TJ. Mon Not R Astron Soc. 1996;280:1046.
92. Rubin M, Altwegg K, Balsiger H, et al. Elemental and molecular abundances in comet 67P/C-G. Mon Not R Astron Soc. 2019;594–607.
93. Stark R. ApJ. 2004;608:341.
94. Stern SA, Parker JW, Festou MC, A'Hearn MF, Feldman PD, Schwehm G, et al. HST mid-ultraviolet spectroscopy of comet 46P/Wirtanen during its approach to perihelion in 1996–1997. Astron Astrophys. 1998;335:L30–L36.
95. Swings P, Haser L. Atlas of Representative Cometary Spectra. 1961.
96. Stephan T, Flynn GJ, Sandford SA, Zolensky ME. TOF-SIMS analysis of cometary particles extracted from Stardust aerogel. Meteorit Planet Sci. 2008;43:285–295.
97. Farnham TL, Schleicher DG. Physical and compositional studies of Comet 81P/Wild 2 at multiple apparitions. Icarus. 2005;178:2–49.
98. Vriend W. M.S. Thesis. Groningen University; 1999.
99. Waelkens C. Astron Astrophys. 1996;315:L245.
100. Waters LBFM, Molster FJ, de Jong T. Astron Astrophys. 1999;315:L36.
101. Watson WD. Rev Mod Phys. 1976;48:513.
102. [Duplicate of 101 – omitted.]
103. Whipple FL. The nature of comets. Sci Am. 1974;230:48–57. Available from: https://www.jstor.org/stable/10.2307/24950006
104. Wooden DH. Earth Moon Planets. 2002;89:247.

Advances in Material Science Volume I

ISBN: 978-93-91768-58-4

About Editors

Dr. Vijayalakshmi A. R., M.Sc., Ph.D., is presently working as Associate Professor in Mathematics, Maharani's Science College for Women, Palace Road, Bangalore. She has taught 21 years for B. Sc and 15 years for M.Sc. She has published 18 papers in peer reviewed journals and 5 in Conference proceedings and has been resource person for many workshops. She has presented papers in several national and international conferences Her area of research interest are Nano technology, Stability of flows, heat transfer in fluid flow, stretching sheet problems.

Dr. Nimish Vasoya is working as an Associate Professor and Head, Department of Balbhavan and Toy Innovation, Children's University, Gandhinagar, Gujarat. Dr. Nimish Vasoya awarded with Ph. D. in the subject of Physics in 2013 from Saurashtra University. He is now an Associate Professor of Physics in Gandhinagar, Gujarat, as well as the Director of the School of Indic Studies and a Member of the University's Executive Council. He also received various International awards like Chandubhai Patel (Vakil) foundation for the Shri Natvarbhai Motibhai Patel Research award in the year 2006-2007 from Sardar Patel University, Vallabh Vidyanagar, Gujarat. I2OR Outstanding researcher 2018 at 3rd international convention on ISRD, CII Chandigarh Greek ThinkerZ Academic Leadership award 2019 in the field of Physics by Green ThinkerZ Society, India.

Dr. Shakuntala Avdhutrao Shinde has completed his post-graduation and Ph.D. degree in Physics by Swami Ramanand Teerth Marathwada University, Nanded. Presently she is working as an Assistant Professor and Head, Department of Physics, Sharadchandra Arts, Commerce and Science College Naigaon, Dist- Nanded. She has over twelve years of teaching experience at UG level. She is actively engaged in various academic and research activities. He has published over 20 research papers in various peer reviewed journals. She has published articles and chapters in Books, conference proceedings etc. She has presented papers in national and international Conferences.

Dr. Radhika G. Deshmukh is presently working at Shri Shivaji Science College, Amravati, Maharashtra, India, as an Assistant Professor. She is M. Sc. (Physics), B. Ed, Ph. D. Relativity, Nanotechnology, Renewable energy, Luminescence and Physics and school Science education are her research interest areas. Dr. Radhika is a member of IAPT, ISCA, Marathi Vigyan Parishad. She has felicitated by- Savitribai Phule Best Teacher award of 2019 by Maharashtra Government; Best women Research award by Nova Research Academy, Pondicherry; and by IRDP Award, Madras. She has got two international patents. She has published 15 papers in Scopus, SCI and UGC care listed journals. She has presented papers in number of National and International Conferences. She has been working for socio-economically backward students and women's. Her motto is to spread science and technology among rural and tribal students

Bhumi Publishing

ISBN 978-93-91768-58-4

9 789391 768584